Generation Mechanisms of Ion Upflow in the Polar Topside Ionosphere

（極域上部電離圏におけるイオンアップフローの生成機構の研究）

Yasunobu Ogawa

小川 泰信

Division of Particle and Astrophysical Science
Graduate School of Science
Nagoya University, Japan

名古屋大学大学院理学研究科素粒子宇宙物理学専攻

February 2002

A Dissertation for the Degree of Doctor Scientiarum

Generation Mechanisms of Ion Upflow in the Polar Topside Ionosphere

（極域上部電離圏におけるイオンアップフローの生成機構の研究）

Yasunobu Ogawa

小川 泰信

Division of Particle and Astrophysical Science
Graduate School of Science
Nagoya University, Japan

名古屋大学大学院理学研究科素粒子宇宙物理学専攻

February 2002

Acknowledgments

I would like to express my deepest gratitude to my supervisor Prof. Ryoichi Fujii for his continuous encouragement of my work on this thesis. This thesis could not have been completed without his appropriate guidance. I would also like to express my sincere gratitude to the other members of the advisory committee, Prof. Tadahiko Ogawa, Prof. Masayoshi Kojima, and Dr. Kazuo Shiokawa, for their constructive comments on this thesis. I would also like to express my respectful gratitude to Dr. Satonori Nozawa who took time to help with data collection. He also read this thesis and gave me a number of helpful suggestions.

I would like to sincerely acknowledge Dr. Stephan C. Buchert at the Swedish Institute of Space Physics (IRF) in Sweden for the helpful discussions and encouragement on the entirety of this thesis. I also deeply appreciate the discussions and suggestions of Dr. Francois Forme at Centre d'etude des Environnements Terrestre et Planetaires (CETP) in France, which greatly helped me with research of Chapter 5 in this thesis.

I am deeply grateful to Dr. Shin-ichi Ohtani at the Applied Physics Laboratory, Johns Hopkins University (APL/JHU) in the USA, for giving me a wonderful chance for collaboration using the data of the DMSP satellites. He kindly helped me during my visit to APL/JHU in May 2001, and gave me useful advice and comments on my study.

I would like to express my sincere appreciation to Prof. Shigeto Watanabe at Hokkaido University, Prof. Sawako Maeda at Kyoto Women's University, and Prof. Toshifumi Mukai and Dr. Takumi Abe at the Institute of Space and Astronautical Science (ISAS), for their kind encouragement and useful advice on my study. I would also like to acknowledge the contribution of Mr. Toshiaki Yamaguchi, Ms. Youko Yamaguchi, Ms. Judy Kishida, Dr. Shin-ichiro Oyama, Dr. Susumu Saito, Mr. Minoru Endo, Ms. Katsue Suzuki, Mr. Masahiko Sugino, Mr. Hirotada Kataoka, Mr. Kazuhiro Morise, Mr. Syun-ichi Matsuo, Mr. Kazuhiro Adachi, Ms. Seiko Imaida, Mr. Masaki Kono, Mr. Hiroyuki Iwahashi, Ms. Satoko Sumiyama, and Mr. Takafumi Tamagawa, who are the staff, graduate students, and graduates of the Solar-

Terrestrial Environment Laboratory (STEL) of Nagoya University, for their support and friendship. I am also thankful to Mr. Naofumi Yoshida at Tohoku University, and Mr. Manabu Yamada at Hokkaido University, for their studying and discussing with me the topics associated with this thesis.

I am indebted to the director and staff of the EISCAT for operating the facility and supplying data. EISCAT is an international association supported by Finland (SA), France (CNRS), the Federal Republic of Germany (MPG), Japan (NIPR), Norway (NFR), Sweden (NFR), and the United Kingdom (PPARC). The DMSP particle detectors were designed by Dr. Dave Hardy of AFRL, and the data was obtained from JHU/APL. I also thank Dr. Dave Hardy, Dr. Fred Rich, and Dr. Patrick Newell for the use of the detectors. I am also grateful to the staff of the CDA web for providing public WIND and ACE satellite data.

Finally, I would like to express my deepest thanks to my family for their continuous encouragement and especially to my parents for their permission for me to proceed with my studies in the graduate school.

General Notation

$\boldsymbol{E}$	electric field vector [V m^{-1}]
$\boldsymbol{B}$	geomagnetic field vector [T]
$\boldsymbol{V}$	velocity vector [m s^{-1}]
$\boldsymbol{g}$	gravitational acceleration vector [m s^{-2}]
$\boldsymbol{j}$	current density vector [A m^{-2}]
e	electric charge [C]
t	time [sec]
m	mass [kg]
n	number density [m^{-3}]
T	temperature [K]
P	pressure [Pa]
I	geomagnetic dip angle [$^\circ$]
k	wave number [m^{-1}]
ν	collision frequency [s^{-1}]
k_B	Boltzmann constant (= 1.38×10^{-23} J K^{-1})

Subscript

e	electrons
i	ions
n	neutrals
in	ion-neutral
ie	ion- electron
en	electron-neutral
ei	electron-ion
//	parallel to the geomagnetic field line
$\perp$	perpendicular to the geomagnetic field line

Abstract

We have investigated three aspects of ion upflow phenomena in order to understand the generation mechanisms of ion upflow. The first step was to investigate the relationship between ion upflow and particle precipitation which is different between several magnetospheric regions. The second step was to investigate the relationship between ion upflow and heating, from the macroscopic point of view. The third step was to investigate the characteristics of naturally enhanced ion-acoustic lines (NEIALs), which may be caused by plasma instabilities and are strongly related to ion upflow from the microscopic point of view.

We have examined the regions where dayside field-aligned (FA) ion upflows occur, based on a statistical analysis using approximately 170 simultaneous events between the EISCAT Svalbard radar (ESR) and the DMSP satellites. This systematic analysis for ion upflow has never been examined. We found that ion upflows occur not only in the cusp and cleft (the low-altitude portion of the low-latitude boundary layer (LLBL)) which have been considered as ion upflow regions, but also in the topside ionosphere connected to the mantle region. Ion upflows seldom occur either in the Boundary Plasma Sheet (BPS) or in the Central Plasma Sheet (CPS) in the dayside high latitudes. Almost all of the events in which the average FA ion velocity is more than 100 m s^{-1} are associated with sufficient soft electron precipitation (differential energy flux of electrons at 100 eV > 10^7 eV cm^{-2} s^{-1} sr^{-1} eV^{-1}). Although soft electron precipitation also sufficiently exists in the BPS, the ion velocities are mostly less than 100 m s^{-1}. The present results indicate that soft particle precipitation is the predominant energy source driving ion upflow in the topside ionosphere, but it works on ion upflow effectively in the higher latitude regions in the dayside and not in the BPS.

Plasma heating associated with FA ion upflow in the dayside topside ionosphere has been presented using data obtained simultaneously with the ESR and the EISCAT VHF radar. The FA ion upflows observed at an altitude of 665 km in the dayside cusp are associated with significant anisotropy of ion temperature, isotropic increases of electron temperature and

enhancements of electron density. The anisotropy factor reaches maximum values of 1.7. There is no clear correspondence between the enhancements of the electric field strength and the occurrence of the ion upflows. This is the first experiment to point out ion anisotropy independent of frictional heating. The ion upflow associated with perpendicular heating seems to closely correspond to NEIALs, because the FA ion velocity immediately changed around strong NEIALs.

The wave number (k)-dependence of the received power in high signal-to-noise ratio (SNR) conditions, occurring for NEIALs and for real satellites, has been investigated. These analyses help to specify generation mechanisms of NEIALs. In the case of NEIALs, we found that variations of the relative power between channels well above both the estimated and expected 1-sigma level occur over a signal pre-integrated profile, and a few profiles where the power radiated by NEIALs varies systematically with wavelength/wave number (k). This feature of NEIALs does not seem to be caused by the ESR system. Furthermore, power differences along one profile with NEIALs are obviously different from those of echoes from satellites at a similarly high SNR. The most plausible explanation we can suggest is that the k-dependence of the power in NEIAL events has its origin in the scattering medium itself. The frequency dependence of the power in NEIAL events and the characteristics of the enhanced peak heights can be well explained by the parametric decay of Langmuir waves [*Forme et al.*, 2001].

The results from these three investigations lead to the conclusion that the energy of soft electron precipitation is considered as the main source of the ion upflow. The energy of soft particle precipitation is supplied to the ions in the topside ionosphere via wave-particle interaction, such as wave-induced transverse ion heating, and upward parallel electric field due to anomalous resistively produced by plasma turbulence. Thus generation mechanisms of ion upflow must have the transversely ion heating and the upward acceleration by wave-particle interaction while the induced plasma waves decay. In addition to direct precipitation effects, namely enhanced ambipolar diffusion and heat flux, wave-particle interaction may hence play an important role in driving ion upflow.

Contents

Chapter 1

General Introduction

The Earth's magnetosphere is formed by magnetic fields originating from within the Earth, the solar wind and the interplanetary magnetic field (IMF) originating from within the Sun, and plasma particles existing there. The plasma particles in the magnetosphere are not generated there, but are transported from other places. With regard to the locations supplying plasma particles, it was considered in the past that the solar wind, composed by hydrogen ions (H^+), helium ions (He^+), and electrons, was the source of the magnetospheric plasma because particles originating from within the Earth were gravitationally bound on the Earth's surface. However, observations over the last three decades clearly indicate that ionospheric ions, such as molecular nitrogen ion (N_2^+), molecular oxygen ion (O_2^+), and oxygen ion (O^+) are indeed in the magnetosphere [*Yau and André*, 1997 and references therein]. Thus, it is now clear that the ionosphere is an important source of ions for the magnetospheric plasma [*Chappel*, 1988; *Shelly*, 1988]. In other words, the outflows of ionospheric ions to the magnetosphere are also important for the formation of the magnetosphere. Additional evidence exists demonstrating that the geomagnetic activity seems to control the supply of magnetospheric ions from the ionosphere. A higher geomagnetic activity enhances a greater abundance of ionospheric plasmas in the magnetosphere. On the other hand, plasmas in the plasma sheet seem to be at least partly controlled by solar wind during geomagnetically quiet situations [e.g., *Winglee*, 1998]. This change of the magnetospheric ion composition is important, because increased heavy ion such as O^+ can have large effects on some important magnetospheric processes [e.g., *Fu et al*., 2001].

The ionosphere and the magnetosphere are closely linked together through the magnetic

field lines. Ions, in particular, in the polar ionosphere obtain energy and momentum from the magnetosphere through particle precipitation, heat flux, propagation of electric fields and plasma waves. Consequently ions in the ionosphere occasionally can move up to higher altitudes and subsequently flow into the magnetosphere and interplanetary region. Recently characteristics of the magnetospheric ions originating in the ionosphere have become clear as a result of several studies using satellites [*Yau and André*, 1997 and references therein]. However, little is known about ion heating and acceleration mechanisms around the polar topside ionosphere, where ions do start to flow up to the magnetosphere. In this thesis, we have investigated the generation mechanisms of this ion upward flow occurring at the polar topside ionosphere.

For a general introduction, characteristics of particles in the polar ionosphere and the magnetosphere are briefly reviewed in this chapter. We particularly describe distributions of particles in the polar ionosphere in Section 1.1, in several of the magnetospheric regions in Section 1.2, and in several ion outflow phenomena observed mainly in the bottomside magnetosphere in Section 1.3. Characteristics of ion upflow in the topside ionosphere and naturally enhanced ion-acoustic lines (NEIALs), which we mainly focus on this thesis, are described in Section 1.4 and Section 1.5. Finally, the purpose of this thesis is described in Section 1.6.

1.1 Ionosphere in the High Latitudes

The Earth is covered with the atmosphere, in which particles are gravitationally bound to low altitudes and maintain their distribution under a diffusive equilibrium. Figure 1.1a shows typical height profiles of the number density of different neutral species below 1000 km altitude at the high latitude, calculated using the Mass Spectrometer and Incoherent Scatter (MSIS) neutral atmosphere model [*Hedin*, 1991]. Below approximately 150 km altitude, the major neutral species are molecules of nitrogen (N_2) and oxygen (O_2), which are the same as those found on the ground. Above approximately 300 km altitude, the number density of atomic oxygen (O) exceeds those of N_2 and O_2. The atomic oxygen is produced by photodissociation and energetic particle impact dissociation. A minor species, atomic nitrogen (N) and nitrogen monoxide (NO), is produced by molecular dissociation and various chemical reactions. Above approximately 900 km altitude, the number densities of atomic helium (He) and hydrogen (H) exceed that of O. The transition height strongly depends on the solar

activity and season. While O dominates the upper atmosphere even above 1000 km during solar maximum conditions, He and H dominate above 500 km during solar minimum and winter conditions.

Around a few hundred km in altitude, various gases in the atmosphere are partly ionized mainly by solar EUV. The region of these mixed ions, electrons, and neutral particles is called the ionosphere. Solar irradiation of intensity decreases due to absorption downward in the Earth's atmosphere where the neutral density increases toward the Earth. The ionization at higher altitudes (above approximately 400 km altitude) balances the diffusion of ions under a diffusive equilibrium, whereas the ionization at lower altitudes (below approximately 200 km altitude) balances the recombination between ion and electrons under a photochemical equilibrium. The ionosphere therefore has a peak at a certain altitude. Figure 1.1b shows typical height profiles of the number density of electrons and different ion species below 1000 km altitude, calculated using the International Reference Ionosphere (IRI) model [*Bilitza*, 1997]. A clear peak is seen at approximately 300 km altitude, as we have mentioned before. The region around the peak is called the *F* region, and the peak is called the *F* peak. Furthermore, a region above the *F* peak is called the topside ionosphere, and a region below the *F* peak, around an altitude of 100 km, is called the *E* region. The number densities of electrons and total ions around the *F* peak are approximately 3×10^{11} m^{-3}, which is roughly 1000 times smaller than that of neutral particles. Hence the ionosphere consists of weakly ionized plasma.

Regarding the composition of ionospheric ions, major neutral particles at each altitude, i.e. N_2, O_2, and O, are ionized by the solar EUV and changed into a molecular nitrogen ion (N_2^+), molecular oxygen ion (O_2^+), and oxygen ion (O^+). These ions are changed into other ions or neutrals through chemical reactions. First, N_2^+ recombines with an electron and dissociates into two nitrogen atoms (N), or recombines with the abundant O_2 and O and forms O_2^+ and nitrogen monoxide ion (NO^+). Secondly, O_2^+ remains there, or recombines with an electron and dissociates into two oxygen atoms (O). Finally, O^+ also remains there, or recombines with the abundant N_2 and O_2 and forms NO^+ and O_2^+. Consequently NO^+ and O_2^+ are dominant below approximately 200 km, while O^+ is dominant above 200 km. The composition ratios as well as the absolute values change by solar zenith angles, particle precipitations, and the ionospheric electric field [e.g., *Schunk*, 1975]. Above approximately 900 km altitude, the number density of the hydrogen ion (H^+) exceeds that of O^+. Although the transition height from O^+ to H^+ as well as that from O to H strongly depends on the solar activity and season,

dominate regions of the heavy ions such as N_2^+, O_2^+, and O^+ are always maintained below the region where H^+ is dominant.

The temperature of the ionosphere is essentially controlled by the absorption of solar UV radiation in the thermosphere. A typical model of temperature profiles for the neutrals, ions, and electrons is shown in Figure 1.2. The electrons have a larger mobility and heat conductivity so that the temperature of the electrons usually becomes higher than the temperature of the ions. The ions are heavier and interact by collision more strongly with neutrals than with electrons around the *F* peak. Because of the similar masses between the colliding species, much of the excess energy of the ions is transferred to the neutrals. The temperature of the ions is therefore smaller than that of the electrons, but higher than the temperature of the neutrals around the *F* peak. Ion temperature increases with increasing altitude and comes close to the electron temperature at the topside of the *F* peak because collisions between ions and electrons become dominant at higher altitudes. These temperature profiles are also significantly dependent on solar activity [e.g., *Roble and Emery,* 1983]. At the high latitude, these temperatures are also strongly affected by electric fields and precipitations from the magnetosphere.

1.2 Particles in Each Magnetospheric Region

As already mentioned, the ionosphere and magnetosphere are closely linked together through the magnetic field lines. Magnetospheric electric fields map down to the ionosphere, creating, for example, the plasma convection, frictional heating and plasma instabilities. At high latitudes, particle precipitation from the magnetosphere ionizes the atmosphere. The heat flux from the magnetosphere is also conducted down to the ionosphere. The characteristics of particle precipitation from the magnetosphere are quite different from one regime to another in the magnetosphere, such as the plasma sheet, low-latitude boundary layer (LLBL), lobe, mantle, and cusp (see Figure 1.3). In particular, the dayside auroral precipitation consists of magnetosheath origin related boundary layer precipitation, and plasma sheet origin related Boundary Plasma Sheet (BPS) and Central Plasma Sheet (CPS) precipitation considered as extensions of the nightside precipitation regions. We first describe the characteristics of these regions.

1.2.1 Cusp

The magnetic field lines of the Earth can be divided into two parts according to their location on the sunward or tailward side of the Earth (see Figure 1.3). Between these two parts on both hemispheres are funnel-shaped areas with a near zero magnetic field magnitude called the polar cusp. It allows the magnetosheath plasma to directly enter the ionosphere, which generally occurs where the ion cutoff drops to at least 1 - 3 keV and below. The cusp position and the precipitation fluxes strongly depend on the IMF and solar wind conditions [*Newell et al*., 1989; *Zhou et al*., 2000].

1.2.2 Low-Latitude Boundary Layer

Low-latitude boundary layer (LLBL), first discussed by *Eastman et al*. [1976], is the dayside magnetospheric boundary layer at a low-latitude and continues to the magnetotail. It consists of a mixture of plasmas of magnetospheric and magnetosheath origins; the magnetosheath plasma may leak diffusively through the magnetopause into this region. The density and temperature are approximately 5×10^{5} - 10^{7} m^{-3} and from less than 100 eV to 1000 - 2000 eV, respectively. The LLBL is distinguished from the cusp by higher average particle energies and smaller precipitating ion energy fluxes. The low-altitude portion of the LLBL is called the cleft.

1.2.3 Mantle

Mantle, first defined by *Rosenbauer et al*. [1975], covers much of the high-latitude magnetosphere, extending tailward from the cusp region (see Figure 1.3). Mantle is characterized by de-energized magnetosheath plasma. The density and temperature are a few times 10^{4} - 10^{6} m^{-3} and approximately 100 eV, respectively. The particles flow tailward at a velocity of 100 - 200 km s^{-1}. The density and energy often decrease when moving inward from the magnetosheath towards the magnetosphere (velocity filter effect); at a low-altitude this creates an energy-latitude dispersion. Ions originating in the ionosphere have also been found in the mantle/lobe regions [*Mukai et al*., 1994; *Hirahara et al*., 1996; *Seki et al*., 1998].

1.2.4 Plasma Sheet and Plasma Sheet Boundary Layer

Plasma sheet is located in the center of the tail near the equatorial plane (see Figure 1.3). The Plasma sheet particles are hot, having energies in the keV range. The plasma density is a slowly varying function of time, the average value being approximately $4\times10^5 - 2\times10^6$ m^{-3}. The ion temperature is approximately 7 times higher than the electron temperature [*Baumjohann et al*., 1989]. Plasma Sheet Boundary Layer (PSBL) is generally observed as a transition region between the lobes and the plasma sheet (see Figure 1.3). The number density is typically 10^5 m^{-3}, which is slightly smaller than that in the plasma sheet.

From ionospheric observations related to the plasma sheet and PSBL, two different types of precipitations have been found. They were defined by *Winningham et al.* [1975] as Central Plasma Sheet (CPS) and Boundary Plasma Sheet (BPS), respectively, because traditionally the CPS is assumed to map to the plasma sheet in the magnetosphere and the BPS to the PSBL. However, these interpretations have been modified by several observations in the magnetosphere [e.g., *Feldstein and Galperin*, 1985; *Sandahl and Lindquist*, 1990; *Fukunishi et al*., 1993]. Through those observations, there is general agreement that the plasma sheet in the tail covers the whole of the auroral oval in the nightside and the inverted-V region associated with the (low-altitude) BPS must be mapped to the outer portion of the plasma sheet, not to the PSBL. Thus, the CPS and BPS terms defined by low-altitude observations have been used simply as the phenomenologically defined regions of the diffuse and discrete aurora on the nightside of the Earth.

Dayside precipitation in the BPS closely resembles the poleward portion of the nightside auroral oval. The electrons have a typical temperature of approximately 300 eV, which is somewhat higher than the LLBL. It remains an unsettled question whether BPS as well as LLBL belongs to the closed field-line region or to the open one [*Lockwood*, 1997]. The CPS is the hard zone of the electron precipitation whose typical energies are above 1 keV. The CPS in the dayside consists of electrons that have been injected into the near-Earth region from the nightside and subsequently drift around the Earth.

Figure 1.4 shows the results of the mapping of several magnetospheric regions mentioned above to the dayside ionosphere, according to particle precipitation characteristics. Ionospheric ions have been found in almost all magnetospheric regions mentioned above. In the next section, we describe several kinds of ion outflow processes from the ionosphere to

the magnetosphere.

1.3 Ion Outflow Processes From the Ionosphere to the Magnetosphere

An important phenomenon of the ionosphere-magnetosphere coupling is the formation of upward ion flows from the ionosphere since they can be a significant source of magnetospheric plasma. Based on several observations around the bottomside magnetosphere, ion outflow phenomena can be grouped into two categories. One is the bulk ions in the ionosphere escaping to the magnetosphere. The other one is a fraction of the bulk ions accelerated and escaping to the magnetosphere. We review the characteristics of ion outflow in order.

In the polar cap, bulk ions continuously escape without any special heating. The phenomenon is called “polar wind.” *Abe et al.* [1993] shows the height distributions of the polar wind in which ions start to flow up around 3000 km and the escape velocities become faster with increasing altitude (see Figure 1.5). Ion species of the polar wind are considered to be H^+, He^+, and O^+, which are relatively lighter ions in comparison to NO^+ and O_2^+.

The ion outflow associated with partially accelerated ions can be divided into several types, such as ion beams, transversely accelerated ions (TAIs), ion conics, and upwelling ions (UWIs). The characteristics are usually seen in the high-energy part of the ion velocity distributions. Ion beams have a peak flux along the upward magnetic field direction and are generally observed above 5000 km altitude. The field-aligned ion energization of several eV results from parallel electric fields.

TAIs and ion conics were first observed by *Sharp et al*. [1977]. Ion conics have a peak flux at an angle to the upward magnetic field direction, while TAIs have peak pitch angles at or close to 90˚. Ion conics are sometimes interpreted as TAIs from a lower altitude which spiral up the field line as a result of the magnetic mirror force. On the dayside, TAIs are regularly present down to approximately 3000 km on the Akebono satellite [*Whalen et al*., 1991]. On the nightside, TAIs are observed at 1400 km on the ISIS-2 satellite [*Klumpar*, 1979] and at 1700 km on the Freja satellite [*André et al*., 1994], and frequently down to 400 km on sounding rockets during an active aurora [*Yau et al*., 1983; *Arnoldy et al*., 1992]. Ion conics also have been observed at altitudes down to approximately 1000 km on sounding rockets and on the ISIS-2 satellite [*Klumpar*, 1979; *Yau et al*., 1983], and up to several Earth’s

radii on the PROGNOZ-7 satellite [*Hultqvist et al*., 1983].

TAIs and ion conics are related to transverse ion heating events with typical energies from thermal to a few keV accompanied with upward flowing ions, electron precipitation and density depletions, and a variety of different resonant waves, such as lower hybrid (LH) waves or low-frequency broadband electrostatic waves [e.g., *Moore et al.*, 1996; *André,* 1997]. Recent satellite and rocket observations indicate that broadband low-frequency emissions are the most important wave signatures associated with perpendicular ion energization, probably followed by waves around a LH wave frequency. In a statistical study using data from the Freja satellite obtained near 1700 km [*André et al*., 1998], perpendicular O^+ ion heating to mean energies above 5 - 10 eV were classified into the four types shown in Figure 1.6. Type 1 and 2 are both associated with broadband low-frequency waves (a few Hz). Type 3 is connected with auroral electrons and waves near half of the hydrogen gyro frequency (about 200 Hz) or waves around the LH wave frequency (about 1 kHz), while type 4 is associated with precipitating H^+ or O^+ and waves around the LH wave frequency. Type 2 is also associated with precipitating protons with keV energies and electrons with mean energies of approximately 100 eV. It is clear that broadband low-frequency waves are the most common wave signatures in Figure 1.6. The large-amplitude electric field fluctuations can produce a perpendicular acceleration of ionospheric ions [e.g., *Lundin and Hultqvist*, 1989; *Hultqvist*, 1996].

Although observed ion conics and TAIs typically have energies from 10 eV to a few keV, lower-energy TAIs also exist and have been reported from sounding rocket flights [*Garbe et al*., 1992; *Yau et al.*, 1983]. However, observationally they are often difficult to investigate in detail from satellite measurements due to limited detector energy resolution, spacecraft velocity, and spacecraft charging.

1.4 Ion Upflow in the Polar Ionosphere

Around the auroral oval, bulk ions in the *F* region/topside ionosphere move upward along the field lines with transient plasma heating. The phenomenon is called “ion upflow.” Ion upflow is often observed with Incoherent Scatter (IS) radars located in the high latitudes [e.g., *Keating et al*., 1990; *Foster et al*., 1998; *Endo et al*., 2000]. The typical velocity of ion upflow is a few 100 m s^{-1} to a few 1000 m s^{-1}, which is smaller than the escape velocity from the Earth. Hence it is still not understood how the ion upflow at high latitudes relates to the

magnetospheric ion outflow for which the ions have presumably overcome the Earth's gravity and succeeded to escape. However, ion upflow must certainly play an important role as plasma sources of the ion outflow, because heavy ions such as NO^+ and O_2^+ found in the ion outflow and in the magnetosphere should primarily exist only in the lower ionosphere so a certain process must occur such as ion upflow to bring these heavy ions to the bottomside magnetosphere.

IS radar observations by *Wahlund et al*. [1992a] have shown ion upflow events associated with strong perpendicular electric fields, frictional ion heating, an elevated *F* region and low electron densities below 300 km indicating a small amount of auroral precipitation. This could be explained by strong pressure gradients produced by an increased ion temperature, and the consequent pushing of ions upward. It is possible that these upflow events are bulk plasma upflows with both ions and electrons moving upward. Observations with IS radars have shown that rather strong DC electric fields heat ions anisotropically by ion-neutral collisions [*Winser et al*., 1989]. Modelers have demonstrated that this anisotropic ion frictional heating can cause ion upflow [*Köeröesmezey et al*., 1992]. Around the dayside polar ionosphere, *Ogawa et al*. [2001] have shown ion upflow associated with frictional heating using data obtained from the EISCAT Svalbard radar (ESR) and the CUTLASS HF radars.

Wahlund et al. [1992a] also reported ion upflow associated with auroral precipitation, which showed an enhanced electron temperature and field-aligned currents with the bulk ion population moving upward and the bulk electron population moving downward. They argued that this ion upflow may be due to enhanced field-aligned electric fields caused by anomalous resistively due to low-frequency plasma turbulence (e.g., ion-acoustic turbulence). While this type of ion upflow occurs, anomalously enhanced IS signals often received toward the field-aligned direction. We describe the plausible physical mechanisms of the enhanced IS signals in the next section in this chapter.

Although both ion upflow and TAIs seem to occur in the vicinity of the auroral zone and are related to the soft electron precipitations, no ion anisotropy has been reported in this type of ion upflow. It is hence a clear question as to how the ion upflows induced by particle precipitation are related to heating associated with TAIs, which are often observed at somewhat higher altitudes as well as at higher transverse energies. Generally, IS radar observations of ion upflow phenomena are difficult to correlate with satellite measurements.

1.5 Naturally Enhanced Ion-Acoustic Lines

IS radar cannot observe plasma waves, which are strongly associated with ion acceleration and ion outflow in high altitudes. However, powerful spectra with strongly asymmetric features, which may be caused by plasma instabilities, have been frequently observed with IS radars. Figure 1.7 shows the typical examples of powerful spectra. The main characteristics of the observations are that one of the ion-acoustic shoulders of the IS spectra is strongly enhanced. At certain altitudes, both sides of the spectra can be simultaneously enhanced during the time the radar takes to integrate its signal. These characteristic ion lines have been called the naturally enhanced ion-acoustic lines (NEIALs). The statistics seem to indicate that the upper shoulder (ion-acoustic waves going downward) is more frequently enhanced than the lower shoulder (waves going upward) at altitudes below 300 km. Conversely the lower shoulder is enhanced more frequently at altitudes exceeding 450 km [*Rietveld et al*., 1991, 1996]. At altitudes between 300 and 450 km, neither of the shoulders dominated the statistics.

A theoretical explanation for the generation of NEIALs is still a matter of debate. Two main classes of physical processes have been advanced so far. The first class relies on relative drifts between the thermal species in the plasma to excite the unstable waves. *Foster et al*. [1988], *Rietveld et al*. [1991], and *St.-Maurice et al.* [1996] proposed the ion-acoustic current driven instability [*Kindel and Kennel*, 1971] as the physical process producing NEIALs. However, the required current densities would have to be of the order of 1 mA m^{-2}, which has never been reported with direct observations. Although a relative drift between two ion populations can also reproduce NEIALs theoretically [*Wahlund et al*., 1992b], the required drift velocity greatly exceeds the ion sound speed.

The second mechanism producing NEIALs is enhanced ion-acoustic fluctuations due to parametric decay of Langmuir waves [*Forme,* 1993]. In this case, the ion-acoustic waves would be produced by the non-linear cascade of plasma waves. Low-energy precipitating electrons would first excite electron plasma waves, which by cascade would then produce secondary plasma and ion-acoustic waves. The parametric decay of beam-induced Langmuir waves has been observed in-situ using the Freja satellite [*Stasiewicz et al*., 1996]. Using the weak turbulence approximation, *Forme* [1999] modeled the spectral signature in which the parametric decay of beam driven Langmuir waves can enhance the right, the left, or both ion lines simultaneously as observed. In addition, *Cabrit et al*. [1996] showed that enhanced power due to NEIALs can be seen by the EISCAT VHF radar (224 MHz and $k_{VHF} \approx 9.4$ m^{-1})

while it is not observed by the EISCAT UHF radar (931 MHz and $k_{UHF} \approx 39.1$ m^{-1}) when both radars simultaneously view the same ionospheric regions. In this parametric decay model, the relative spread of the ion-acoustic *k* spectrum is determined essentially by the spread of the electron beam. Hence this parametric decay model has a possibility to explain the result from the VHF/UHF radar. However, we have not known whether the characteristics of the *k*-dependence is frequently observed or not, because the previous result was only a case study.

1.6 Purpose of Thesis

In this thesis, we investigate three aspects of ion upflow phenomena in order to understand the generation mechanisms of ion upflow. The first is to investigate regions where ion upflow occurs. The second is to investigate the relation between ion upflow and heating. The third is to investigate the characteristics of NEIALs, which are strongly related to ion upflow and may be caused by plasma instabilities. It is again noted that the ion upflow in the polar topside ionosphere is not a continuous outflow phenomenon of ionospheric light ions, called the polar wind, but an outflow phenomenon of ionospheric heavy ions such as NO^+ and O_2^+ accompanied by their transient heating. The heating mechanisms of ion upflow are likely to differ from those of ion outflow observed in the magnetosphere, although it is still not well understood how the ion upflow at high latitudes relates to the magnetospheric ion outflow.

Recently, it has been suggested that frictional heating inputs are usually of secondary importance, and the predominant source driving ion upflows seems to be soft (< 0.5 keV) electron precipitation [*Horwitz et al*., 1997, *Kundsen et al*., 1998]. The production mechanism of the ion upflow should be related to the free energy supplied by particle precipitation. Typical energy and flux density of the particle precipitation are different depending on the magnetospheric regions. In order to understand the ion upflow phenomena, it is important to determine in which regions of the dayside magnetosphere ion upflow occurs. *Nilsson et al*. [1994] found from simultaneous observations by the Søndre Strømfjord IS radar and the Freja satellite that some ion upflow events occur in the topside ionosphere of the cusp. These ion upflows were seen in the cusp under several conditions, such as the stable cusp, boundary cusp and storm cusp [*Nilsson et al*., 1996]. However, very little is currently known about whether ion upflow can occur in other dayside plasma regions or not. For example, the answer to the question of whether the ion upflow occurs in the mantle or LLBL is not known as is either the question of whether it also occurs in the dayside closed field line regions. A

systematic study of the dayside ion upflow is thus necessary to assess the regions where ion upflows occur.

The EISCAT Svalbard radar (ESR), which was constructed in Svalbard (invariant latitude 75.2˚ N) in 1996, allows us to study the high latitude ionosphere connected to the several magnetospheric regions. In order to understand the generation mechanisms of ion upflow phenomena in the dayside ionosphere, we determine, using approximately 170 ESR and DMSP satellite simultaneous data samples, in which regions of the magnetosphere and under what conditions the ion upflow occurs. This will be presented in Chapter 3.

Previous studies with the IS radars investigated the relation between ion anisotropy and ion upflow around the *F* region where ions start to flow up. However, in order to understand heating mechanisms associated with ion upflow, it is essential to investigate the velocity distribution of ions at the topside ionosphere where ions flow fully upward. Combined ESR and EISCAT VHF radar observations provide us with an opportunity to investigate the ion upflows and anisotropy at the topside of the *F* region. We hence investigate the relation between ion upflow and the heating process using data obtained from the simultaneous ESR and EISCAT VHF radar observations. They will be presented in Chapter 4.

Plasma instabilities as well as soft electron precipitations are considered to drive ion upflow. As related phenomena, NEIALs are seen in IS signals and the causes of these signals are proposed using various plasma instabilities. To know whether and how the cross section of NEIALs depends on the wave vector *k* may enable us to distinguish between such plasma instabilities. *Cabrit et al*. [1996] first discussed the *k*-dependence of the NEIAL cross section using the EISCAT VHF and UHF systems simultaneously. *Buchert et al*. [1999] made use of data recorded separately from different receiver channels of the ESR (500 MHz and $k_{ESR} \approx 21$ m^{-1}), which are spaced over frequency intervals of 2 MHz. They suggested from one case study that the power of NEIALs varies strongly with wavelength. Such a strong dependence of *k* may be explainable by a model involving the parametric decay of beam-driven Langmuir waves [*Forme*, 1993]. In order to investigate the characteristics of the NEIALs statistically, we utilize a larger database of NEIALs events and also compare their power characteristics with those of real satellite echoes. This will be presented in Chapter 5.

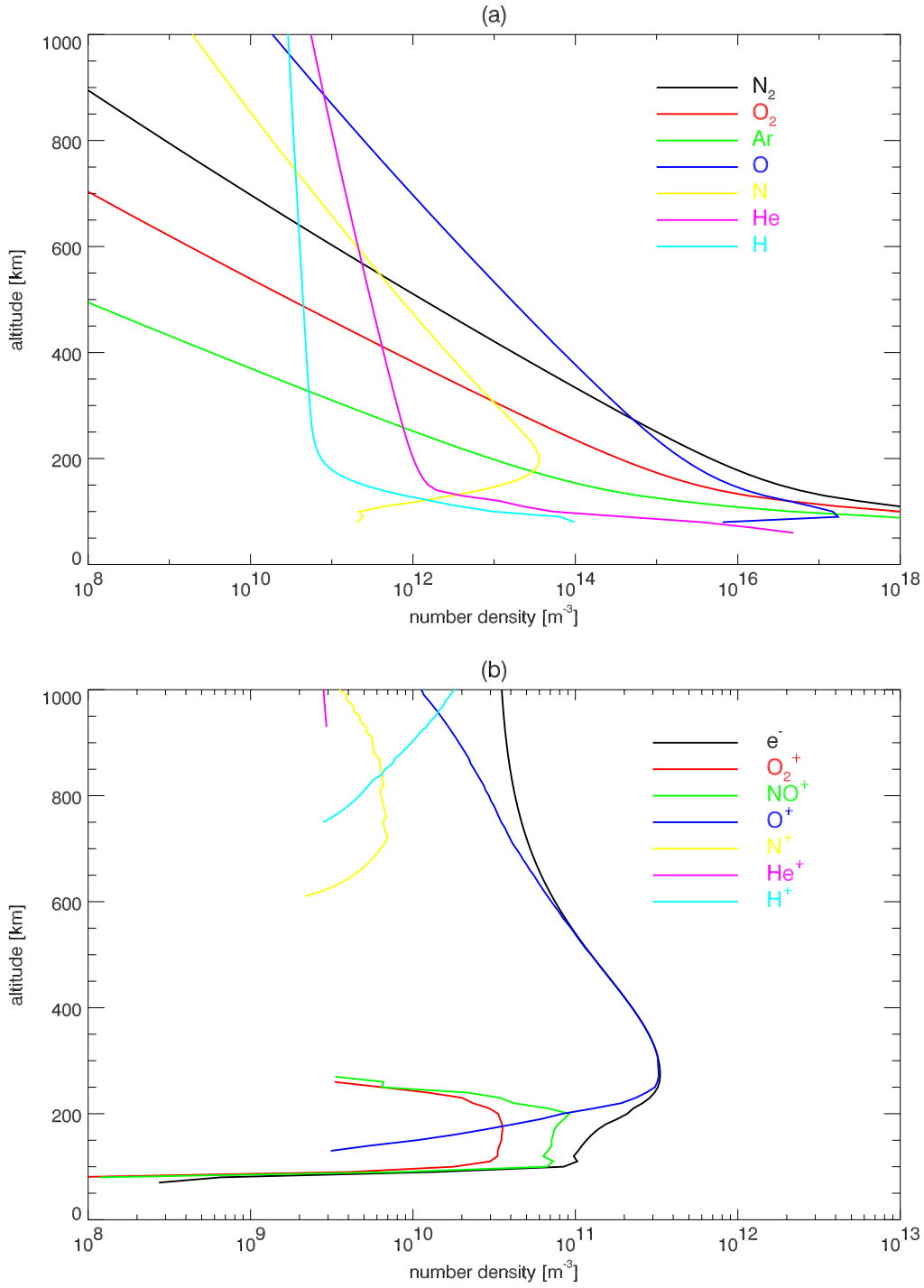

Figure 1.1: Height profiles of the number density of different neutral species (a) and electron and different ion species (b) below 1000 km altitude above Longyearbyen, Norway (78.2° N, 16.0° E) at 0900 UT on July 6, 1998. The height profiles of different neutral species are calculated using the MSIS 90 model [*Hedin*, 1991] and electron and different ion species using the IRI 95 model [*Bilitza*, 1997].

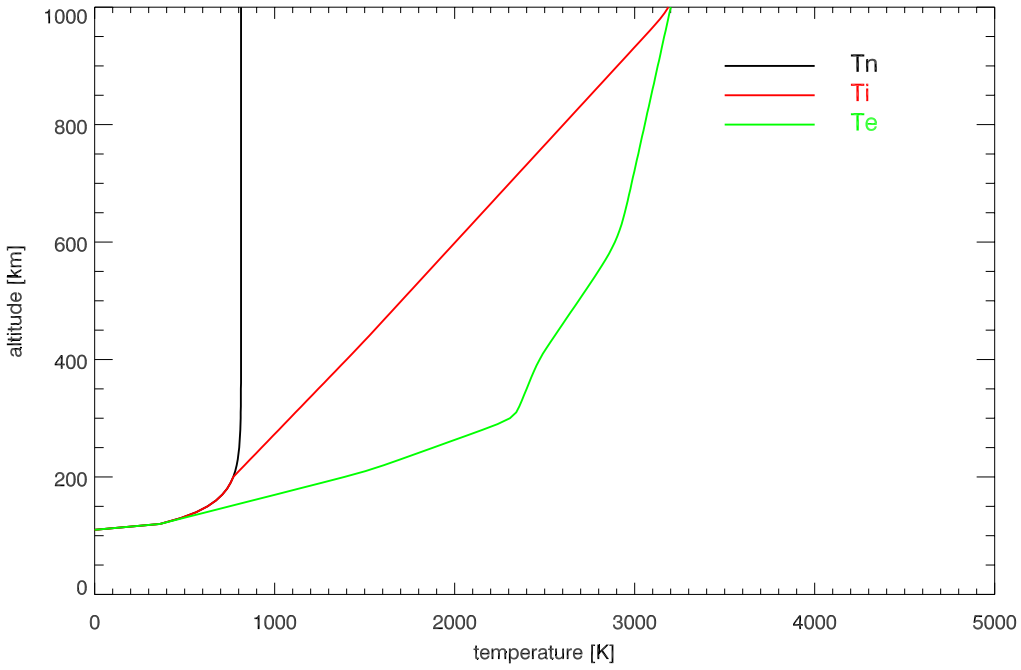

Figure 1.2: Height profiles of the temperature of neutral particles, ions, and electrons below 1000 km altitude above Longyearbyen, Norway (78.2° N, 16.0° E) at 0900 UT on July 6, 1998. The height profiles are calculated using the IRI 95 model [*Bilitza*, 1997].

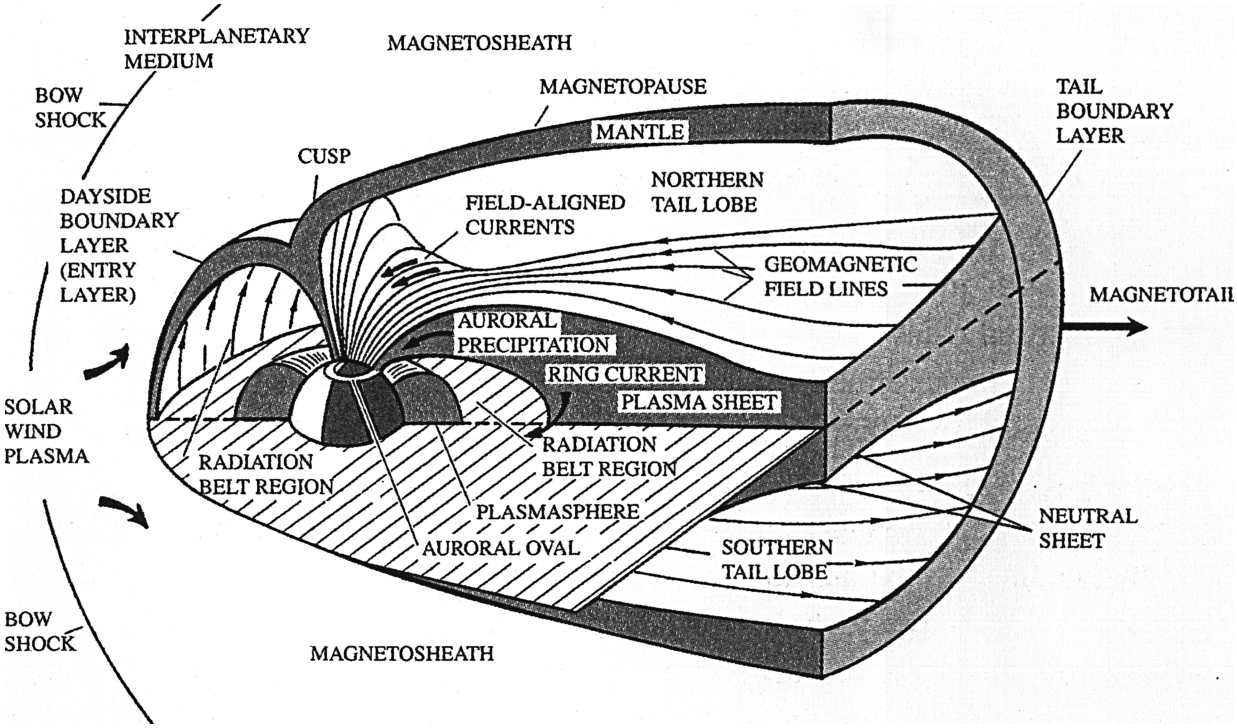

Figure 1.3: Schematic diagram of the Earth's magnetosphere showing the various regions and boundaries [After *Roederer*, 1981].

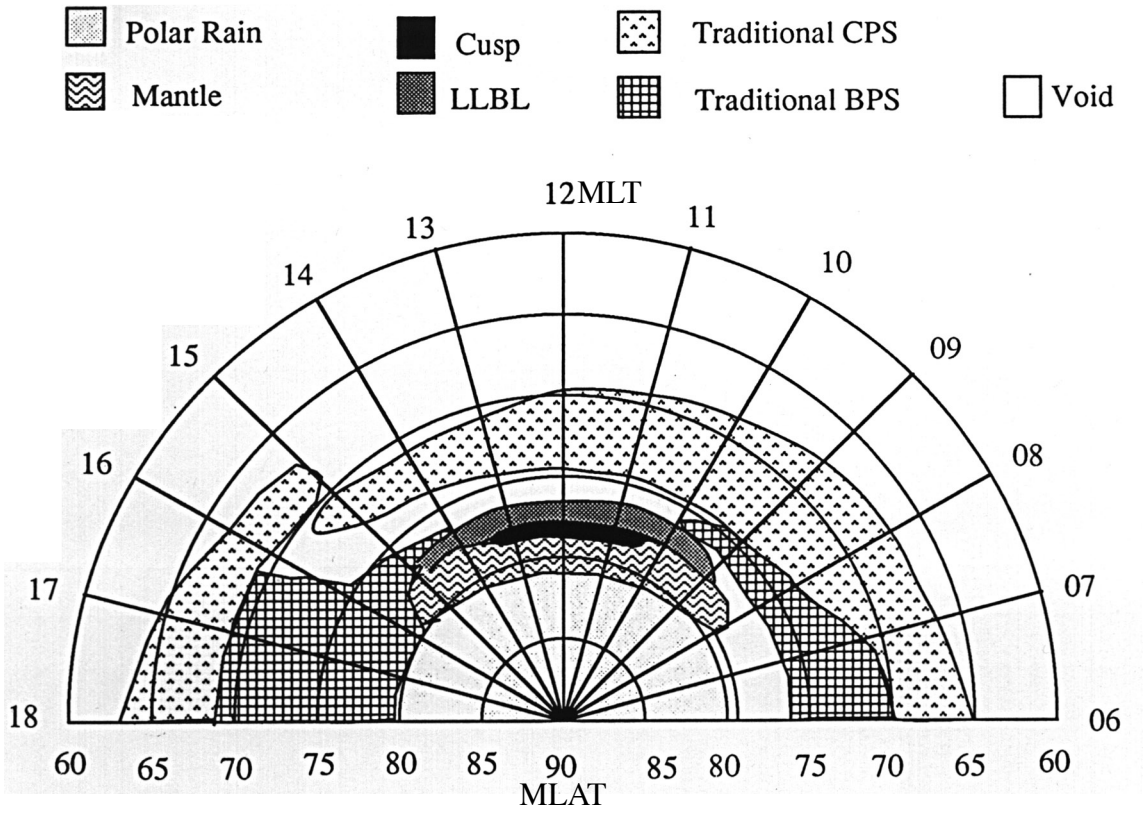

Figure 1.4: A map of the ionosphere to the magnetosphere based on plasma characteristics as functions of magnetic latitude (MLAT) and magnetic local time (MLT) [After *Newell and Meng*, 1992].

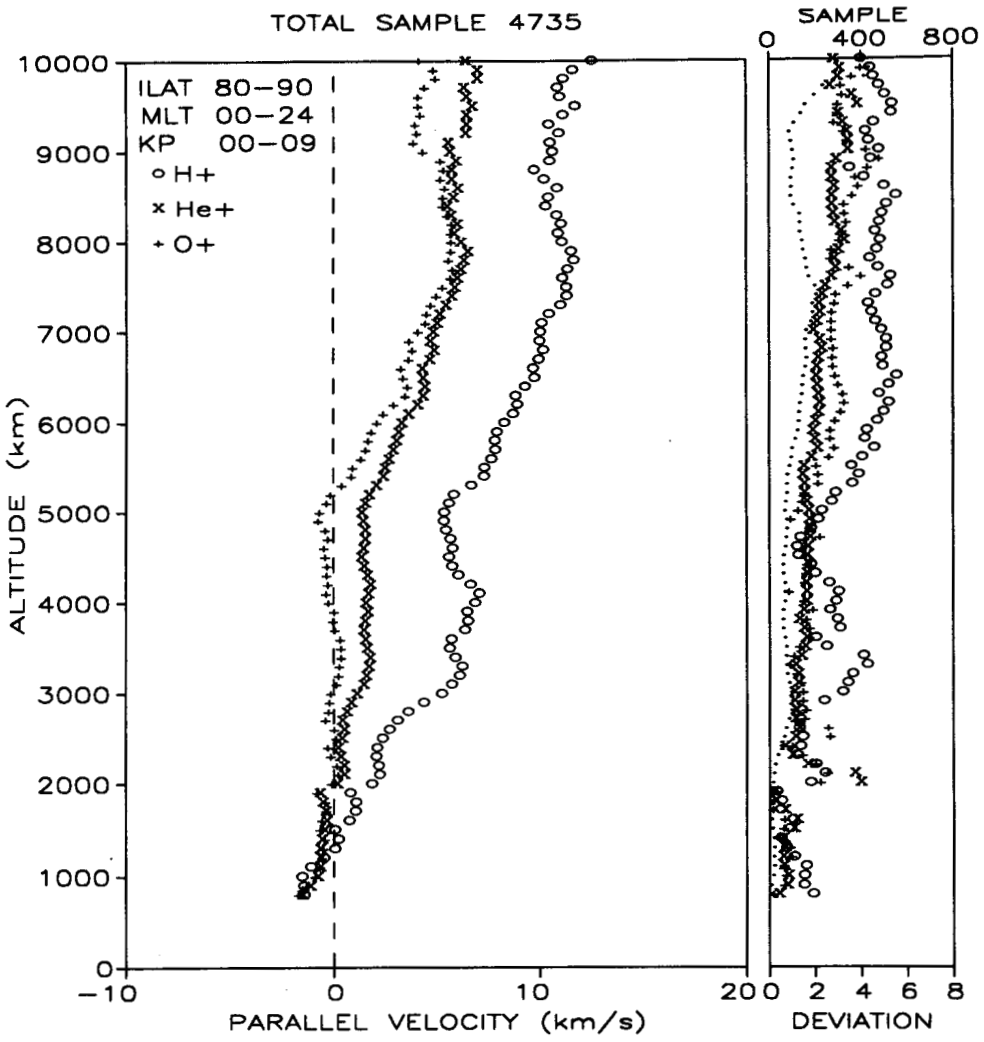

Figure 1.5: Parallel ion velocity of the polar wind as a function of altitude, averaged over all magnetic local times, all *Kp* levels, and all invariant latitudes above 80°. (open circles indicate) H^+ (crosses) He^+, (and pluses) O^+. (Left) Averaged ion velocity; (right) standard velocity deviation (bottom abscissa) and the number of data samples (top abscissa) [After *Abe et al.*, 1993].

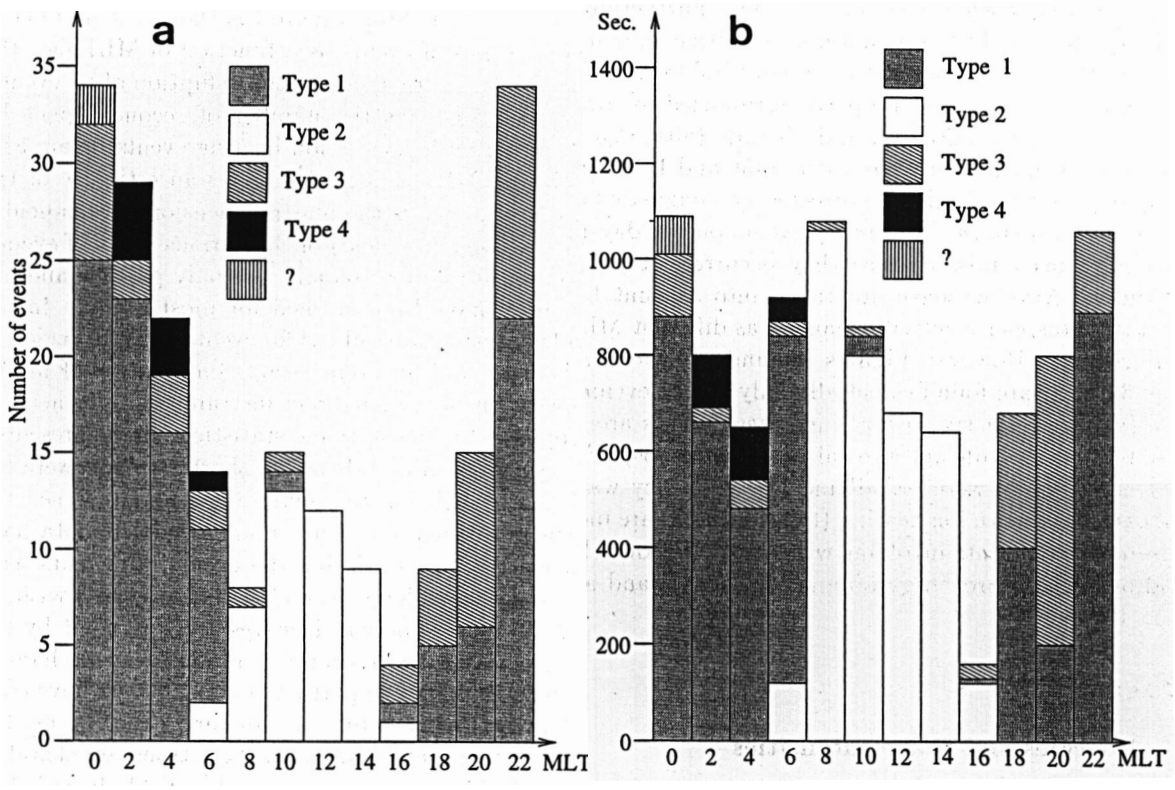

Figure 1.6: Different types of ion heating events observed with the Freja satellite near 1700 km height during about 1300 passes as a function of magnetic local time (MLT): (a) number of events and (b) the number of seconds spent in each type of event. Type 1 and 2 are both associated with broadband low-frequency waves, type 3 is connected with auroral electron and waves near half of the hydrogen gyro frequency or waves around the frequency of the lower hybrid wave, while type 4 is associated with precipitating H^+ or O^+ and around the frequency of the lower hybrid wave [After *André et al.*, 1998].

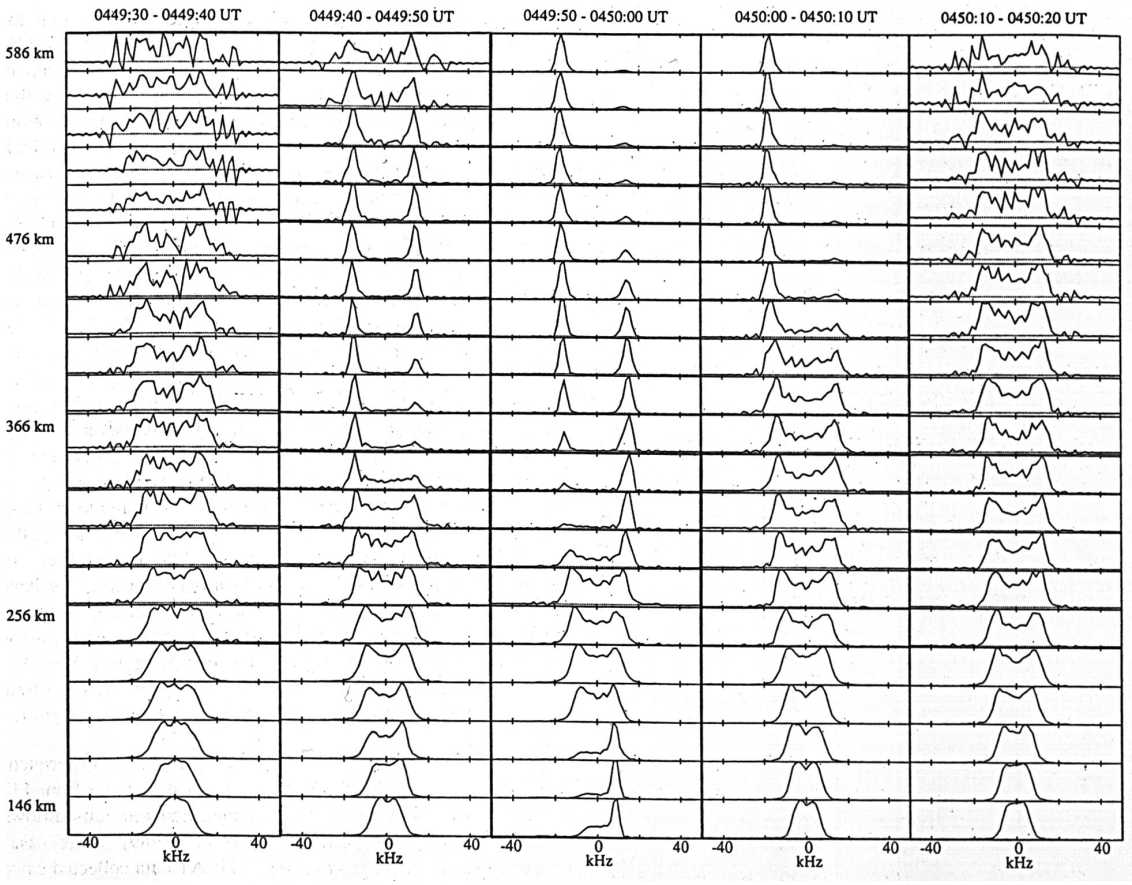

Figure 1.7: Examples of IS spectra at the EISCAT UHF radar. A sequence of 5 successive 10 sec data intervals showing how the long-pulse spectra change from normal to anomalous and back again. Each spectra is normalized [After *Rietveld et al.*, 1991].

Chapter 2

Instruments

In this thesis, we mainly utilized datasets obtained from the EISCAT radars and the DMSP satellites. In this chapter, these instruments are briefly described.

2.1 EISCAT Radars

The European Incoherent Scatter (EISCAT) scientific association is a cooperative project between seven countries: Germany, Finland, France, Japan, Norway, Sweden, and the United Kingdom. EISCAT is administered from the Headquarters in Kiruna, Sweden and has operational sites at Tromsø (Norway), Kiruna (Sweden), Sodankylä (Finland) and Longyearbyen (Svalbard). Geographical positions of the EISCAT radar sites and operating parameters of the EISCAT radars are shown in Figure 2.1 and Table 2.1, respectively. The EISCAT experiment has been divided into 2 groups: Common Programmes (CP), where the data are immediately available to all, and Special Programmes (SP), where the use of the data is restricted to particular users for one year. Both programs are conducted by all seven associates.

The facility at Tromsø consists primarily of two radars (at UHF and VHF frequencies). The UHF radar is a tristatic radar operating at 931 MHz with its transmitter at Tromsø and receivers at Tromsø, Kiruna, and Sodankylä. The VHF radar operates at 224 MHz with both the transmitter and receiver at Tromsø. The UHF radars have parabolic 32m antennas that are fully steerable both in azimuth and elevation, while the VHF radar has four $40\mathrm{m}\times30\mathrm{m}$ segments of a cylindrical antenna that are mechanically steerable between a vertical and 60°

zenith angle to the north. Additionally, the VHF segments can be individually phased up to 14.8° from the bore-sight direction. The UHF radar has been operating since 1981 and the VHF radar since 1987.

The EISCAT Svalbard radar (ESR), located at Longyearbyen, consists of two antennas. The 32m steerable antenna has been operating since 1996, followed by the installation of 42m antenna which was completed in 1999. The 42m antenna is permanently directed parallel to the local geomagnetic field. Both antennas operate at 500 MHz and the output of the transmitter can be switched between the two antennas at 3.2 sec at the minimum, allowing experimenters to make almost simultaneous measurements on both the 32m steerable antenna and the 42m fixed dish.

The ESR has mainly used three radar code designs, called GUP0, GUP3, and TAU0 in order. We describe these radar code designs in detail, because we have utilized data obtained from these different radar code designs together in this thesis, mainly in Chapter 3.

First, the GUP0 is a basic long pulse (LP) code and mainly intended for the *F* region/topside observations, between 123 km and 921 km. Figure 2.2a shows the timing diagram of 8 channels for the GUP0. In every cycle, long pulses are transmitted on 4 frequencies. The pulse length of the transmitted three pulses is $320\,\mu$sec, which corresponds to a range resolution of 54 km. The pulses provide range coverage from 180 to 921 km. The last pulse is shortened to $150\,\mu$sec in an effort to reduce ground clutter effects. The range resolution of the last pulse is approximately 23 km and the pulse provides range coverage from 123 to 750 km. The gate separation of the GUP0 is 3 km in length, correspond to the receiver's sampling rate of $20\,\mu$sec. The pulses and channels for the GUP0 are also summarized in Chapter 5. This GUP0 had been used for test experiments and CP of the ESR from March 1996 until May 1998.

Secondly, the GUP3 is designed for both the *E* and *F* region observations. Figure 2.2b shows the timing diagram of 4 channels for the GUP3. In every cycle, one LP and one alternating code (AC), by use of a $16\times 40\,\mu$sec code, are transmitted on 2 frequencies. The pulse length of the LP is $640\,\mu$sec, corresponding to a range resolution of 108 km. The range coverage of the LP is between 150 and 900 km. The range resolution of the AC, derived from range ambiguity functions, is approximately 3 km at maximum. The range coverage of the AC is between 20 and 750 km. The gate separation of both the LP and AC of the GUP3 is 3 km in length as well as that of the GUP0. This GUP3 had been used for CP of the ESR from August 1998 until March 2000.

Finally, the TAU0 has been used for CP of the ESR since the GUP3, March 2000. The TAU0 is also designed for both the *E* and *F* region observations, but it utilizes two alternating codes (ACs), by use of a $15 \times 64\,\mu$sec code. Figure 2.2c shows the timing diagram of the ACs for the TAU0. One AC has a range coverage from 212 to 1306 km and the other one from 58 to 1153 km. The range resolution of both the ACs for TAU0 is 2.4 km at maximum, which is the same as the gate separation of the TAU0 (2.4 km in length).

These incoherent scatter (IS) radars use powerful transmitters, large antennas and sensitive receivers to measure the spectral characteristics of electromagnetic radiation scattered from electrons in the ionized parts of the Earth's atmosphere at altitudes between approximately 80 and 1500 km. A range of ionospheric parameters is recovered by iteratively fitting theoretical spectra to the received data [e.g., *Lehtinen and Huuskonen*, 1996]. The basic parameters measured are electron density and temperature, ion temperature, and ion drift velocity.

2.2 DMSP Satellites

The Defense Meteorological Satellite Program (DMSP) satellites are in a near polar orbit, and sun synchronous at an altitude of approximately 840 km. Each satellite has an orbital period of approximately 101 minutes. Each DMSP satellite is loaded with a particle energy spectrometer (called SSJ/4), visible and infrared sensors, an ion drift meter and other related equipment.

The DMSP SSJ/4 particle detectors were designed to measure the flux of precipitating electrons and ions as they enter the Earth's upper atmosphere. They consist of four electrostatic analyzers that record electrons and ions between 30 eV and 30 keV. The two low-energy detectors consist of 10 channels centered at 34, 49, 71, 101, 150, 218, 320, 460, 670, and 960 eV. The high-energy detector measures particles in 10 channels centered at 1.0, 1.4, 2.1, 3.0, 4.4, 6.5, 9.5, 14.0, 20.5 and 29.5 keV. Each detector pauses at each channel for 0.09 seconds while switching from a high-energy channel to a low one. A complete cycle is sampled each second, which corresponds to a spatial resolution of approximately 7 km. The nominal response efficiency is 50% at a value of 10% of the central energy for that channel.

Table 2.1: Parameters of the EISCAT Radars

Location	Tromsø		Kiruna	Sodankylä	Longyearbyen
Geographic Coordinates (˚)	69.6 N		67.9 N	67.4 N	78.2 N
	19.2 E		20.4 E	26.6 E	16.0 E
Geomagnetic Inclination (˚)	77.5 N		76.8 N	76.7 N	81.5 N
Invariant Latitude (˚)	66.2 N		64.5 N	63.6 N	75.2 N
Band	VHF	UHF	UHF	UHF	UHF
Center Operating Frequency (MHz)	224	931	931	931	500
Max. Bandwidth (MHz)	3	8	8	8	10
Channels	8	8	8	8	8
Peak Power (MW)	3.0	2.6	-	-	1.0
Average Power (MW)	0.3	0.3	-	-	0.25
Pulse Duration (msec)	0.001-2.0	0.001-1.0	-	-	0.001-2.0
Gain (dB)	46	48	48	48	42.5
System Temperature (K)	250-350	90-110	30-35	30-35	80-85

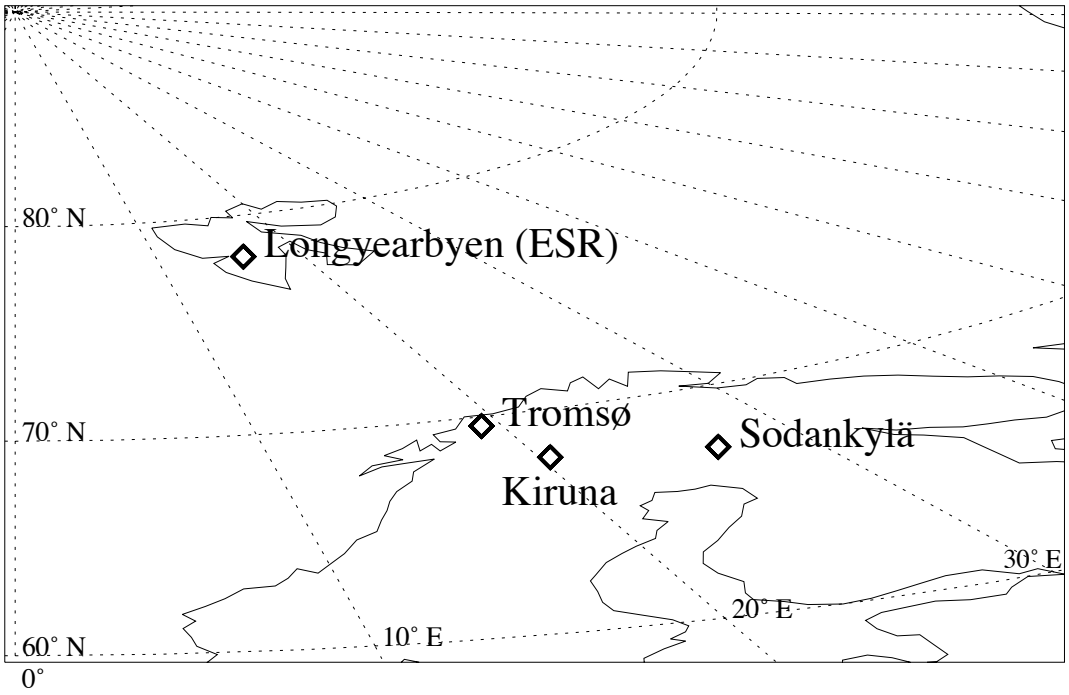

Figure 2.1: Geographical locations of the EISCAT radar sites.

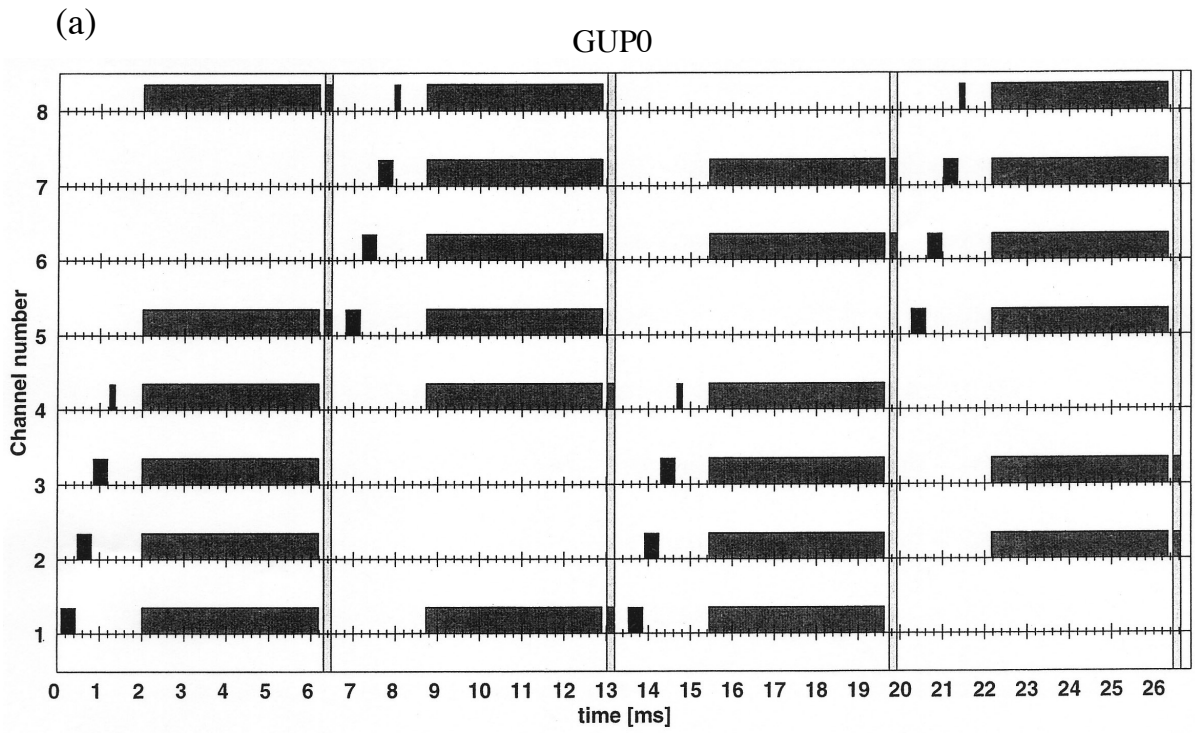

Figure 2.2: Timing diagram for (a) GUP0, (b) GUP3, and (c) TAU0.

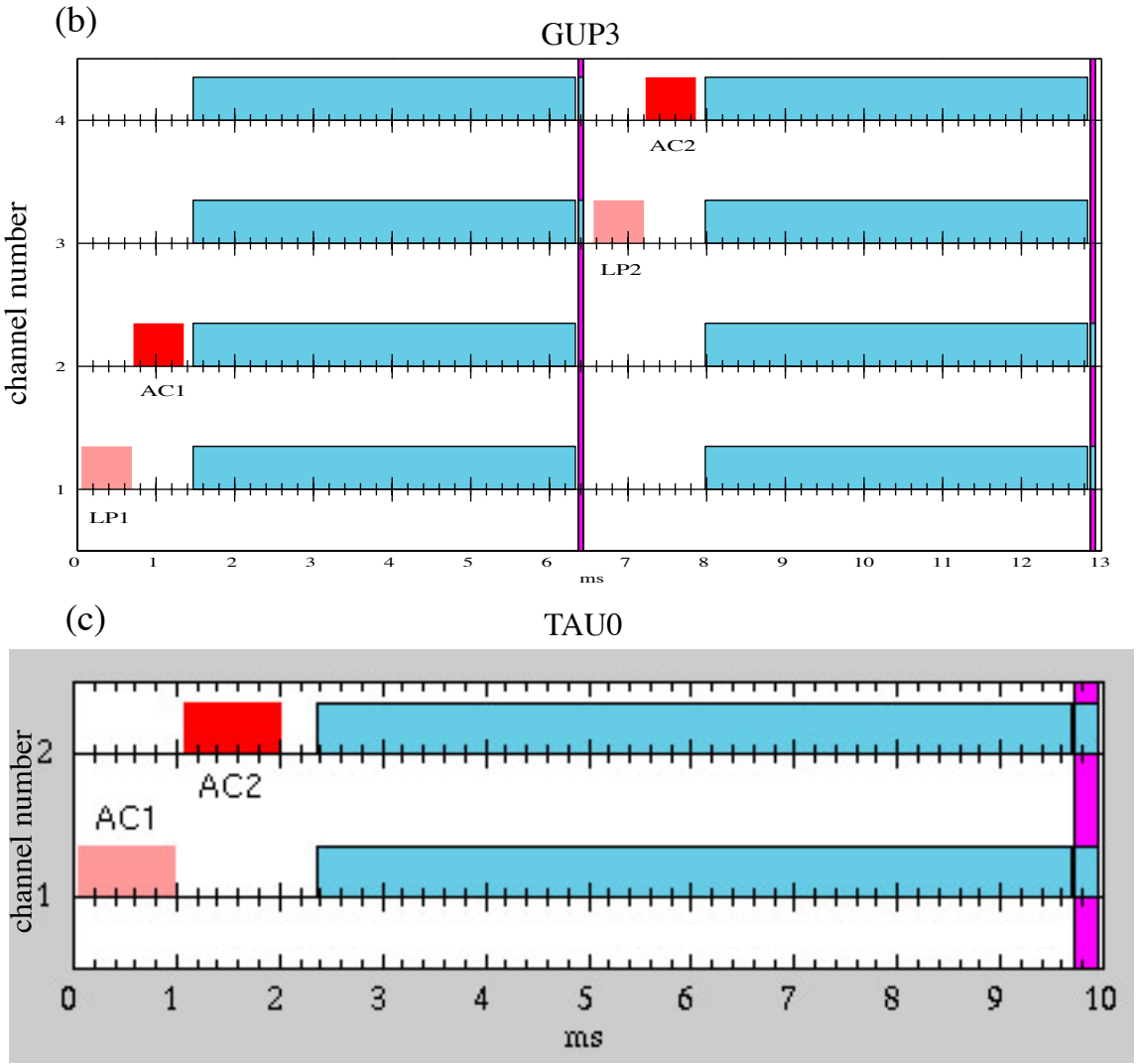

Figure 2.2: (continued)

Chapter 3

Occurrence Regions of Ion Upflow in the Dayside Ionosphere

The aim of this chapter is to understand the generation mechanisms of ion upflow phenomena in the dayside ionosphere. In particular, this chapter tries to determine, using simultaneous data between the EISCAT Svalbard radar (ESR) and DMSP satellites, in which regions of the magnetosphere and under what conditions the ion upflow occurs. Section 3.1 describes the instruments and data. Section 3.2 describes the observational results. The occurrence regions of ion upflow in the dayside ionosphere are discussed in Section 3.3.

3.1 Instruments and Data

In order to examine magnetic field-aligned (FA) ion upflow in the polar ionosphere, we have used only FA data obtained from ESR experiments of several modes, Common Program 1 L (CP-1L) mode, Common Program 2 L (CP-2L) mode and several Special Program (SP) modes where the antenna is either continually or occasionally pointed to the magnetic field-aligned direction. The total number of observations used in this study is approximately 170 days occurring from January 1998 to November 2001. The integration time period is 2 min, except for 1 min integrated CP2L data during September 21 - 23, 1998, and 4 min integrated CP2L data during February 5 - 26, 2001. Although pulse codes for the topside ionosphere are different between the long pulse (LP) of GUP0 and GUP3 and the alternating code (AC) of TAU0, we have used the same gate interval of 36 km for both LP and AC. The differences

between the pulse codes are described in Chapter 2. Spectra in the incoherent scatter (IS) radar data sometimes include echoes from satellites or space debris, and naturally enhanced echoes [*Rietveld et al*., 1991], from which correct physical parameters cannot be obtained. We have hence excluded these data from the present study. We have also excluded poor quality data whose error values of the ion velocity and electron density exceed certain values.

Plasma particle data from the DMSP satellite provide information about which magnetospheric region –the cusp, low-latitude boundary layer (LLBL), mantle, Boundary Plasma Sheet (BPS), or Central Plasma Sheet (CPS)– the satellite is located in. Since statistically the cusp has a fairly wide longitudinally elongated shape [*Newell et al*., 1992; *Maynard et al*., 1997], we have selected simultaneous ESR and DMSP data where a DMSP satellite passed by within 350 km (equivalently within a one hour magnetic local time (MLT) span) from the magnetic field line of the ESR during the time period when the ESR is located between 0800 and 1600 MLT.

3.2 Results

We have investigated, by using simultaneous events between the ESR and DMSP satellites, in which regions of the magnetospheric plasma regions ion upflow occurs. The dayside specific magnetospheric plasma regions here are the cusp, LLBL, mantle, BPS, and CPS, which are distinguishable from plasma properties measured from the DMSP satellites based on the methods proposed by *Newell et al*. [1988, 1991a, 1991b]. The classification of each region adopted in this study are summarized as follows:

1. “Cusp” can be detected by very high fluxes, particularly for ions. The ions typically have a spectral peak of differential energy fluxes of more than 10^8 eV cm^{-2} s^{-1} sr^{-1} eV^{-1}, which is higher than anywhere else in the auroral oval. Furthermore, low energy ion cutoff drop exists at least at 1 - 3 keV and below. Electron temperature is below 100 eV and the average energy of electron precipitation is below approximately 200 eV.

2. “LLBL” can be distinguished from those in the cusp by their hotter ions and electrons than those in the cusp. Electron temperature is typically less than 200 eV and the average energy of electron precipitation is less than approximately 400 eV. The ion fluxes are 10^6 - 10^7 eV cm^{-2} s^{-1} sr^{-1} eV^{-1}, which are smaller than those in the cusp by approximate factor of 10.

3. “Mantle” can be distinguished by the de-energized magnetosheath ions observable poleward of the dayside auroral oval. The ion temperature ranges from a few tens of a eV up to approximately 100 eV, and ion average energy is no more than a few 100 eV. The ion fluxes as well as those in the LLBL are smaller than those in the cusp.

4. “BPS” is classified as any soft region of electron precipitation except for the cusp, LLBL, mantle, and polar rain in the polar cap. The use of the term “soft” means electron average energy below 1 keV. This region resembles the nightside BPS; i.e., the ion precipitation shows no clear sign of a magnetsheath origin, electron temperatures are a few 100 eV, and spatially and spectrally structured electron spectra are common.

5. “CPS” is classified by spectrally smooth clouds of more than 1 keV electrons and ions, which is the probability of observing the extension of the nightside zones of hard precipitation.

Figure 3.1 shows the typical examples of each magnetospheric region observed from the DMSP satellites. The particle data are obtained from electrostatic analyzers that measure precipitating electrons and ions from 32 eV to 30 keV. Note that the ion energy scale is inverted. Figure 3.1a shows a conjunction event in the cusp at 0735 UT on July 6, 1998. The red arrow denotes the geomagnetic latitude of the ESR (75.2˚ N). The cusp, a 75.8˚ - 75.1˚ geomagnetic latitude (MLAT), is characterized by a strong peak in ion energy flux at approximately 1 keV and high number fluxes of ions. The electron spectral peak in the cusp is approximately 100 eV which is similar to the magnetosheath value. Immediately equatorward of the cusp is a region of LLBL. The LLBL is distinguished from the cusp by higher than average particle energies, and it has ion densities which are a few times smaller than those in the cusp. In Figure 3.1b, a conjunction event in the LLBL is seen at 1103 UT on February 12, 1999. The average energies of ions and electrons in the LLBL are 3 keV and 300 eV, respectively. The number fluxes of ions in the LLBL are reduced by a factor of approximately 5, but those of the electrons are similar to those of the cusp. Figure 3.1c shows a conjunction event in the mantle at 1054 UT on March 25, 1998. The mantle is recognized by lower energies when compared with the cusp. The ion densities in the mantle are a few times smaller than those in the cusp. The poleward low energy ion “plume” results from its entrance

into the magnetosphere until precipitating to undergo significant poleward $E \times B$ deflection [*Shelley et al.*, 1976; *Reiff et al.*, 1977]. As is also the case with the LLBL, soft electron precipitation (below 200 eV) has occurred in the mantle, although the number flux is smaller than that in the cusp around 74.5˚ MLAT. Figure 3.1d shows a conjunction event in the BPS at 0815 UT on February 8, 2001. In the BPS, a few keV and a few hundred eV electron precipitations coexist. Hence soft electron precipitation occasionally occurs in the BPS as shown in Figure 3.1d. Figure 3.1e shows a conjunction event in the CPS at 0905 UT on April 8, 1999. The CPS is recognized by a few keV electron precipitation. The electrons have drifted from the nightside plasma sheet. There is no soft electron precipitation in the CPS. Characteristic energies of ion precipitation such as those in the cusp, LLBL and mantle are not seen in the BPS and CPS.

Figure 3.2 shows height profiles of the electron temperature obtained from the ESR. Each plot from (a) to (e) corresponds to each conjunction event shown in Figure 3.1. The thick lines indicate electron temperature during the conjunction events marked as red arrows in Figure 3.1. The thin lines denote the background levels of the electron temperature. Each background level is different by time, season and solar cycle. We hence have defined the background electron temperature as a level of electron temperature under a quiet (no precipitation) condition that occurred at a time close to each conjunction event. Figure 3.2a shows a height profile of the electron temperature in the cusp shown in Figure 3.1a. The electron temperature in the cusp increases up to 5000 K at 500 km altitude, whereas the background electron temperature is approximately 3000 K at the same altitude. The electron temperature enhancement is also clearly seen in the LLBL (Figure 3.2b) and mantle (Figure 3.2c), although differences from the background levels are smaller than those in the cusp in Figure 3.2a. Figure 3.2d shows no difference between the electron temperature in the BPS and the background levels. The electron temperature is approximately 2000 K at 500 km altitude. The CPS in Figure 3.2e also shows no difference of electron temperatures.

Figure 3.3 shows height profiles of the field-aligned (FA) ion velocity obtained from the ESR. Each plot from (a) to (e) again corresponds to each conjunction event shown in Figure 3.1. The background FA ion velocity in each plot is also obtained as quiet (no precipitation) conditions and is approximately 0 m s^{-1}, but some fluctuations due to the low SNR exist above 550 km altitude. Figure 3.3a indicates an existence of a significant upward flow in the cusp. The upward flow commences from 350 km altitude and the FA ion velocity increases with a higher altitude, reaching 200 m s^{-1} at 600 km altitude. In the LLBL (Figure 3.3b) and mantle

(Figure 3.3c), height profiles of the FA ion velocity are similar to those in the cusp. The FA ion velocities in both the LLBL and mantle are more than 100 m s^{-1} at 600 km altitude. In the BPS (Figure 3.3d), ions hardly move toward the field-aligned direction below 550 km altitude. Above 550 km altitude, ions flow slightly but not continuously upward. In the CPS (Figure 3.3e), FA ion velocity is approximately 0 m s^{-1} below 700 km altitudes.

Figure 3.4 shows FA ion velocity distributions in these magnetospheric regions. We have defined one "event" as a set of 2 min integrated ESR data, which is obtained within ± 5 min from a conjunction time. A satellite pass conjunction thus provides us with 5 events in the case of the CP1L experiment. In the following, we use a unit of "events" to count the ion upflow phenomena. This unit is defined as follows: Assume that a conjunction between the ESR and DMSP happens at t_0, and t_0 - 5 min < t < t_0 + 5 min as the conjunction time. This is equivalent to the assumption that the ionospheric locations of the plasma regions observed by DMSP do not change during this 10 min time period. We determine the FA ion velocities of ion upflow within each of the 2 min intervals.

The abscissa in Figure 3.4 shows the FA ion velocity averaged over altitudes between 400 and 700 km observed from the ESR. The quantified bin of the FA velocity used here is 50 m s^{-1}. The ordinate is the number of events in each FA ion velocity bin. First, there are 23 conjunction events in the cusp (Figure 3.1a). For all of these events, ion upflows occur, whose velocity ranges from approximately 100 to 300 m s^{-1}. Secondly, there are more than 80 events in the LLBL (Figure 3.1b). Figure 3.1b clearly shows that most of the events in the LLBL (or cleft) have an upward FA ion velocity. In particular, half of the events have an upward FA ion velocity of more than 100 m s^{-1}. It should be noted that a few events have a negative FA ion velocity showing that ion upflow does not always occur in the LLBL. The peak of the distribution of FA ion velocity in the LLBL is at approximately 100 m s^{-1}. Thirdly, 70 conjunction events are found in the mantle (Figure 3.1c). The distribution of FA ion velocity in the mantle is similar to that in the LLBL. Ion upflow with the FA ion velocity of more than 100 m s^{-1} is frequently observed in the mantle. Downflow with FA ion velocity of less than -200 m s^{-1} is also observed in this region. On the contrary, the FA ion velocity in the BPS and CPS is fairly distributed around 0 m s^{-1}, implying that there is a smaller probability of having (intense) ion upflow in these two regions.

Figure 3.5 also shows the FA ion velocity distributions in these magnetospheric regions, and the figure adds the results of the case in which soft electron precipitation occurs to Figure 3.4. When the differential energy flux of electrons at 100 eV is more than 10^7 eV cm^{-2} s^{-1} sr^{-1}

eV^{-1}, the FA ion velocity distributions are shown in black color. In the cusp (Figure 3.5a), all events are associated with soft electron precipitation. The FA ion velocities are distributed to the upward direction. Almost all events in the LLBL (Figure 3.5b) are also associated with soft electron precipitation. But some events with the precipitation have small upward ion velocity (less than 100 m s^{-1}). In the mantle (Figure 3.5c), FA ion velocities with the soft electron precipitations are clearly distributed to the upward direction. In particular, FA ion velocities of more than 150 m s^{-1} are always associated with the soft electron precipitations. On the contrary, FA ion velocities without soft electron precipitations are distributed to the downward direction or to nearly 0 m s^{-1}. In the BPS (Figure 3.5d), there are many events in which soft electron precipitation exists and the FA ion velocity is small. The distribution of FA ion velocity in the BPS is obviously different from that in the mantle, although both the BPS and mantle often have soft electron precipitations. There is little precipitation of soft electrons in the CPS (Figure 3.5e), by definition.

3.3 Discussion

Ion upflow in the dayside is frequently observed from the ESR because of its latitudinal location. The simultaneous observations between the ESR and DMSP satellites show that ion upflow frequently occurs in the cusp, LLBL and mantle, but much less frequently in the closed field line regions such as the CPS/BPS precipitation. The characteristics do not change even when different (more strict) longitudinal criteria are adopted as a simultaneous observation between the ESR and DMSP satellites. *Nilsson et al*. [1996] have reported the ion upflows in several cusp types including equatorward boundary of the cusp. However, this paper for the first time demonstrates that ion upflow occurs in the regions connected not only to the cusp and cleft (LLBL) but also to the plasma mantle, and it less frequently occurs in the region connected to the BPS and CPS.

Almost all of the events in which average FA ion velocity is more than 100 m s^{-1} are associated with soft electron (< 0.5 keV) precipitation. In particular, there is good correlation between ion upflow and soft electron precipitation in the mantle. The soft electron precipitation is short burst electron precipitation [*Veselovsky et al*., 1995] or continuous precipitation with no gap between the cusp and mantle regions. The characteristics of the ion upflow in the mantle are the same as those in the cusp/cleft region. Hence the ion upflow in the mantle cannot be explained by heated ions originally flowing out of the cusp/cleft region

then drifting into the mantle by $E \times B$ drift. We conclude that the ionospheric region corresponding to the mantle region is also the occurrence region of ion upflow.

An analysis of DE 2 observations by *Seo et al.* [1997] found that at approximately 800 km altitude a quasi-inverse relationship is seen between the observed FA ion upflow velocities and the characteristic energy of the precipitating soft electrons (< 0.5 keV) for restricted ranges of electron energy flux. Several simulation models also show that soft particle precipitation can cause ion upflow in the topside *F* region [e.g., *Caton et al*., 1996; *Su et al*., 1999]. Soft particle precipitation causes neutral particles around the *F* region/topside ionosphere to ionize [e.g., *Millward et al*., 1999]. The precipitation also causes electrons around the *F* region/topside ionosphere to heat through Coulomb collisions with primary and secondary electrons. As a result, the ambipolar electric field, which is proportional to both the density and temperature gradients, becomes largely upward and works on ions as an upward force. We have described the effect of the ambipolar electric field on ion motions in detail in Appendix A.

However, there are little upflow events associated with soft precipitation in the BPS. Even if the criterion of the differential energy flux of electrons at 100 eV is changed from 10^7 to 10^8 eV cm^{-2} s^{-1} sr^{-1} eV^{-1}, the characteristics of the distributions of FA ion velocities in each region, especially the BPS, are not changed. The present results indicate that the relation of soft particle precipitation to ion upflow is different between the corresponding magnetospheric regions. DE 2 observations also show that the distribution of FA ion velocity associated with soft electron precipitation around 50 eV is scattered, and there are many cases with small FA ion velocity (in Figure3c in *Seo et al.* [1997]). Our results indicate that the small upward velocity events with soft particle precipitation are associated with the BPS region in the dayside. Thus the effect of soft particle precipitation on ion upflow may be different between the corresponding magnetospheric regions. The existence of heat fluxes by thermal electrons from the magnetosphere also plays a role in causing the difference between the regions, because electron temperature enhancement is not seen in the BPS (see Figure 3.2). *Caton et al*. [1996] shows that electron heat fluxes from the magnetosphere, as well as the soft particle precipitation, are the primary driver of ion upflow.

Ion upflow is rarely found in the regions corresponding to the CPS. A reason for this infrequent occurrence of the ion upflow in the CPS may be that the energy of electron precipitation is generally higher than that in the cusp, LLBL and mantle, and hence the electron precipitation in the CPS provides less energy at the higher altitude ionosphere where

the ion upflow is initiated, but rather it ionizes the *E* region atmosphere.

It may be worth pointing out that *Kozolovsky et al*. [2001] have shown that mean FA ion motions at 300 - 550 km were upward in a region equatorward of a postnoon arc around 16 - 17 MLT. They considered that the source of the postnoon arc might be located inside the LLBL or probably in the BPS, implying that the ion upflow they observed was located in the BPS. We leave it to a future work to establish how the occurrence regions of ion upflow in the dayside ionosphere continue in the dawn and dusk, and even in the nightside region.

3.4 Chapter Summary

We have examined the correspondence of dayside ion upflows to the various magnetospheric regions based on a statistical analysis using more than 100 simultaneous observations between the ESR and the DMSP satellites. The results obtained are summarized below.

1. Ion upflows occur not only in the cusp and cleft (the low-altitude portion of the LLBL) which have been considered as ion upflow regions, but also in the topside ionosphere connected to the mantle region. The ion upflows seldom occur either in the BPS or in the CPS at the dayside high latitudes. These results are important to understand the processes of ions escaping from the ionosphere to the magnetosphere.

2. Almost all events in which the average field-aligned (FA) ion velocity is more than 100 m s^{-1} are associated with soft electron precipitation (differential energy flux of electrons at 100 eV > 10^7 eV cm^{-2} s^{-1} sr^{-1} eV^{-1}). Although soft electron precipitation also exists in the BPS, the ion velocities are mostly less than 100 m s^{-1}. The present results indicate that soft particle precipitation is the predominant source driving ion upflow in the topside ionosphere, but it may work on ion upflow effectively in the higher latitudinal regions in the dayside and not in the BPS.

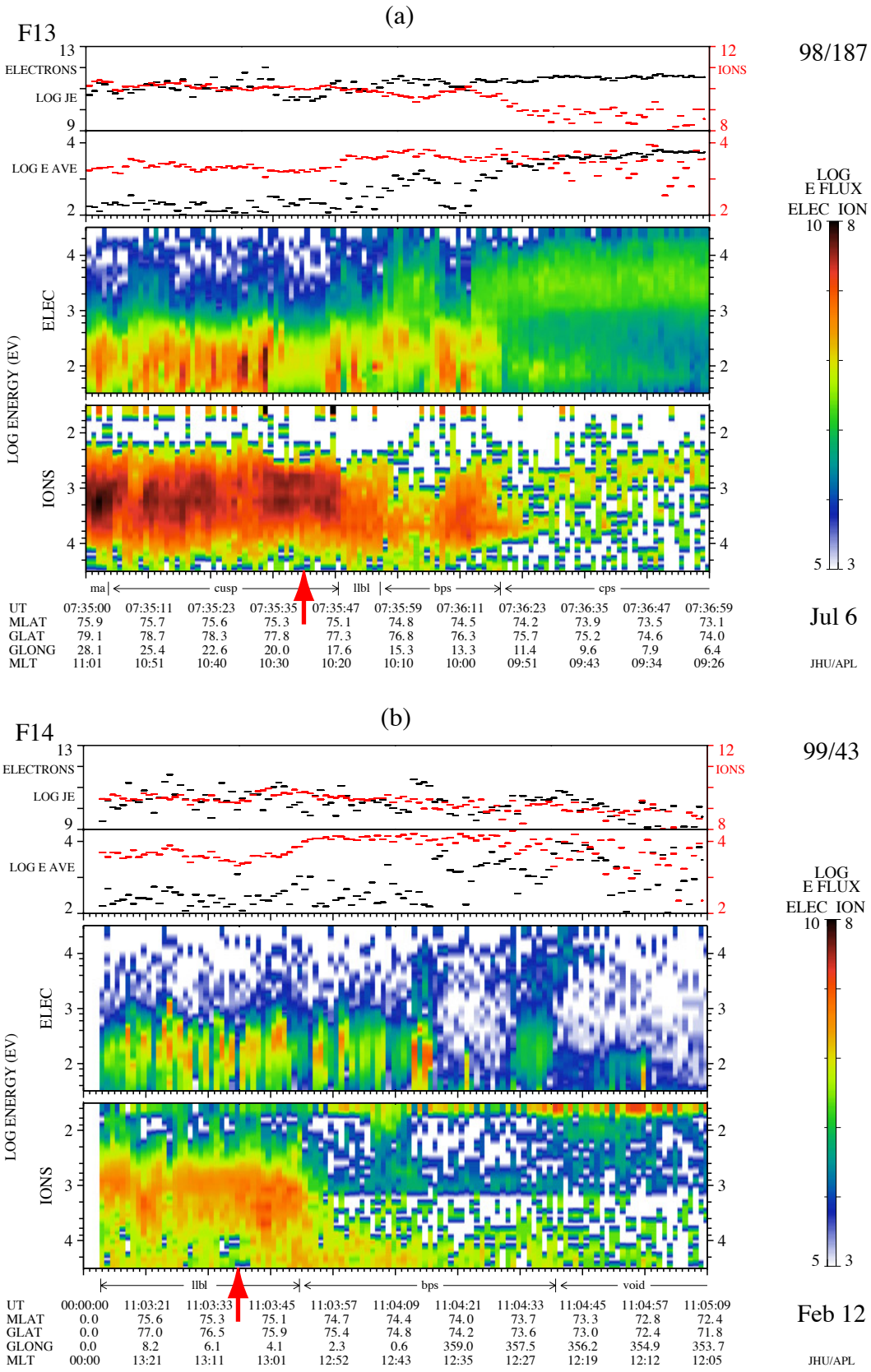

Figure 3.1: DMSP spectrograms including conjunction events with the ESR. Each conjunction event shows (a) cusp, (b) LLBL, (c) mantle, (d) BPS, and (e) CPS.

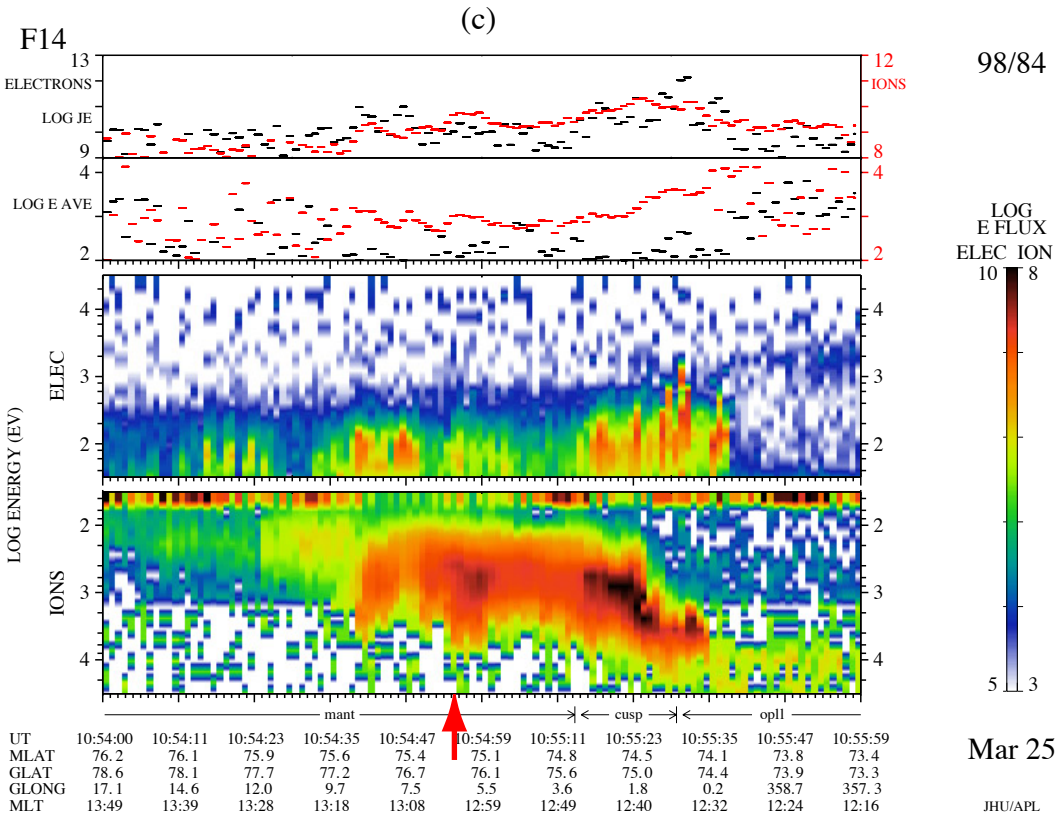

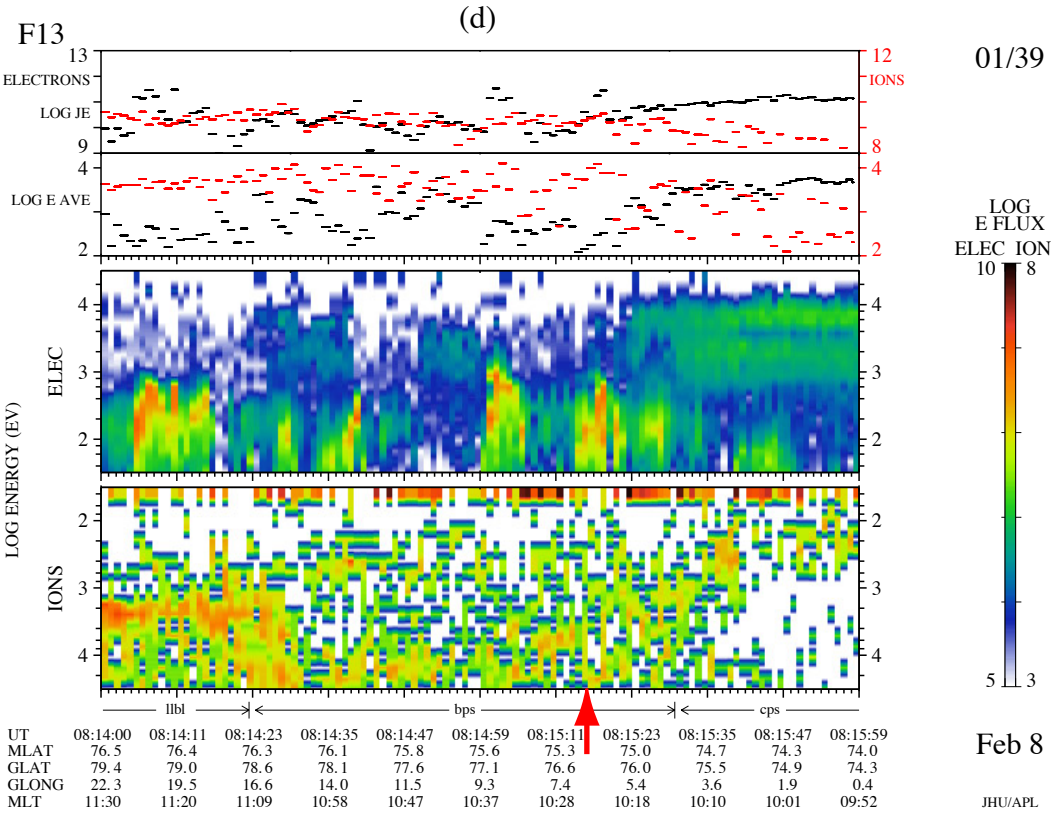

Figure 3.1: (continued)

(e)

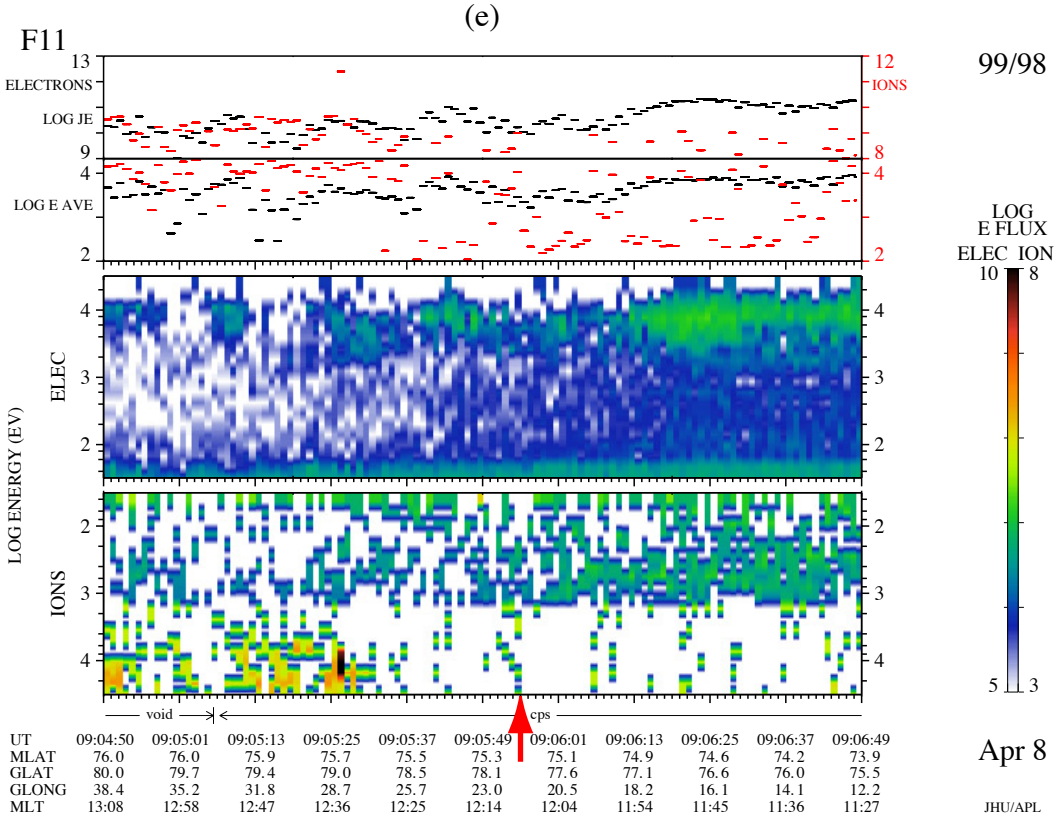

Figure 3.1: (continued)

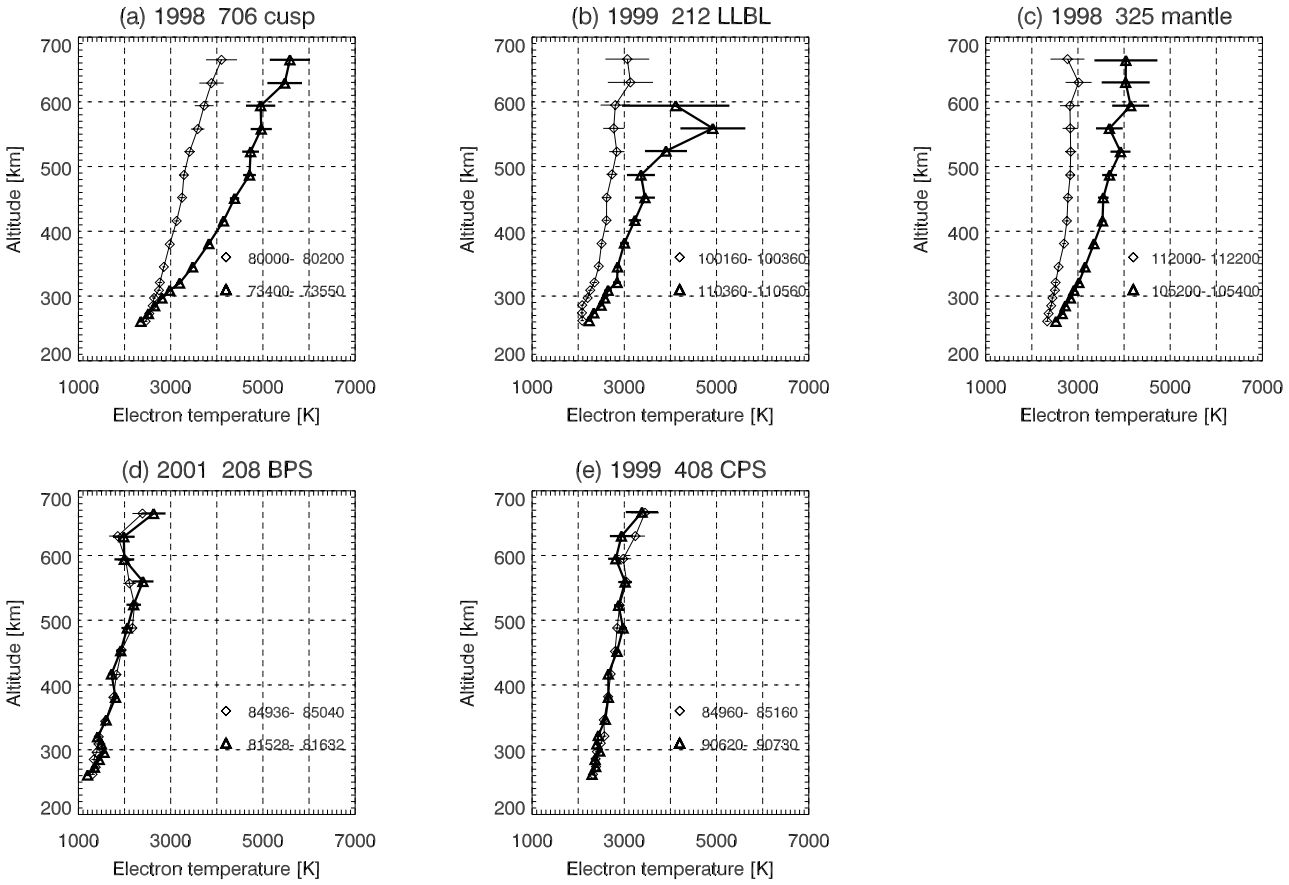

Figure 3.2: Height profiles of electron temperature at corresponding magnetospheric regions. Each conjunction event shows (a) cusp, (b) LLBL, (c) mantle, (d) BPS, and (e) CPS.

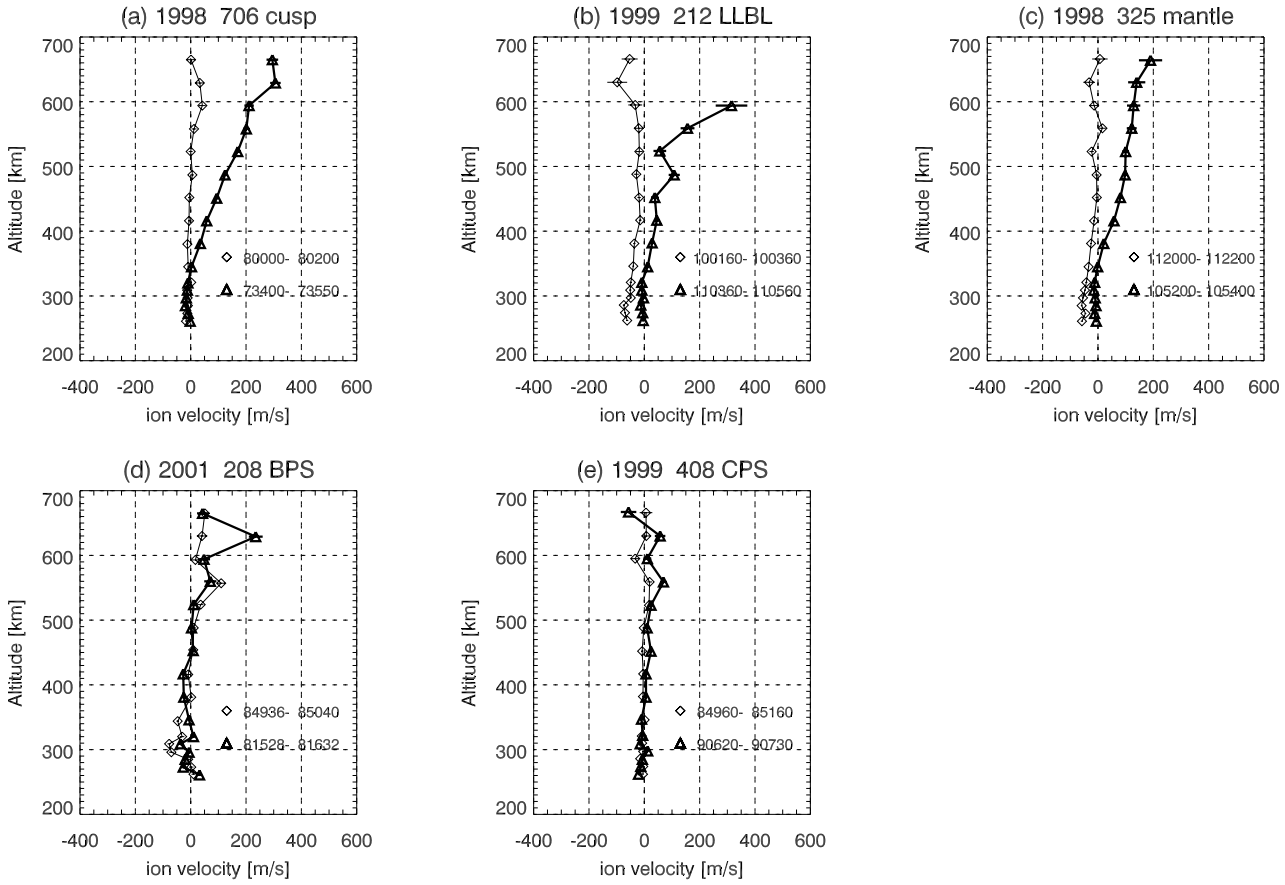

Figure 3.3: Height profiles of field-aligned (FA) ion velocity at corresponding magnetospheric regions. Each conjunction event shows (a) cusp, (b) LLBL, (c) mantle, (d) BPS, and (e) CPS. Positive ion velocity is in an upward direction.

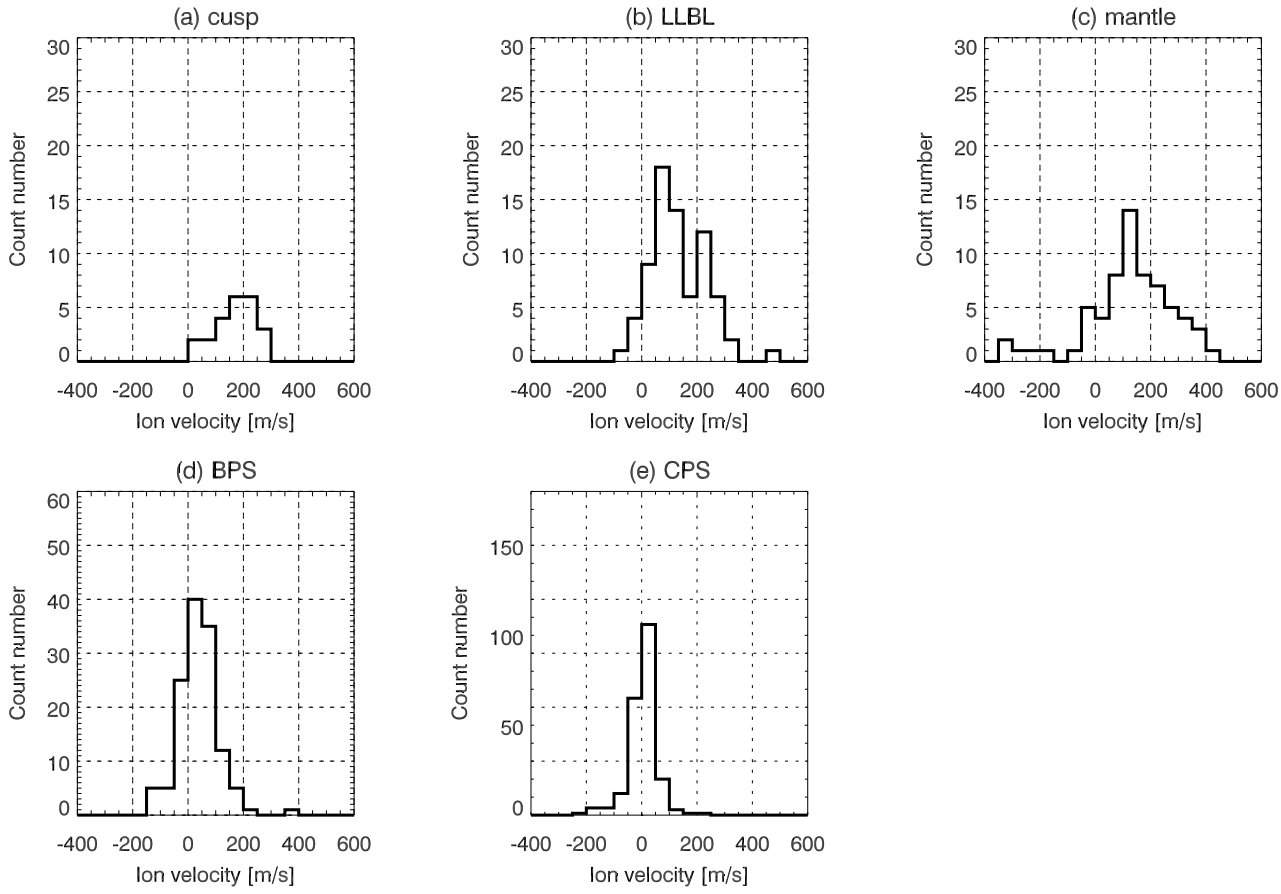

Figure 3.4: Ion velocity distributions at corresponding magnetospheric regions. Positive ion velocity is in an upward direction.

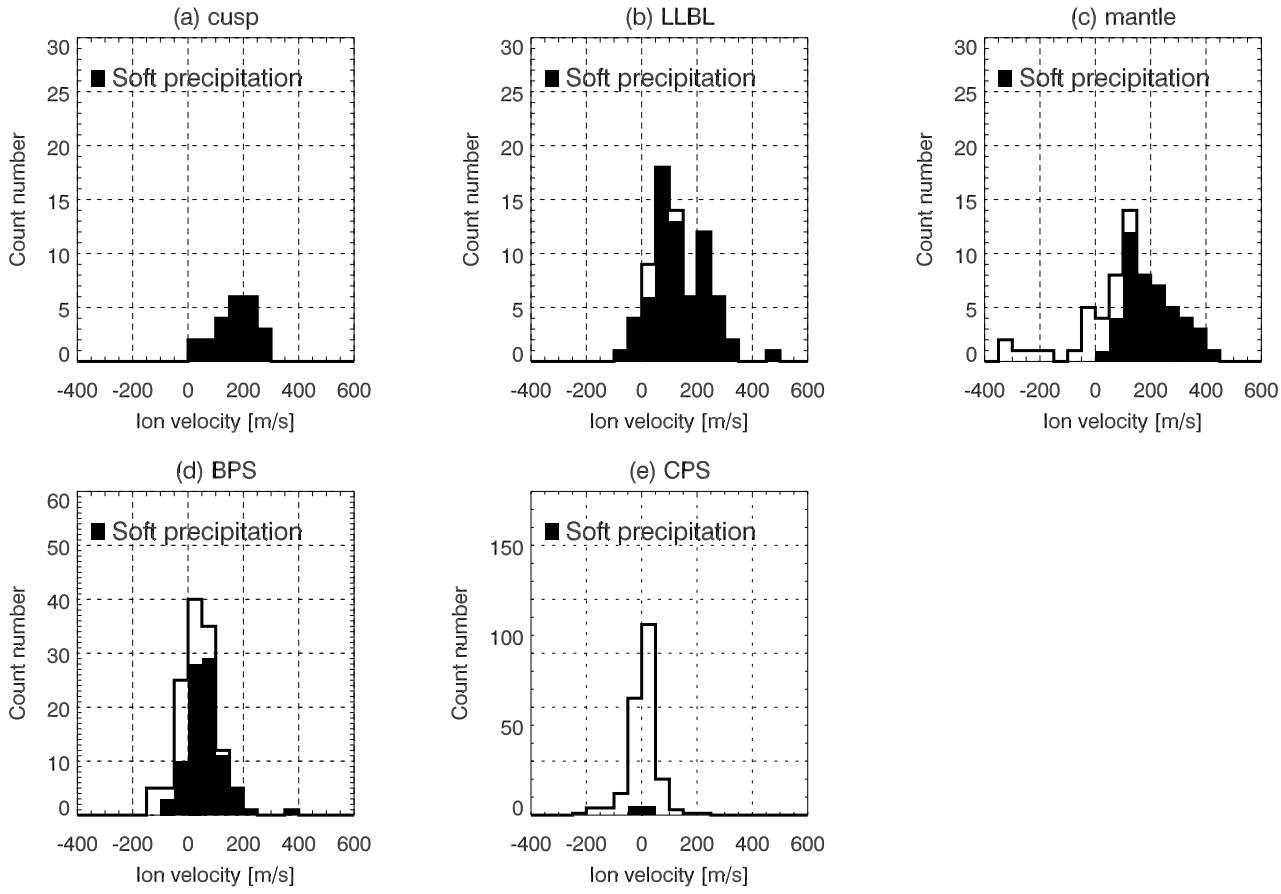

Figure 3.5: Ion velocity distributions at corresponding magnetospheric regions. Ion velocity distribution is shown in black when the differential energy flux of electrons at 100 eV is more than 10^7 eV cm^{-2} s^{-1} sr^{-1} eV^{-1}.

Chapter 4

Ion Temperature Anisotropy Associated With Ion Upflow

In this chapter, we investigate the relations between ion anisotropy and ion upflow by using the EISCAT Svalbard radar (ESR) and EISCAT VHF radar simultaneously. The simultaneous ESR and VHF radar observations provide us with an opportunity to investigate the ion upflows at higher latitudes and anisotropy at higher altitudes than previous observations did using the EISCAT VHF and UHF systems in Northern Scandinavia. Section 4.1 describes the experiment. Section 4.2 describes the data set. Section 4.3 describes the observational results. The causes of ion anisotropy and ion upflow in the dayside topside ionosphere are discussed in Section 4.4. This chapter is mostly a reproduction of *Ogawa et al.* [2000a].

4.1 Experiment

We have conducted a simultaneous incoherent scatter (IS) radar experiment (Special Programme SP-NI-IOF) using both the ESR in Longyearbyen and the EISCAT VHF radar in Tromsø. This combination lets us particularly focus on the temperature anisotropies. Figure 4.1 illustrates the design of the experiment. The ESR, located at 78.2˚ N and 16.0˚ E, points towards the magnetic field-aligned (FA) direction and measures the electron density n_e, the magnetic FA ion velocity $V_{i//}$, and ion and electron temperatures $T_{i//}$ and $T_{e//}$ at altitudes above 150 km with an altitude resolution of 36 km. Complementarily, the EISCAT VHF radar, located at 69.6˚ N and 19.2˚ E, is operated in the Common Programme 4 mode: Two split

beams looking at a low elevation angle of 30˚ into two directions to the north; one beam is directed due north and the other is steered 14.8˚ to the west of north. The former beam crosses point C in Figure 4.1 located approximately on the magnetic field line of Longyearbyen at an altitude of 665 km. The range resolution is 65 km. The inclination of the magnetic field line at Longyearbyen is 81.5˚. The aspect angle between the radar beam from Tromsø and the Longyearbyen magnetic field is approximately 59˚.

4.2 Data

It is known that IS radar signals sometimes show spectra which cannot be explained by normal IS theory [*Foster et al.*, 1988]. One is an artifact; a reflection from satellites. The other is considered to be a natural phenomenon, the so-called naturally enhanced ion-acoustic lines (NEIALs) [e.g., *Rietveld et al.*, 1991; *Collis et al.*, 1991; *Forme and Fontaine*, 1999]. Intense echoes, often with asymmetrical spectra, are a frequently observed feature of the latter one. Using these criteria, we carefully inspected all raw IS spectra pre-integrated over 10 s during the time period of the experiment, between 0700 and 1100 UT on July 6, 1998, and constructed a 1 min post-integrated dataset after excluding all the abnormal spectra from the dataset. The FA ion velocity, electron density, and electron/ion temperatures were then derived assuming that the ions are oxygen ions (O^+) with a molecular composition at the lowest altitudes. From the catalogue of the NEIAL events (a subset of the abnormal spectra), we have obtained their occurrence frequency, which will be compared with the occurrence of ion upflows.

4.3 Observations

Figure 4.2 shows the color-coded height-time profiles of 1 min integrated data obtained from the ESR between 0700 and 1100 UT on July 6, 1998. These include, from top to bottom, the electron density n_e, the FA ion velocity $V_{i//}$, and the electron and ion temperatures $T_{e//}$ and $T_{i//}$, respectively. Magnetic Local Time (MLT) ≈ UT + 3 hours ≈ Geographical Local Time (LT) + 2 hours.

In the top panel, the electron density (a) shows two kinds of enhancements. One is continuous in time from 0810 until 1010 UT, which increases ionization by the solar illumination. The other is more short-lived and is seen between 0700 and 0800 UT and after

1010 UT. These enhancements are due to particle precipitation in the dayside high latitude region. The precipitation apparently contained low energy particles, which ionized the neutral atmosphere in the *F* region. The FA ion velocity $V_{i//}$ (b) shows FA upflow events between 0700 and 0740 UT, at 0805 UT, and after 1010 UT. These FA upflow events are a cluster of short-lived (or a burst of) ion upflows. Each upflow starts at approximately 400 km in height. The velocity of the ion upflows tends to become faster with increasing altitude and occasionally reaches 500 m s^{-1} at 700 km. The electron temperature, shown in the third panel (c), also shows enhancements. Both the envelope and each segment of the enhancements very well coincide with those of FA upflows as well as with electron density increases. The FA ion temperature $T_{i//}$ (d) also increases during roughly the same time periods as the enhancements of both the FA upflows and electron density. There are, however, periods of poor correspondence between these two. For example, around 0720 UT there are FA ion upflows, but no significant $T_{i//}$ increases.

Figure 4.3 shows the color-coded height-time profiles of 20 sec integrated data obtained from the EISCAT VHF radar between 0718 and 1115 UT on July 6, 1998. They include, from top to bottom, the electron density n_e, the ion velocity $V_{i,VHF}$ toward the geographic north, and electron and ion temperatures $T_{e,VHF}$ and $T_{i,VHF}$, respectively. The higher altitude corresponds to the higher geographic latitude, because the VHF radar is pointed at a low elevation angle of 30˚ to the north. Hence the altitude of 700 km corresponds to the 78˚ geographic north, while the altitude of 300 km corresponds to the 74˚ geographic north.

In the top panel, the electron density (a) shows a continuous increasing due to the solar illumination during the time from 0810 until 1010 UT. More short-lived enhancements seen with the ESR are not clearly observed, which is due more to a longer VHF radar pulse length (900 μsec) in comparison to that of the ESR (360 μsec). The ion velocity $V_{i,VHF}$ (b) shows northward flow events (> 500 m s^{-1}) between 0730 and 0737 UT, at 0805 UT, at 1010 UT, and after 1030 UT. Southward flow (< -100 m s^{-1}) is also seen between 0718 and 0720 UT at around 700 km altitudes, which corresponds to the latitude located near the ESR. Northward flow regions after 1030 UT gradually extend to the low latitudes, up to the 75˚ geographic north. Around 0800 to 1000 UT, fluctuations of the northward ion velocity with the period of approximately 5 min are seen. The electron temperature $T_{e,VHF}$, shown in the third panel (c), also shows enhancements. The enhancements continue to the high altitude (high latitude) regions from the large northward flow regions. The ion temperature $T_{i,VHF}$ (d) also increases during roughly the same time periods as the electron temperature enhancement. The ion

temperature enhancements around 0735, 1014 and 1050 UT correspond to the large northward flow events and occur at the same time as the FA ion temperature $T_{i//}$ (in Figure 4.2d) enhancements. They are probably due to the result of the frictional heating process between ions and neutral particles. Other ion temperature enhancements are seen from the VHF radar observation above 500 km altitude around 0725 - 0730 and 1025 - 1030 UT. They neither correspond to the large northward flow events nor the FA ion temperature $T_{i//}$.

The dayside ionosphere around the cusp is directly and/or indirectly affected by the interplanetary magnetic field (IMF) and by the solar wind conditions. We hence show the solar wind and IMF conditions on July 6, 1998, related to the SP we conducted. Figure 4.4 shows the IMF conditions observed from the ACE satellite (a) and the WIND satellite (b). The ACE satellite was located close to the L1 point, approximately 232 Earth's radii upstream from the Earth on the Sun-Earth line, while WIND was located approximately 60 Earth's radii upstream from the Earth on July 6, 1998. Based on these locations and the observed solar wind flow speed, the expected delay times for the IMF observed by ACE and WIND to reach the Earth would have been approximately 45 min and 8 min, respectively. The IMF *Bz* observed WIND became negative between 0710 and 0755, and after 0905 UT. In these time periods except for a time period between 0905 and 1010 UT, enhancements of the electron temperature are seen from both the ESR and the VHF radar. The enhancements are due to the particle precipitation, which tends to become active in the dayside when IMF *Bz* is negative. The ACE and WIND IMF data hence provide a consistent explanation for the enhancements of the electron temperature observed with the ESR and the VHF radar. The solar wind conditions observed from the ACE and WIND satellites are shown in Figure 4.5. The solar wind velocity is roughly stable around 630 $\pm$ 30 km s^{-1}, but the ion density in the solar wind suddenly changes from approximately 4 to 12 cc^{-1} around 0550 UT by ACE and then around 0630 UT by WIND. Our SP observation from 0700 to 1100 UT is hence conducted after the solar wind shock.

Particle data from the DMSP F13 satellite shows a cusp signature near the ESR site around 0735 UT (see Figure 3.1a). The equatorward boundary of the cusp signature is seen at 75.1° N, and the equatorward boundary of soft electron precipitations is at approximately 74.4° N. This is consistent with the equatorward boundary of the electron temperature enhancements at the same time period 0735 UT observed with the EISCAT VHF radar. Hence the electron temperature enhancement seems to be caused by soft electron precipitations and heat flux from the magnetosphere in the vicinity of the cusp.

Figure 4.6 shows time variations of several physical parameters obtained from the ESR and the VHF radar at point C (in Figure 4.1), which is located approximately on the magnetic field line of Longyearbyen at an altitude of 665 km. In Figure 4.6a, ion upflows are seen at this altitude between 0710 and 0745 UT and after 1010 UT. The maximum velocities are 350 and 500 m s^{-1} during these two time periods, respectively.

Figure 4.6b shows the relative occurrence frequency of the naturally enhanced ion line (NEIAL) events that were excluded before post-integration and were not used for deriving $V_{i//}$, $T_{i//}$, $T_{e//}$, and n_e. The upflow events are strongly correlated with high occurrences of naturally enhanced ion line events.

Figure 4.6c compares the ion temperatures measured with the ESR and with the VHF radar. As mentioned before, the ESR observes the FA temperature $T_{i//}$, and the VHF radar the temperature $V_{i,VHF}$ at an aspect angle of approximately 59˚ from the magnetic field. The ion temperature is strikingly anisotropic when an ion upflow occurs, while otherwise both observed temperatures are approximately equal. Associated with the ion upflows around 0730 UT, $T_{i,VHF}$ shows significant enhancements reaching values up to 3000 K. This is approximately 800 K higher than the background ion temperature (2000 - 2200 K). $T_{i//}$, quite differently, is even decreased by a few 100 K compared to the temperature (1900 K) before and after. The anisotropy factor, $T_{i,VHF} / T_{i//}$, shown in Figure 4.6d, becomes larger (1.4 - 1.7) when ion upflows occurred, while it stayed around 1.1 when no clear ion upflows were observed.

Figure 4.6e shows $T_{e//}$ (open circles) and $T_{e,VHF}$ (solid circles) measured with the ESR and VHF radar, respectively. Both temperatures are strongly enhanced during the ion upflow events and reach more than 5500 K. There are no significant differences between $T_{e//}$ and $T_{e,VHF}$. This suggests that isotropic electron temperatures are associated with ion upflows.

Figure 4.6f displays the electric field strength derived from the VHF radar measurement. Here we assume that the two directional VHF radar beams were measuring the same electric field from different view angles. The electric field is expected to cause enhanced frictional heating in the *F* region. The correspondence between enhancements of upflows and the electric field strength is at best only partial.

So far, it is clear that ion upflows correlate closely with particle precipitation. In order to investigate relations between ion upflow and wave activity due to the particle precipitation in detail, we focus on ion velocities and NEIALs at the time periods around 0730 and 1036 UT when the effect of frictional heating due to enhancements of electric field is relatively small.

Figure 4.7 and Figure 4.8 show the relation between the FA ion velocity and the NEIALs using high time resolution (10 sec) data. Figure 4.7 indicates the relation between the FA ion velocity and the NEIALs at altitudes from 380 km to 665 km between 0700 and 0800 UT on July 6, 1998. Vertical lines indicate the occurrence time and altitude of the NEIALs. Note that plasma parameters such as ion velocity and plasma temperature cannot be obtained while the NEIALs are received. The received powers of the NEIALs denoted by the thickest lines are 1000 times stronger than those of normal IS echoes. The thickest NEIALs are found around 0722, 0730, and 0733 UT. FA ion velocities just after the thickest NEIALs are largely positive and reach 400 m s^{-1} above 600 km altitude, while FA ion velocity is less than 200 m s^{-1} in any altitude around 0718 UT before one of the thickest NEIALs around 0722 UT. The strongly upward ion velocities immediately decrease with time. The ion velocities at 630 and 665 km altitudes at 0725 UT decrease to nearly 0 m s^{-1}. These characteristics are clearly seen in Figure 4.8, which also shows the relation between ion velocity and the NEIALs, but from 1000 to 1100 UT. The thickest and relatively strong NEIALs are found around 1034, 1037, and 1044 UT. There are large velocity differences above 500 km between before and after the NEIALs at 1034 UT. The increased velocities immediately decrease with time around 1040 UT and 1045 UT, or gradually decrease with time after 1046 UT.

Let us, for the moment, consider other examples. Upward ion velocities (of more than 100 m s^{-1} above 600 km altitude) are also shown around 0703 and 0736 UT in Figure 4.7 and around 1012 and 1025 UT in Figure 4.8, when enhancements of the electric field and both parallel and perpendicular ion heating are seen. These ion upflows seem to be also affected by frictional heating, as described in the introduction. Since the frictional heating input is considered to be of secondary importance to ion upflow in this event, we are not concerned here with ion upflow at these time periods as mentioned before.

4.4 Discussion

The simultaneous ESR and EISCAT VHF radar experiment has shown that in addition to isotropic ($T_{e//} \approx T_{e,VHF}$) enhancements of the electron temperature, significant ion temperature anisotropy (increases of the ion temperature obliquely to the magnetic field line $T_{i,VHF}$ and small decreases of the FA ion temperature $T_{i//}$) are associated with FA ion upflows.

The anisotropic ion temperature could indicate the presence of toroidal or nearly toroidal ion velocity distribution functions. As one possibility, such distributions are produced by

charge exchange reactions between ions and neutrals, when their relative drift/the electric field is high (≥ 70 mV m^{-1}). These charge exchange reactions cause frictional heating which heat ions in both the parallel and perpendicular directions to the magnetic field. The perpendicular ion temperature enhancement is slightly (approximately 1.5 – 2.0 times) larger than the parallel ion temperature enhancement. The point of this frictional heating is that parallel ion temperature $T_{i//}$ also increases when ion anisotropy occurs. This mechanism hence cannot explain the anisotropy observed around 0730 UT in our experiment, because parallel ion temperature $T_{i//}$ does not increase around the same time period of 0730 UT.

Furthermore, the characteristic feature of IS spectra for non-Maxwellian ion distribution produced by the charge exchange reactions, a central peak, was observed with the EISCAT UHF radar by *Lockwood et al.* [1989] and *Winser et al.* [1989]. In our ESR/VHF experiment a central peak in the spectra did not occur and a bi-Maxwellian distribution seems to fit the data well. The EISCAT UHF measurements were at approximately 300 km where ion-neutral reactions play a crucial role in the ion kinetics below *F* peak [*Lee et al.*, 1998]. Our measurements are at 665 km, where ion-neutral reactions play a less important role for the ion kinetics. The sum of the observations indicates that here microphysical processes different from the charge exchange under high relative drifts cause the anisotropy.

The good correlation of upflow with enhancements of T_e and n_e suggests that it is caused by precipitation related processes rather than by high convection. The total energy of electron precipitation around the cusp (typically, $n_{e,beam} \approx 10^7$ m^{-3} and $k_B T_{e,beam} \approx 100$ eV) is approximately 1.6×10^{-11} J m^{-3}, which is roughly equal to the total kinetic energy of ion upflow around 350 km (typically, $n_e \approx 10^{11}$ m^{-3} and $V_{i//} \approx 100$ m s^{-1}). As already mentioned in Chapter 3, in this kind of scenario previous models have identified enhanced ambipolar diffusion and heat flux as the main drivers of upflow. Our new data suggest that wave activity, which is probably also caused by precipitation, plays an additional role. The waves seem to heat ions at the energy of approximately 0.3 eV transversely up to a ratio $T_{i\perp}/T_{i//} \approx 2$. In-situ measurements have shown that the ion temperature remains isotropic below approximately 0.4 eV in quiet time (non-auroral) regions [*Norqvist et al.*, 1998]. This partial inconsistency might be explained by the lower altitude, perhaps also by the rather different instrumentation.

Using our data, we have calculated the resulting hydrodynamic mirror force [*Suvanto et al.*, 1989]. It accelerates the plasma upward, but is smaller by a factor of roughly five times in comparison to the FA ion and electron pressure gradients, which were also calculated from the data (see Appendix A). Therefore it remains unclear whether there is some additional, still

unknown, FA bulk ion acceleration mechanism due to the wave activity. For example, lower hybrid waves, generated in the events of electron precipitation, could effectively accelerate electrons and ions [*Lynch et al.*, 1994]. Furthermore, the upward parallel electric field due to anomalous resistively produced by plasma turbulence also has a possibility to drive ion upflow ([*Wahlund et al.*, 1992a] and see Appendix A).

The FA ion velocities immediately change around strong NEIALs, which may be caused by plasma instabilities. Although we cannot obtain the FA ion velocities from IS signals while the NEIALs are received, ions are also accelerated upward while the NEIALs are received [*Forme and Fontaine*, 1999]. Thus generation mechanisms of ion upflow must have transversely ion heating and upward acceleration by wave-particle interaction.

We hence finally suggest that the combined effects of the wave-induced accelerations and of precipitation enhanced ambipolar diffusion and heat conduction are predominant drivers of ion upflow in the topside ionosphere. The mirror force effect associated with transversely ion heating becomes more important as altitude increases. Our suggestion could be checked by combining and extending existing hydrodynamic and kinetic models.

4.5 Chapter Summary

Plasma heating associated with ion upflow in the dayside *F* region/topside ionosphere has been presented using data obtained simultaneously with the ESR and the EISCAT VHF radar on July 6, 1998. The results obtained are summarized below.

1. Our observation is the first experiment using two IS radars for targeting plasma temperature anisotropies at the topside ionosphere where field-aligned (FA) ion upflow occurs. Plasma temperature obtained along the magnetic field line and nearly perpendicular to the magnetic field have sufficient quality with a time-resolution of 5 min and can be used to investigate plasma temperature anisotropies continuously.

2. The FA ion upflows observed at an altitude of 665 km in the dayside cusp are associated with significant anisotropy of ion temperature, isotropic increases of electron temperature and enhancements of electron density. The anisotropy factor, $T_{i,VHF} / T_{i//}$, reaches maximum values of 1.7. There is no clear correspondence between the enhancements of the electric field strength and the occurrence of the ion upflows. This suggests that the ion

upflow is driven primarily by precipitation.

3. The energy of soft particle precipitation is supplied to the ions in the *F* region/topside ionosphere via wave-particle interaction, such as wave-induced transverse ion heating, and upward parallel electric field due to anomalous resistively produced by plasma turbulence. The data support that in addition to direct precipitation effects, namely enhanced ambipolar diffusion and heat flux, the wave-particle interaction may play an important role in ion upflow in the F region/topside ionosphere.

4. The FA ion velocities immediately changed around strong NEIALs. This implies that plasma waves associated with the NEIALs play a significant role in heating ions transversely and driving FA bulk ion upflows. In order to specify plasma waves associated with ion upflow, the characteristics of NEIALs, particularly the dependence of the wave number *k*, are investigated in the next chapter.

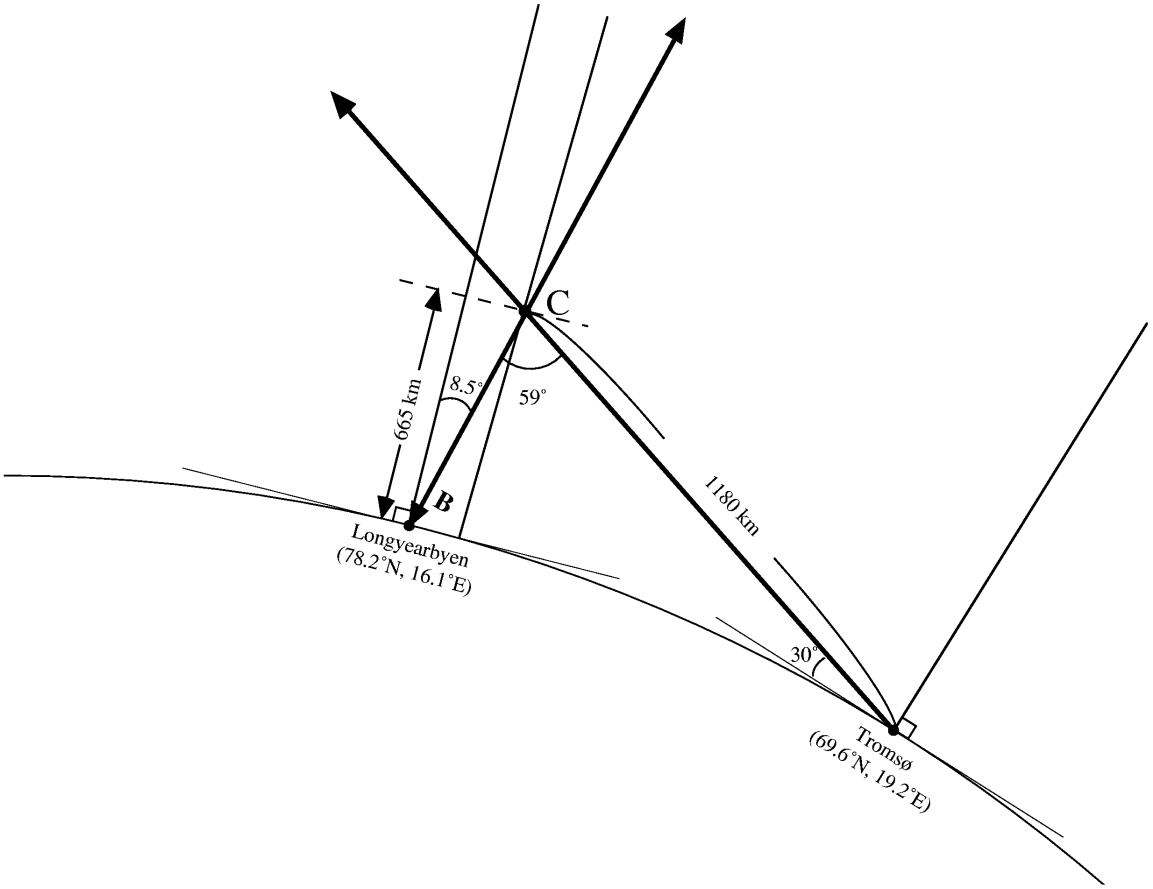

Figure 4.1: Sketch of the geometry and antenna pointing during the EISCAT special programme used for this study. The ESR is pointed in the magnetic field-aligned (FA) direction. The EISCAT VHF radar is simultaneously pointed at a low elevation angle of 30° into two directions far to the north. One of the beams crossed a point C located approximately on the magnetic field line of Longyearbyen at the altitude of 665 km.

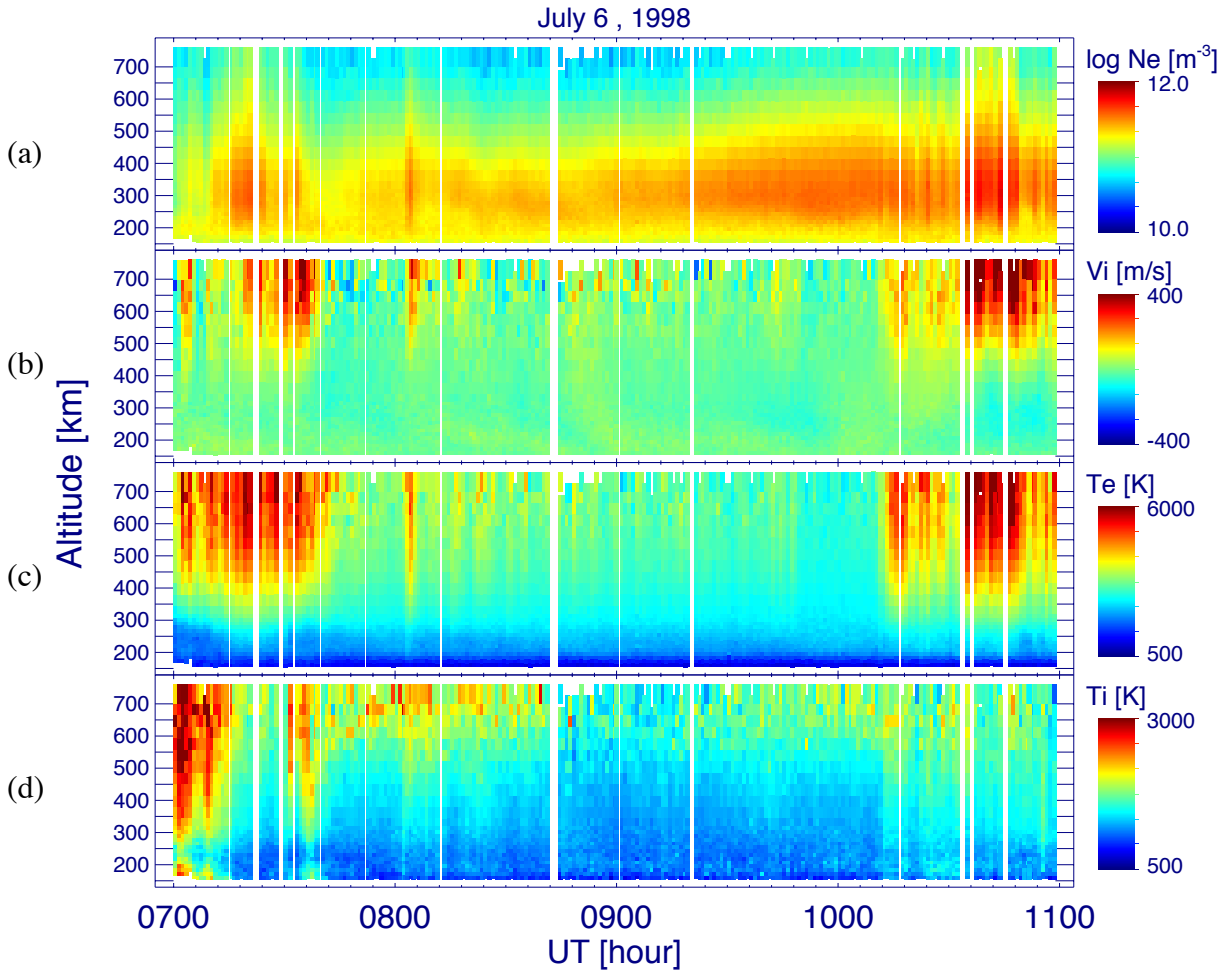

Figure 4.2: Color-coded height-time profiles of 1 min integrated data obtained from the ESR between 0700 and 1100 UT on July 6, 1998. They are, from top to bottom, the electron density n_e, the magnetic field-aligned (FA) ion velocity $V_{i//}$, and electron and ion temperatures $T_{e//}$ and $T_{i//}$.

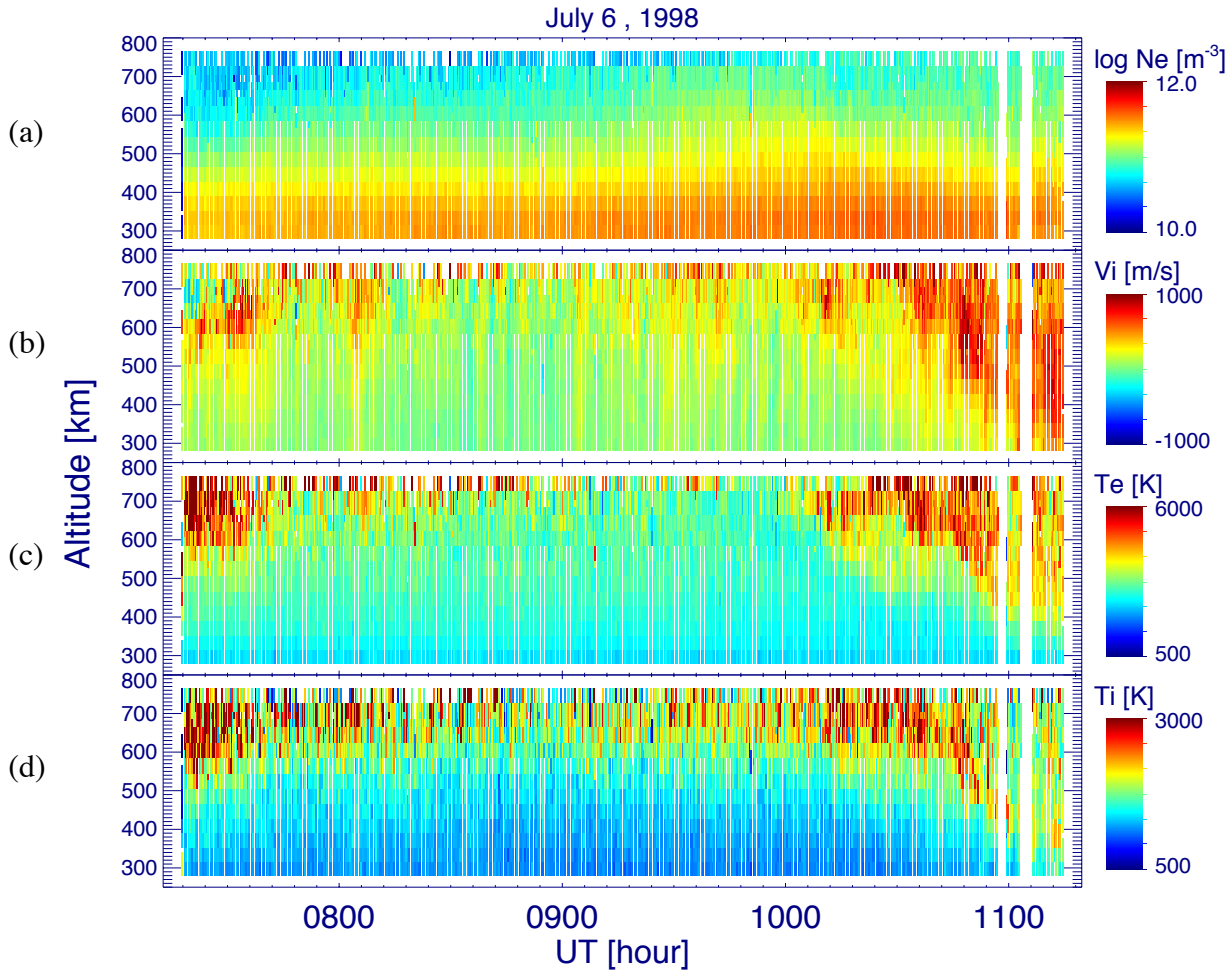

Figure 4.3: Color-coded height-time profiles of 20 sec integrated data obtained from the EISCAT VHF radar (directed to the geographic north) between 0718 and 1115 UT on July 6, 1998. They are, from top to bottom, the electron density n_e, the ion velocity $V_{i,VHF}$, and electron and ion temperatures $T_{e,VHF}$ and $T_{i,VHF}$.

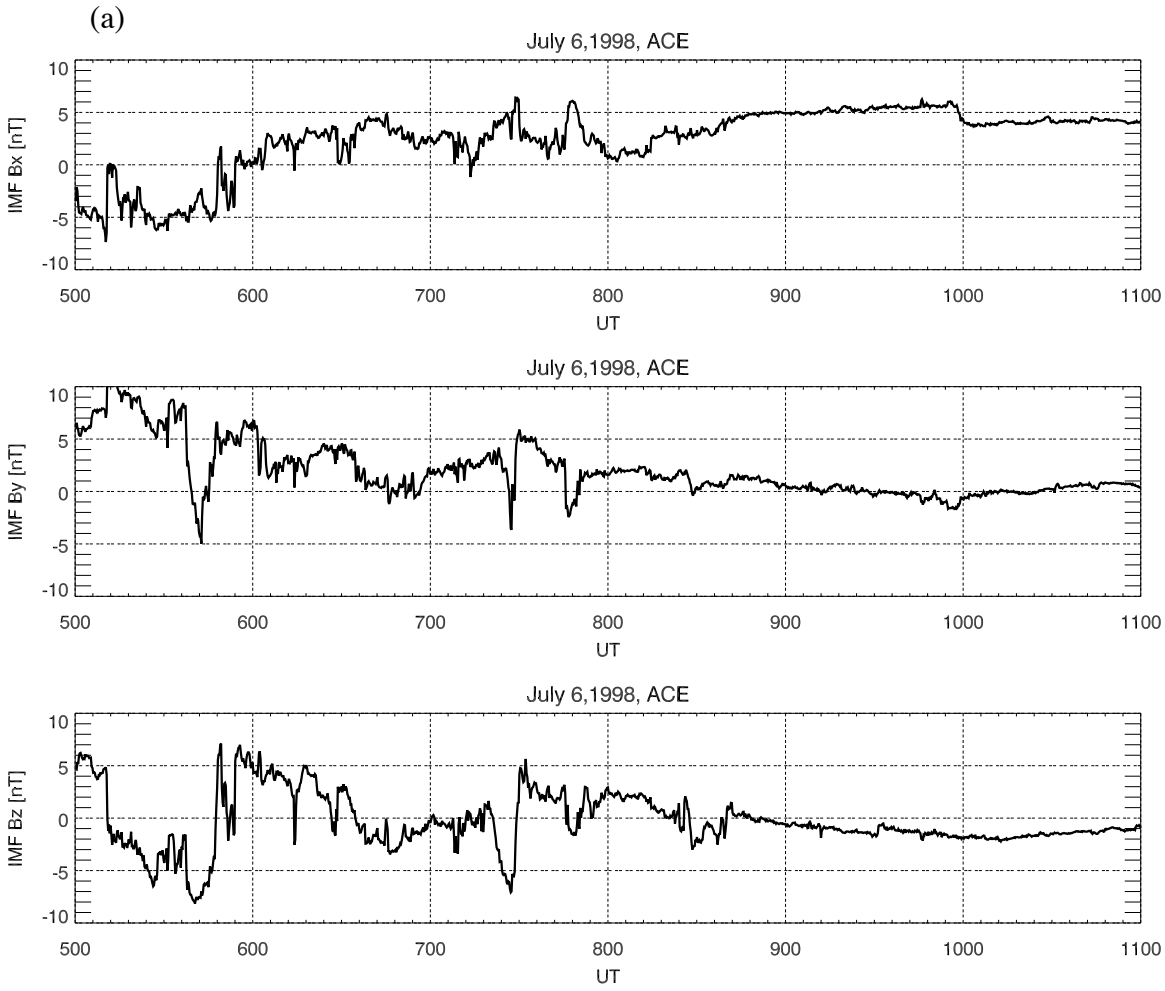

Figure 4.4: (a) Components of the Interplanetary Magnetic Field (IMF) in GSM coordinates on July 6 1998, as measured with the ACE satellite near the L1 point. (b) The format is the same as (a), but showing the IMF components measured with the WIND satellite near the Earth.

(b)

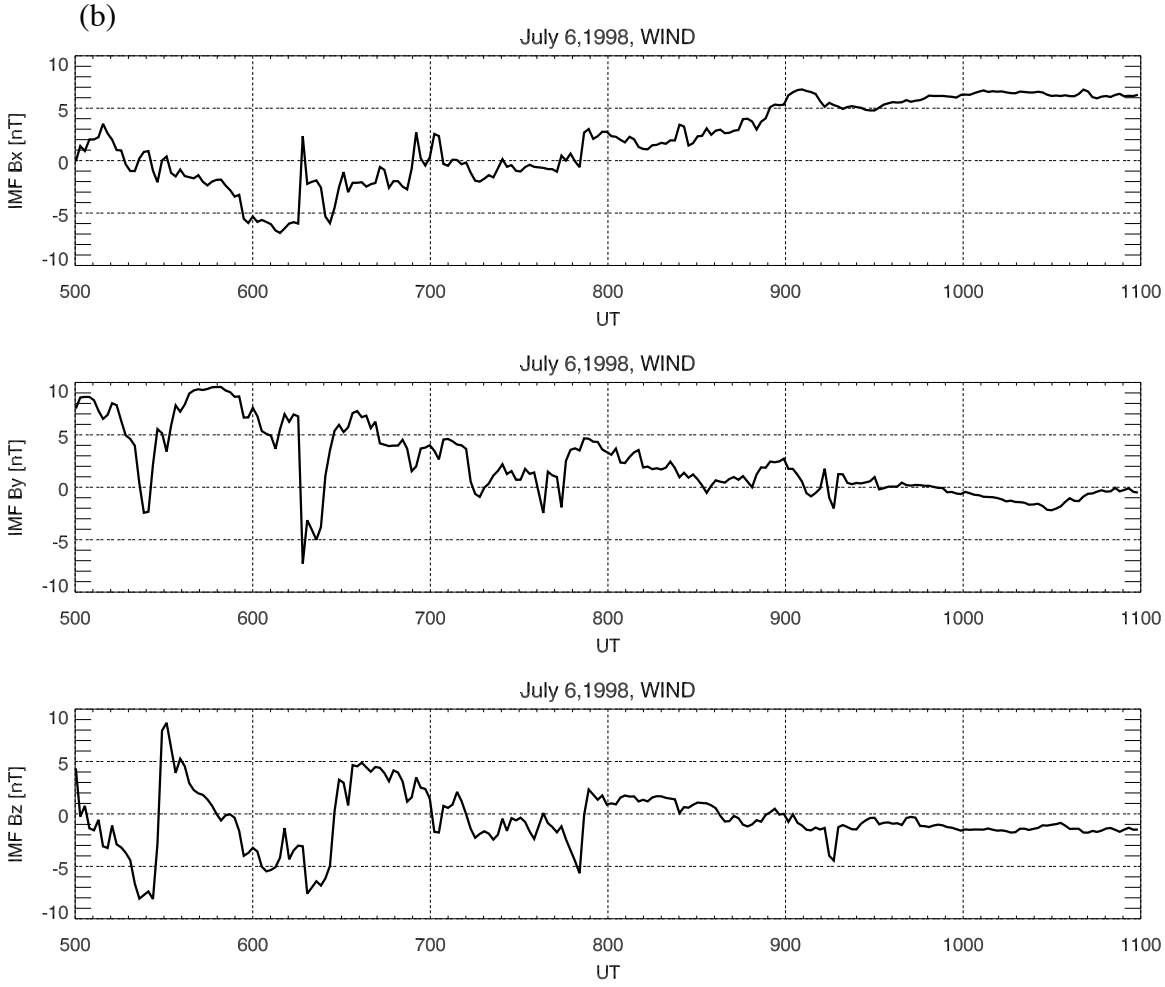

Figure 4.4: (continued)

(a)

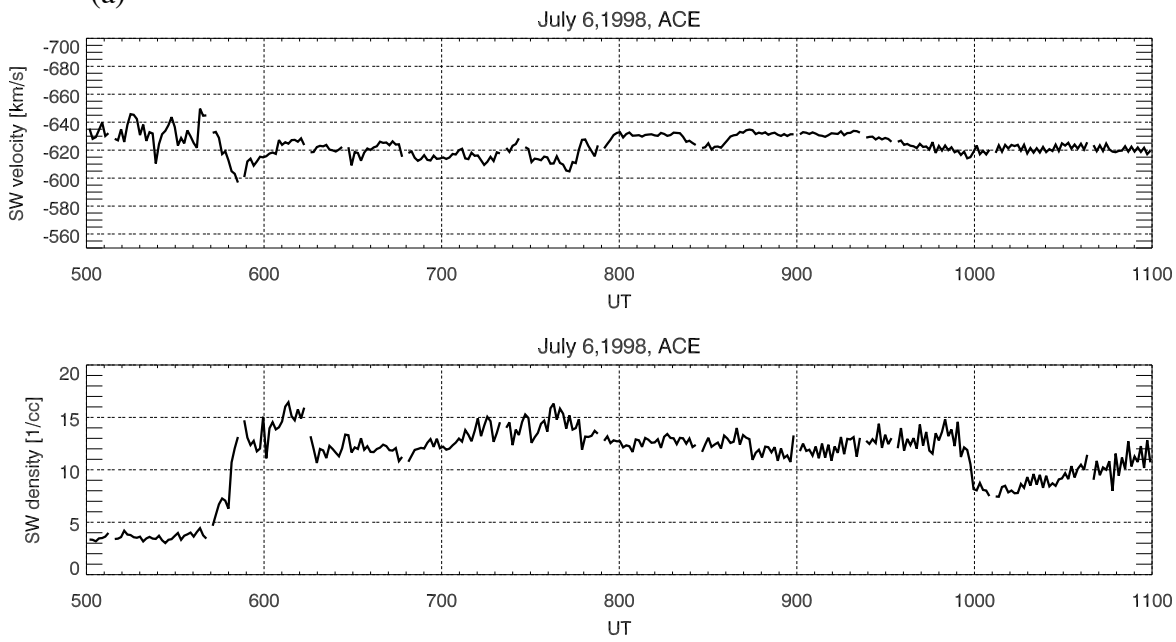

Figure 4.5: (a) Components of the ion density and velocity in the solar wind in GSM coordinates on July 6 1998, as measured with the ACE satellite near the L1 point.
(b) The format is the same as (a), but measured with the WIND satellite near the Earth.

(b)

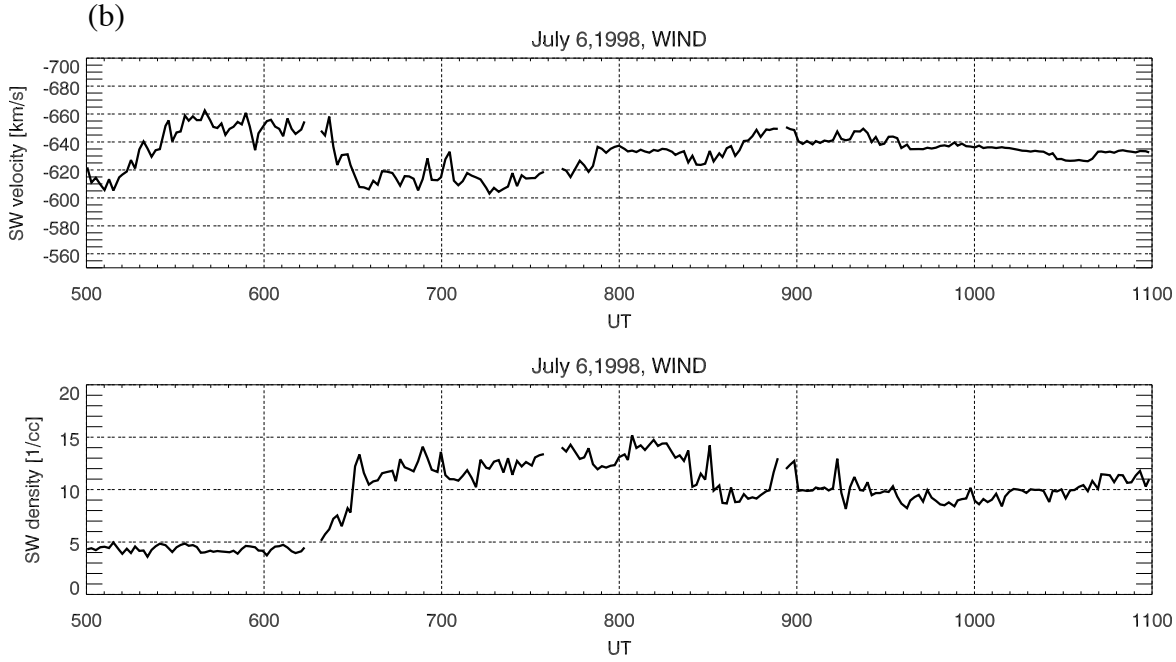

Figure 4.5: (continued)

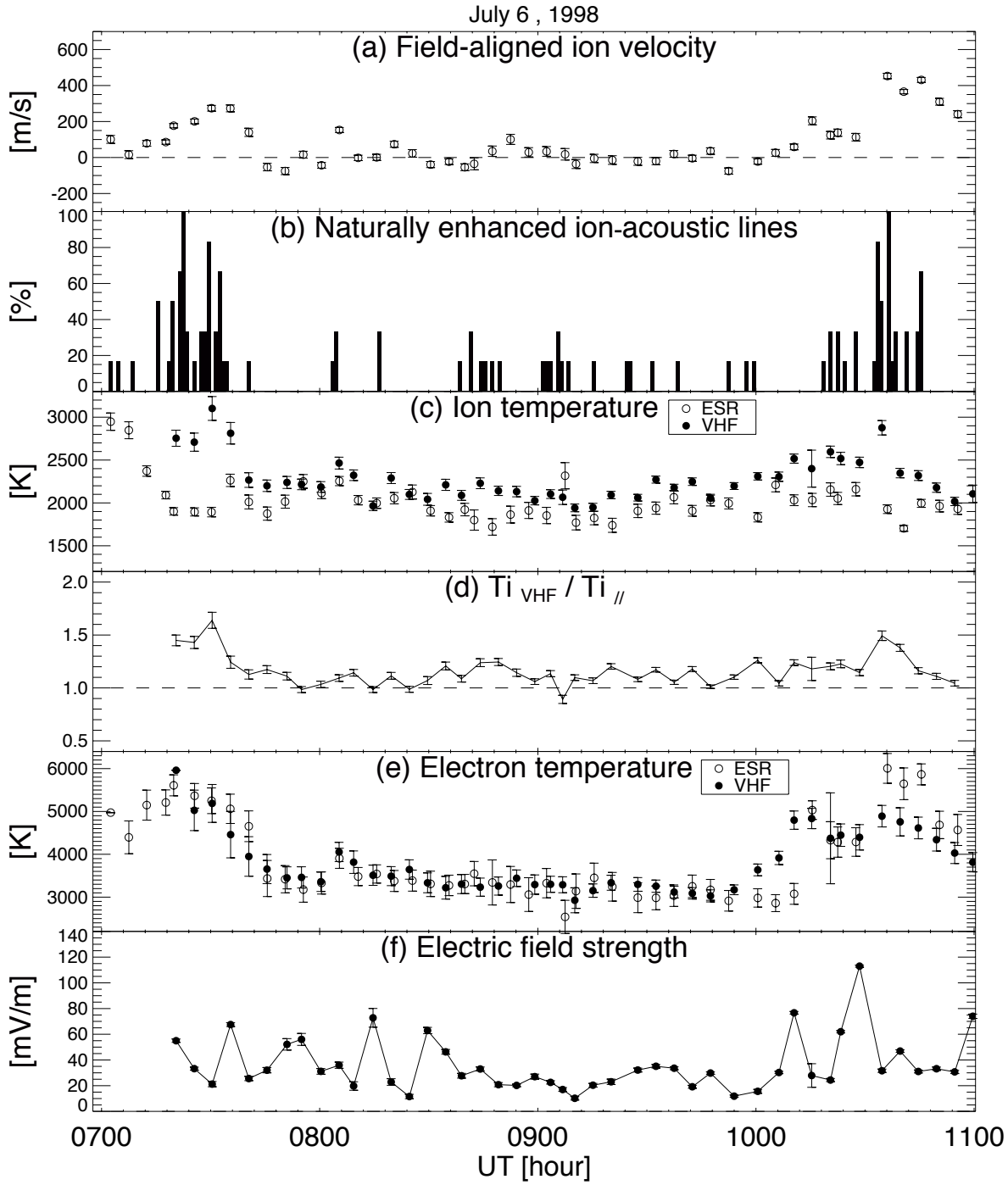

Figure 4.6: Time variations of several physical parameters obtained from the ESR and the EISCAT VHF radar at an altitude of 665 km (point C in Figure 4.1) along the Longyearbyen magnetic field line. The parameters shown are (a) $V_{i//}$; (b) the relative occurrence frequency of the naturally enhanced ion-acoustic line; (c) $T_{i//}$ and $T_{i,VHF}$, measured with the ESR (open circles) and with the EISCAT VHF radar (solid circles); (d) the ion temperature anisotropy $T_{i,VHF}$ / $T_{i//}$; (e) $T_{e//}$ (open circles) and $T_{e,VHF}$ (solid circles); (f) the electric field strength derived from the VHF radar measurement.

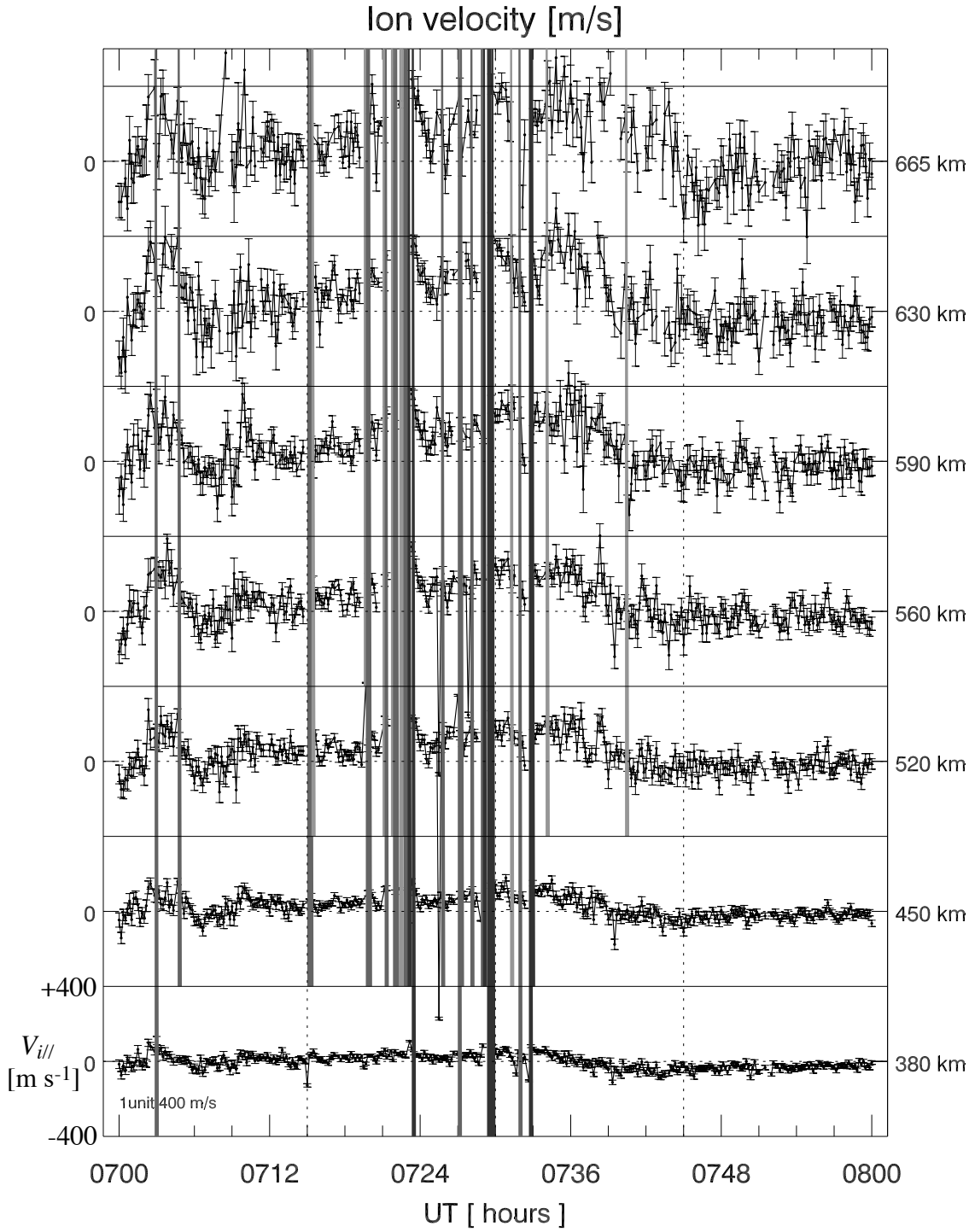

Figure 4.7: Relation of the magnetic field-aligned (FA) ion velocity $V_{i//}$ to naturally enhanced ion-acoustic lines (NEIALs) at altitudes from 380 to 665 km between 0700 and 0800 UT on July 6, 1998. Received powers denoted by thickest lines are 1000 times stronger than those of normal incoherent scatter (IS) signals.

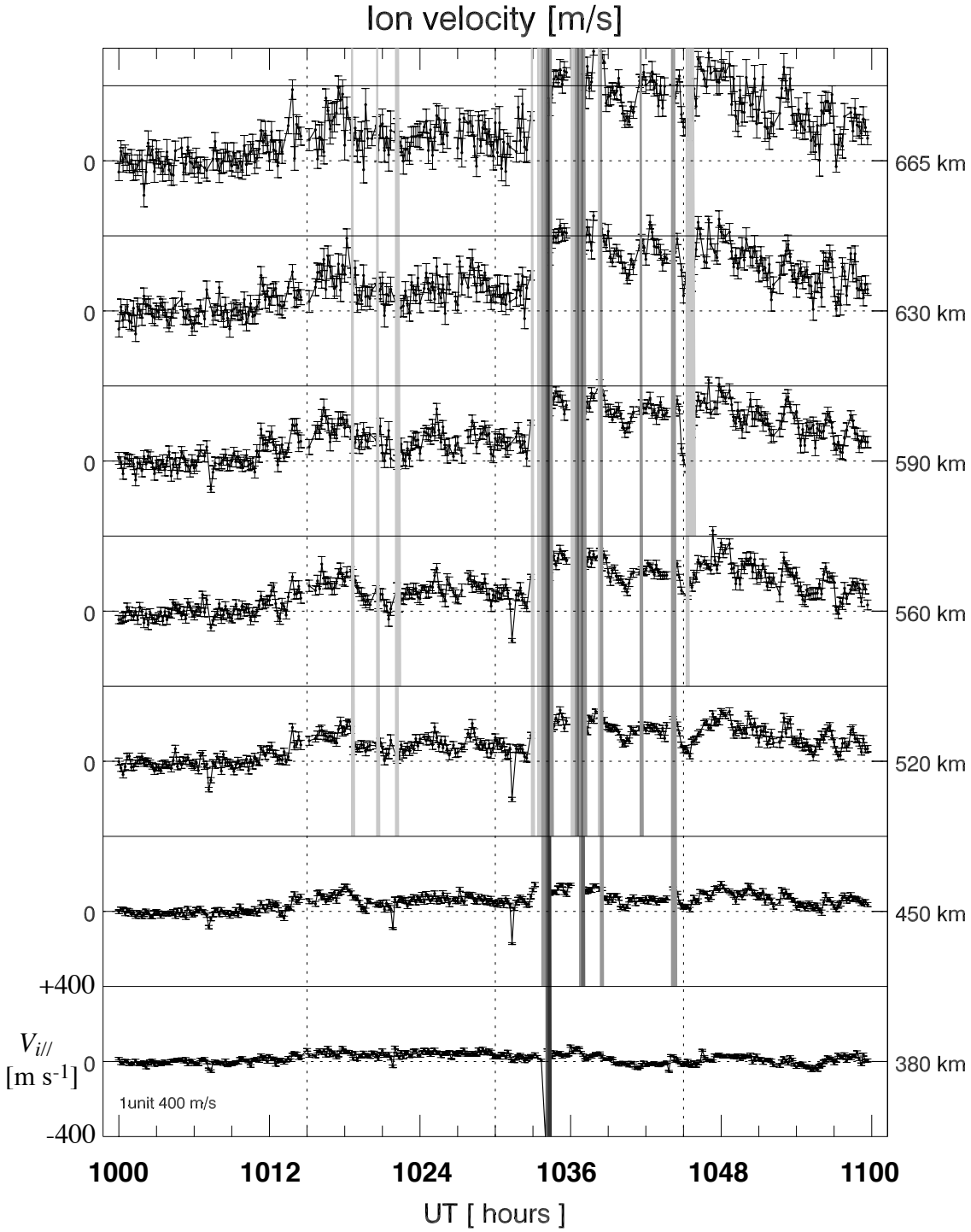

Figure 4.8: Relation of the magnetic field-aligned (FA) ion velocity $V_{i//}$ to naturally enhanced ion-acoustic lines (NEIALs) at altitudes from 380 to 665 km between 1000 and 1100 UT on July 6, 1998. Received powers denoted by thickest lines are 1000 times stronger than those of normal incoherent scatter (IS) signals.

Chapter 5

k-Dependence of the Naturally Enhanced Ion-Acoustic Lines

In this chapter, the focus is on the phenomena driven by plasma instabilities, in particular on the wave number (*k*)-dependence of the naturally enhanced ion-acoustic lines (NEIALs). In order to specify the causes of the NEIALs, it is important to statistically examine the existence of the *k*-dependence of the NEIALs. In this study we use a database of NEIAL events obtained from 0700 to 0800 UT on July 6, 1998 and compare their power characteristics with those of real satellite echoes. Section 5.1 describes the reason for this in more detail. Section 5.2 describes the analysis methods which use data recorded separately from different receiver channels of the EISCAT Svalbard radar (ESR). Section 5.3 and 5.4 describe the observational results of NEIALs and of real satellite echoes, respectively. The *k*-dependence of NEIALs is discussed in Section 5.5. This chapter is mostly a reproduction of *Ogawa et al.* [2000b].

5.1 Purpose

Figure 5.1 shows power profiles of incoherent scatter signals from the GUP0 program obtained from the ESR at 0724:10 UT on July 6, 1998. In the left panels the thick line indicates data from channel 1 using the lowest frequency of the ESR, and the thin line indicates data from channel 6 using the highest frequency of the ESR. In the case of normal incoherent signals (upper left panel), there seems to be no significant difference between the

powers from both channels. The right panels show the normalized power difference between the powers from either of the channels. This normalized difference increases with range, because the signal-to-noise ratio (SNR) decreases with range; thus the statistical fluctuations increase, for low SNR statistical power differences between the two channels are relatively large and randomly fluctuate. This is expected because the GUP0 receiver settings produce only small correlations between subsequent samples for a noise-dominated input. For high SNR the power differences are small and seem somewhat correlated, which is also expected for an IS signal with a poor range resolution of 54 km.

On the other hand, in the lower left panel (at 0723:20 UT), NEIALs enhance the power in the range between 400 and 800 km. In the case of the NEIALs, the received power from both channels is relatively high, causing a high SNR. Note that the power scale (x axis) in the lower panel is 10 times larger than that in the upper panel. Normal IS signals are seen around the *F* peak, and the normalized power difference from the two channels (right panel) is within statistical fluctuations. However, around the power peak (500 km), the powers from both channels seem to differ more than we expected, taking into account that the SNR is very high compared to the upper panel. For such a high SNR we expect rather small relative power differences, smaller than in the same profile at around 300 km. At the largest ranges around 850 km there is still significant power in the noise-subtracted profile with NEIALs (lower panel in Figure 5.1). We have observed that this is a typical feature of profiles with NEIALs, and it is absent in profiles with only IS signals. The NEIALs seem to produce a distinct power peak but also to extend over a wider range consistent with earlier studies [*Rietveld et al.*, 1991]. They are rather soft radar targets filling the volume illuminated by the radar pulses as opposed to real satellites which are hard targets. If the power differences of a soft target are fluctuating uncorrelated along the profile, the differences should cancel each other out when long pulses (54 km in this experiment) are used, although some correlation between samples arises from the uneven power level along the illuminated volume, which is similar to the situation in the upper panel for the IS signals. However the relatively smooth variation and the large power difference as seen in Figure 5.1 between approximately 400 and 700 km cause us to suspect that NEIALs not only exhibit larger power differences than expected, but that the differences seem to be systematic along the altitude.

In the following we investigate whether these power differences are related to the occurrence of a high SNR or perhaps an inherent feature of NEIALs. Furthermore, we assess how often these frequency dependences occur.

5.2 Methods

The relatively low peak but high average power (25% duty cycle) of the ESR transmitter can be utilized efficiently only through a systematic use of multi-frequency modulations [*Wannberg et al*., 1997]. Among the basic radar codes constructed for the ESR, GUP0 is the most suitable to compare power differences between channels. The GUP0 is a multi-frequency long-pulse code, and mainly intend for *F* region and topside observations.

Table 5.1 shows a summary of the GUP0. The maximum frequency difference between 8 channels around 500 MHz is 2 MHz. In this study, we used channels 1, 2, 3, 5, 6, and 7, because they receive pulses of equal length (360 μsec) with a range resolution of 54 km. The other two channels use a pulse length of 150 μsec. For our investigation, we have used data obtained between 0700 and 0800 UT on July 6, 1998, because in this period a number of the NEIALs samples were seen (see Figure 4.6 and 4.7 in Chapter 4). The antenna was set along the field-aligned (FA) direction in this experiment. In a sophisticated radar like the ESR the signals pass through numerous stages. It is difficult to calculate the expected relative gain from two different channels. Therefore we use the data themselves to calibrate and assume the following relation between channels:

$$Power_n = g_n \cdot Power_1 \,, \tag{5.1}$$

$$g_n(t) = \left\langle \frac{background_n(t)}{background_1(t)} \right\rangle_r \,, \tag{5.2}$$

where n indicates the channel number, and g_n is an estimate of the relative gain during one pre-integration period which may depend on time t. The subscript r indicates that averaging is made over a pre-integrated power profile using the SNR to weight the data.

The five panels in Figure 5.2 show the relative gains $g_n(t)$ from 0700 to 0800 UT on July 6, 2000. g_n seems to depend only weakly on time. The histograms in Figure 5.3 show the distributions of the relative gains. All distributions are consistent with the assumption that the relative gains have simply statistical fluctuations. We use the average of each distribution to compare the measured power at different channels/frequencies.

5.3 Results

In Figure 5.4, five scatter plots show the relative power differences over SNR. The thin points are from normal IS signals, and the thick ones at the high SNR are from ranges with power enhancements from NEIALs. NEIALs were always seen on all channels. Assuming a Gaussian distribution of both the noise and the scatter signal, data should scatter approximately according to the relation

$$\frac{\Delta power}{power_1} = \frac{1}{\sqrt{N(IPP)}} \cdot \left(1 + \frac{1}{SNR}\right), \tag{5.3}$$

N(IPP) is the number of samples. One effective interpulse period (IPP) lasts 13.4 msec. The auto-correlated data are integrated over 744 IPPs or 10 sec. We have also estimated the standard deviation of the relative differences in 8 SNR bins and found empirically that the relation (5.3) represents reasonably well the actual standard deviation. Most data points, in particular at SNR < 3, scatter not more than expected from normal distributions with standard deviation given by the curve in Figure 5.4. Enhanced (thick) data points connected by a line originate from the same profile (pre-integration period). It can be seen that the data points with large power differences come from the same profiles. In other words, where a power difference is larger than statistically expected, it also tends to vary systematically with an altitude over one post-integration period. If all the enhanced powers of NEIALs were produced in a narrow layer, similarly as for a hard target, the long pulse length combined with the receiver filter would lead to horizontally rather than vertically connected data points as will be shown in the next section for real satellite data. It should be noted that our NEIALs sometimes last 30 sec and longer, consistent with previous EISCAT UHF observations [*Rietveld et al.*, 1991]. NEIALs typically seem to come and go over seconds or tens of seconds. If they were made of conglomerations of very short-lived (< 1 sec) bursts, each one producing a much higher SNR than the observed, average SNR, a random frequency dependency of the cross section should tend to cancel when integrating over 10 sec.

In order to obtain a statistically meaningful quantity for the difference between NEIAL and normal IS data, we have mapped all data points in Figure 5.4 to a reference SNR of 1 using equation (5.3). Thus two distributions of power differences are created, one for normal IS signals and one for NEIALs. They are shown in Figure 5.5. These distributions are not

composed of completely independent points because the long pulse length causes correlations along a profile as discussed qualitatively in section 5.1. We have assumed that only every 18th point is independent, which is pessimistic, since data points are obviously not correlated over a complete pulse length. Using the test described by *Press et al*. [1992] there is 5% or lower probability that both distributions in Figure 5.5 are the same or that NEIALs statistically do not have larger power differences than IS signals. Next we investigate the relative power in real satellites which also cause high, often even higher SNR than NEIALs.

5.4 Comparison with Echoes From Satellites

In order to explain the spectral difference between normal echoes, NEIALs, and echoes from real satellites, their IS spectra are shown in Figure 5.6, 5.7, and 5.8, respectively. Formats of these figures are the same as those in *Rietveld et al.* [1991] (see also in Figure 1.7 in this thesis), *Sedgemore-Schulthess et al.* [1999], and *Forme et al.* [2001]. The right (left) ion line indicates downgoing (upgoing) ion-acoustic waves. In the following we use the terms "upshifted" and "downshifted" to refer to downgoing and upgoing ion-acoustic waves, respectively. The black lines in these panels follow the positions of each ion-acoustic peak. Figure 5.6 shows the normal IS spectra measured with the ESR at 0724:10 UT. Usually double humped peaks are seen in the IS spectra, and the spectral intensities decrease with increasing altitude above the *F* peak. Spectra including NEIALs shown in Figure 5.7 have strong peaks around 470 km altitudes. The spectral intensities are more than 10 times larger than those in normal IS echoes. Both downshifted and upshifted ion-acoustic lines have enhancement, but the downshifted ion-acoustic line is more intense than the upshifted one. The spectral signatures resemble those exhibited for the EISCAT UHF radar in Figure 1.7. Figure 5.8 shows IS spectra including echo from a real satellite. The enhanced spectral peak is seen in narrower ranges than NEIALs. However, it may be difficult to distinguish between echoes from satellites and NEIALs by using only spectral signatures, because the enhanced spectral peak is shifted, by the flight speed of the satellite, into 4 kHz, which is near the ion-acoustic frequency.

Figure 5.9 shows the same example of echoes from a real satellite, and the power profiles and power difference between the two channels. The satellite return is seen over a range of 54 km, which is the same as the pulse length. The received power level around 600 km altitude is almost the same as NEIALs, but the power difference between the two channels is nearly

constant. The feature is clearly seen in the right panel (b). The normalized power difference increases with increasing altitude, but the power difference from a real satellite is steady at approximately -0.18 at altitudes between 570 and 620 km. We hence used not only spectral signatures but also power profiles in order to distinguish between the NEIALs and echoes from real satellites.

We found two real satellites in the data period, and used them for the NEIAL study. Figure 5.10 shows the relative power differences between channels for real satellites in the same format as Figure 5.4. The power differences follow approximately a horizontal line for each profile containing a satellite echo mainly due to the small correlations induced by the digital ESR receiver filters. Most satellite echoes are in the right tips of the approximate horizontal lines. This means that the power difference is constant over an integration period, even if the SNR becomes very high. This is obviously different from the behavior for NEIALs. We thus conclude that the relative gains in the receiver do not vary systematically over a pulse cycle within a few interpulse periods, but is rather constant over such short time scales (13.4 msec). The relative power in real satellites, although constant over a pre-integrated profile, varies from event to event by a large factor, much more than expected as can be seen in Figure 5.2. In GUP0 the pulses from channels 1, 2, and 3 are transmitted in one IPP, and from channels 5, 6, and 7 they are transmitted in the next IPP (see Figure 2.2a). A satellite may enter or leave the radar beam rapidly within 100 msec or so between pulses from different channels, which explains large power difference between channel 1 and 5, 6, and 7, respectively. This, however, leaves a large unexpected and unexplained difference between the two events when comparing channels 1 and 2 with in time adjacent transmitter pulses as shown in the upper left panel of Figure 5.10.

5.5 Discussion

We have studied the relative powers between channels using different frequencies in high SNR situations. In the case of NEIALs, we found that variations of the relative power between channels well above both the estimated and expected 1-sigma level occur over signal pre-integrated profiles, and a few profiles within 1 hour of data where the power radiated by NEIALs varies systematically with wavelength/wave number (k). This feature of NEIALs does not seem to be caused by the ESR system. Furthermore, power differences along one profile with NEIALs are obviously different from those of echoes from satellites at a similarly

high SNR. Therefore the NEIAL cross-section itself seems to vary strongly with frequency. If the NEIAL power is highly frequency dependent, why are the differences usually in the noise level? It may be due to the very small frequency spacing. The relative frequency difference is approximately 0.3%. We believe that the study of a *k*-dependence of the NEIALs will require a large statistical database and dedicated experimental modes using a wider frequency spacing between channels.

In addition to this *k*-dependence, the amplitude enhancement of upgoing and downgoing ion-acoustic waves occurs at somewhat different power levels and different altitudes (also see Figure 1 in *Forme et al*. [2001]). These observational facts are modeled using the parametric decay of beam driven Langmuir waves in an inhomogeneous medium [*Forme et al*., 2001]. It is shown that the density gradient with altitude as well as the collisions contribute to an altitude variation of ion-acoustic spectra and may account for the observed signatures. It is also responsible for the transition from upshifted to downshifted enhanced ion lines. The model shows that the power radiated by enhanced spectra varies with the wavelength and that the power difference between two wavelengths varies with altitude.

Lower hybrid (LH) waves as well as ion-acoustic waves are theoretically considered as signatures of the low frequency modulation of Langmuir waves. The evidence for interactions of Langmuir waves with LH waves are found with the Freja satellite around 1500 km [*Stasiewicz et al*., 1996]. While Freja observations from approximately 1700 km and models show the lower hybrid waves heat ions transversely above approximately 40 eV [*André et al*., 1994], observations by sounding rockets at up to approximately 1000 km show a good correlation between waves above lower hybrid waves and transverse ion energization to characteristic energies of up to approximately 10 eV [*Kintner et al*., 1992; *Chang*, 1993; *Singh*, 1994; *Lynch et al*., 1996]. Although it is still unknown how plasma waves heat thermal ions (< 0.4 eV) transversely, it seems reasonable to suppose that the heating effects by plasma waves, which may be related to parametric decay instabilities of Langmuir waves driven by precipitating soft energy electron beams, play an important role in ion upflow in the topside ionosphere. The heating is considered to occur in the vicinity of the cusp, according to the investigation discussed in Chapter 3 and 4.

5.6 Chapter Summary

The *k*-dependence of the received power in high signal-to-noise ratio (SNR) conditions,

occurring for naturally enhanced ion-acoustic lines (NEIALs) and for real satellites, has been investigated by using the EISCAT Svalbard radar (ESR), where the data are recorded in 8 separate channels using different frequencies/wave numbers. The results obtained are summarized below.

1. For the real satellites we found large variations of the relative powers from event to event, which is probably due to a different number of pulses received by the satellite over the integration period. However, the large power difference remains unexpected in one case. Over a short time scale (≤ 10 sec) the relative power difference seems to be highly stable.

2. For NEIAL events we found that variations of the relative power between channels well above both the estimated and expected 1-sigma level occur over signal pre-integrated profiles, and a few profiles within 1 hour of data where the power radiated by NEIALs varies systematically with wavelength/wave number (k).

3. The amplitude enhancement of upgoing and downgoing ion-acoustic waves occurs at somewhat different altitudes and different power levels. These observational facts are modeled using the parametric decay of beam driven Langmuir waves in an inhomogeneous medium [*Forme et al*., 2001]. We suppose that the heating effects by plasma waves, which may be related to parametric decay instabilities of Langmuir waves driven by precipitating soft energy electron beams, play an important role in ion upflow in the topside ionosphere.

Table 5.1: List of Channels of GUP0 Used at the ESR

Channel	Frequency (MHz)	Pulse Length (μsec)	Range (km)
1	498.875	360	294 - 921
2	500.125	360	237 - 864
3	499.375	360	180 - 807
4	500.375	150	123 - 750
5	499.625	360	294 - 921
6	500.625	360	237 - 864
7	499.875	360	180 - 807
8	500.875	150	123 - 750

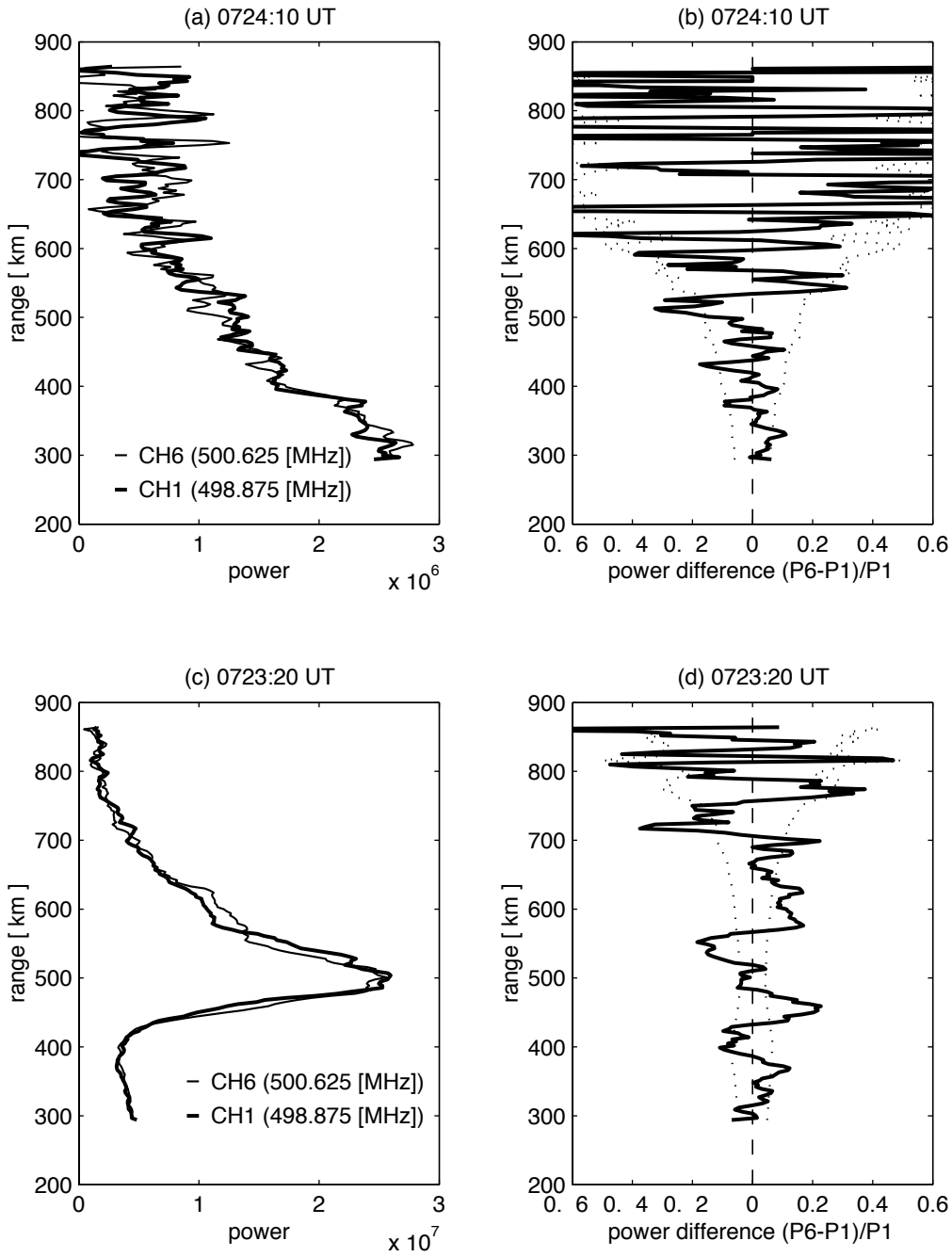

Figure 5.1: Power profiles from two different receiver channels obtained from the ESR. The power of channel 6 has been corrected for the relative gain difference (see text in Section 5.2). (a) Normal IS signals and (c) naturally enhanced ion-acoustic lines (NEIALs). The right panels ((b) and (d)) show normalized power differences. Dotted lines indicate estimated 1-sigma level derived from equation (5.3).

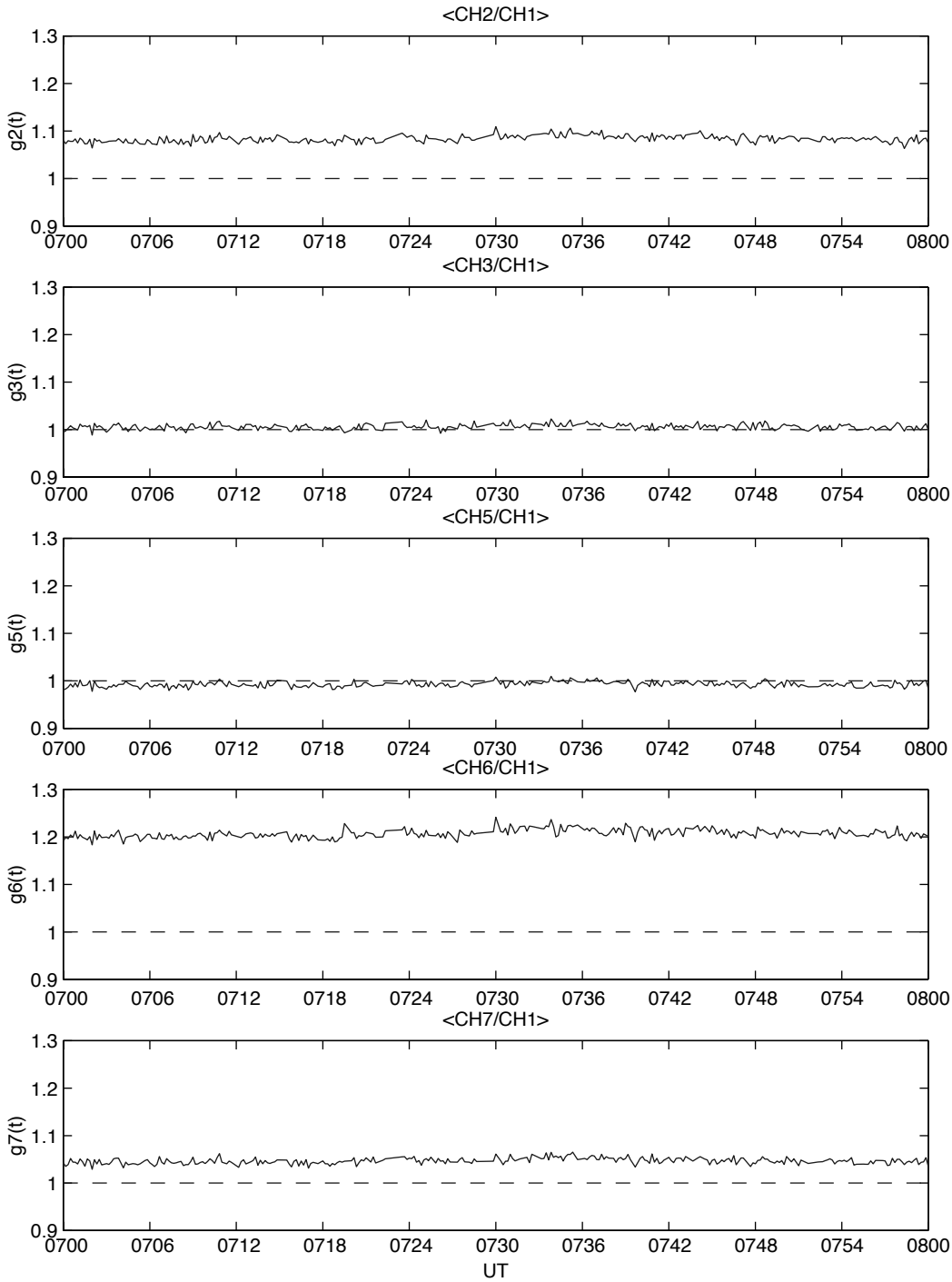

Figure 5.2: Estimated relative gains between channels over time between 0700 and 0800 UT on July 6, 1998.

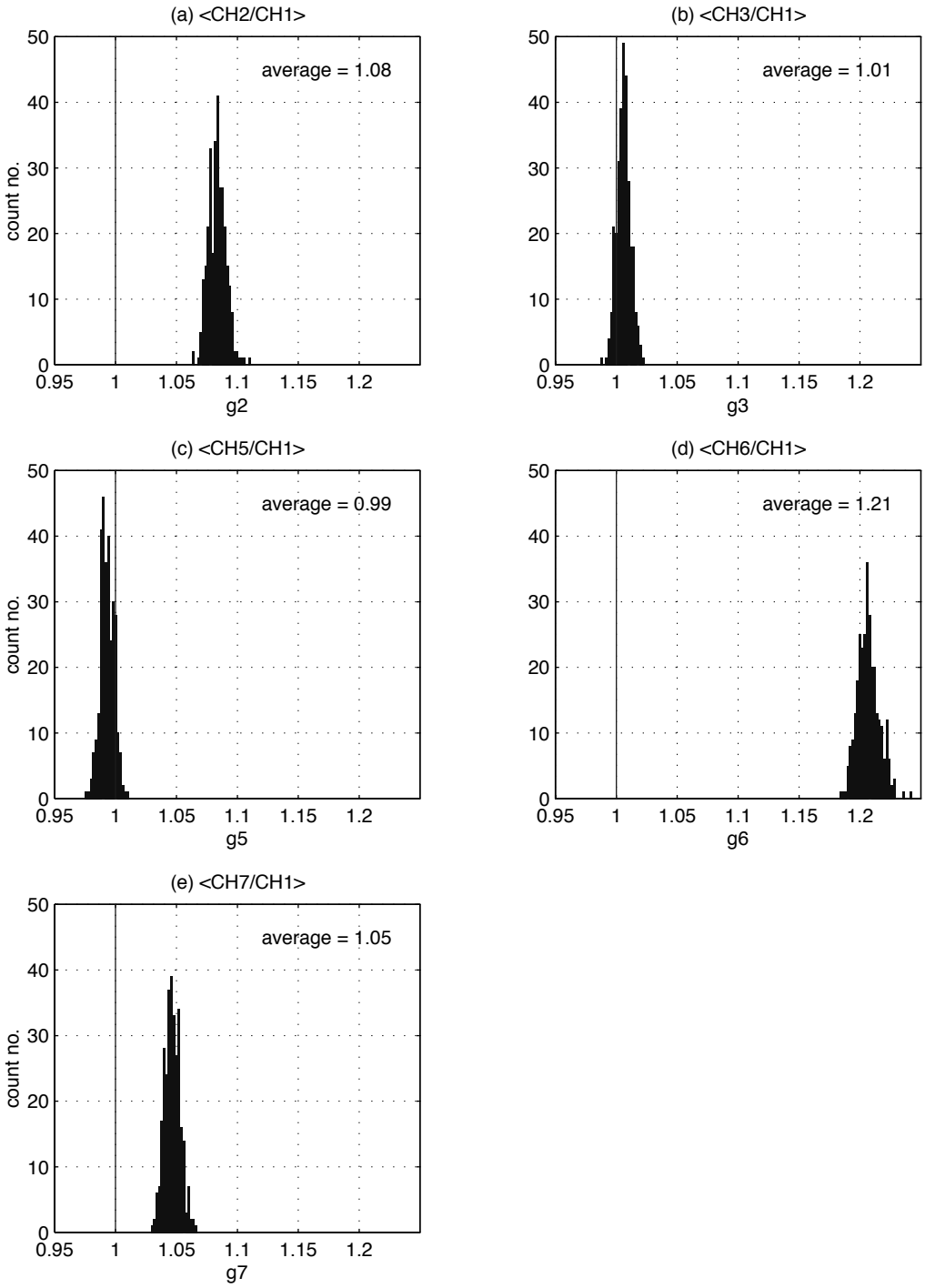

Figure 5.3: Distributions of the relative gains over the time period shown in Figure 5.2.

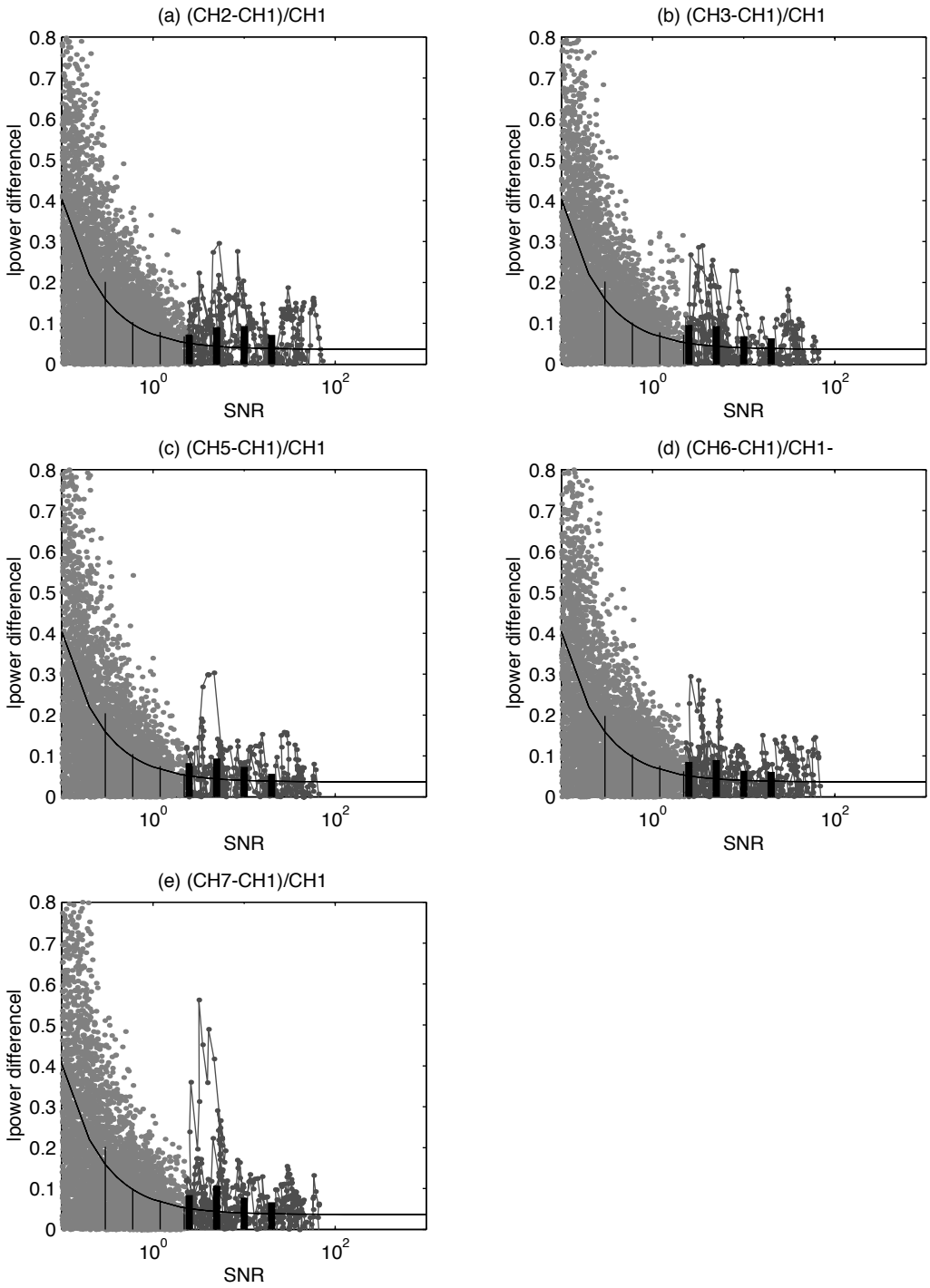

Figure 5.4: Relative power differences between channels over signal-to-noise ratio (SNR). Vertical bars indicate the 1-sigma levels that are calculated from the distribution of data points falling within corresponding SNR bins. The boundaries of the SNR bins are 0.2, 0.5, 1, 1.5, 3, 7, 20 and 100. Gray dots are from normal IS signals, and thin vertical bars indicate the respective 1-sigma levels. Black dots (connected by lines) are from NEIAL data, and the thick vertical bars indicate their respective 1-sigma levels. The curve represents equation (5.3).

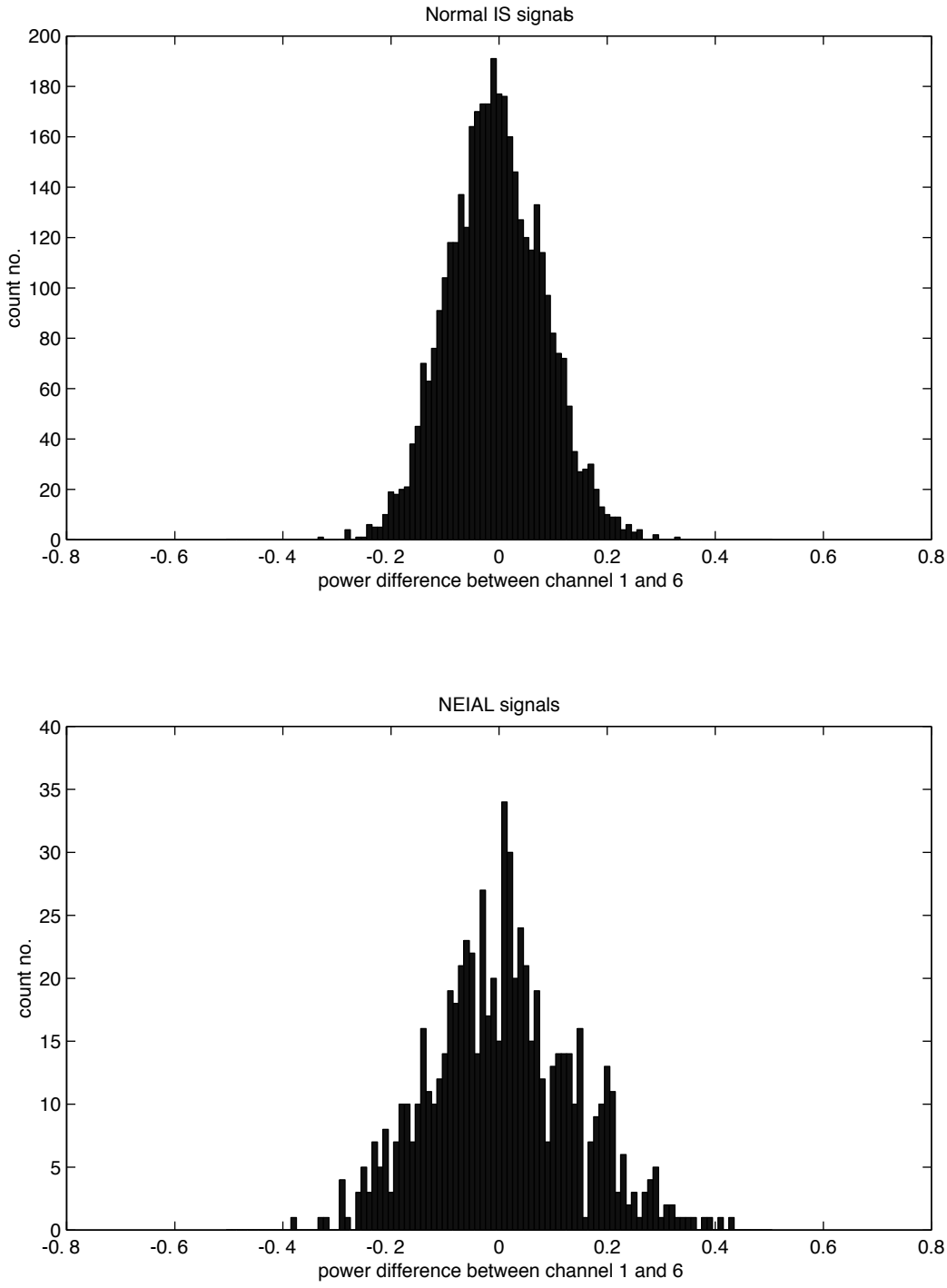

Figure 5.5: Distributions of the power differences between two channels (1 and 6) in normal IS signals (upper panel) and in NEIAL signals (lower panel). Each power difference is mapped by using equation (5.3) to a SNR = 1.

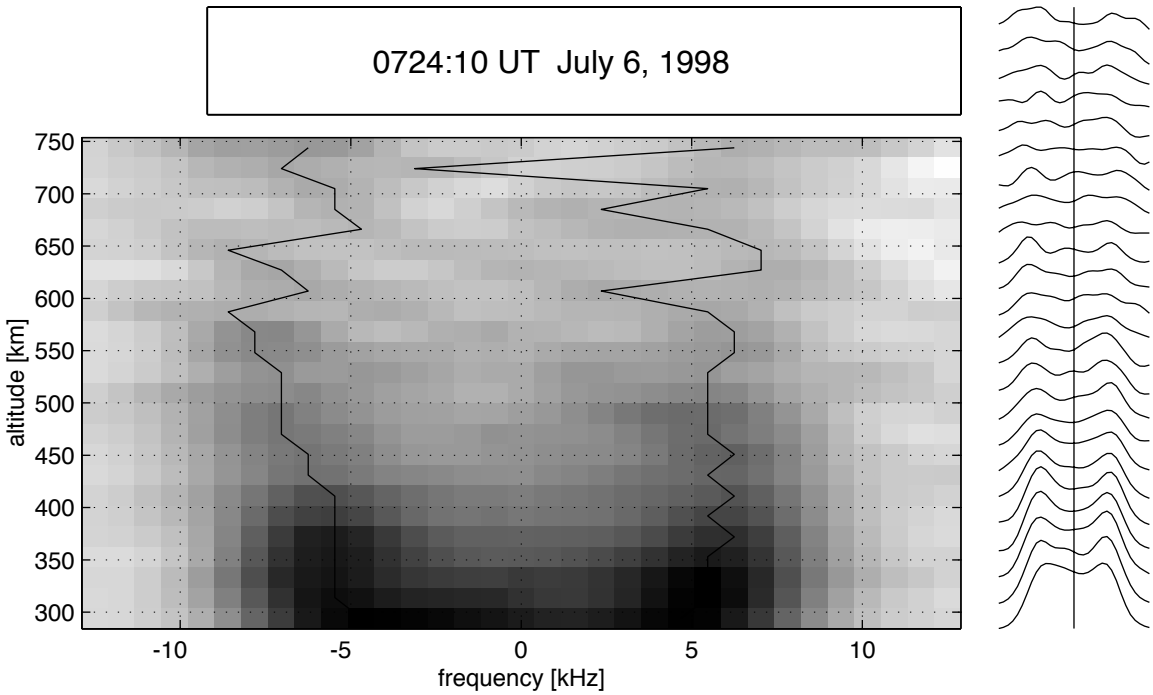

Figure 5.6: IS spectra measured with the ESR. (Left panel); The range corrected spectral power, coded with a gray scale, over the frequency on the x axis and range on the y axis. The black lines follow the positions of each of the ion-acoustic peaks. (Right panel); The same spectra as line plots. Each spectral intensity is normalized.

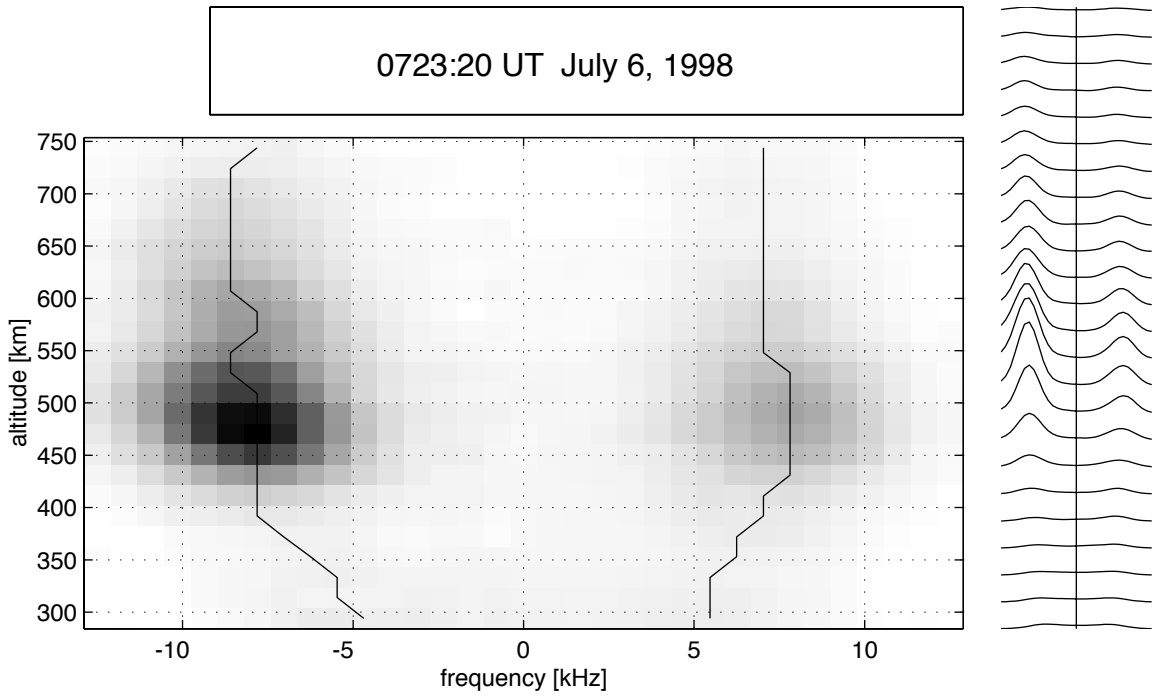

Figure 5.7: Same format as Figure 5.6, but for NEIAL event.

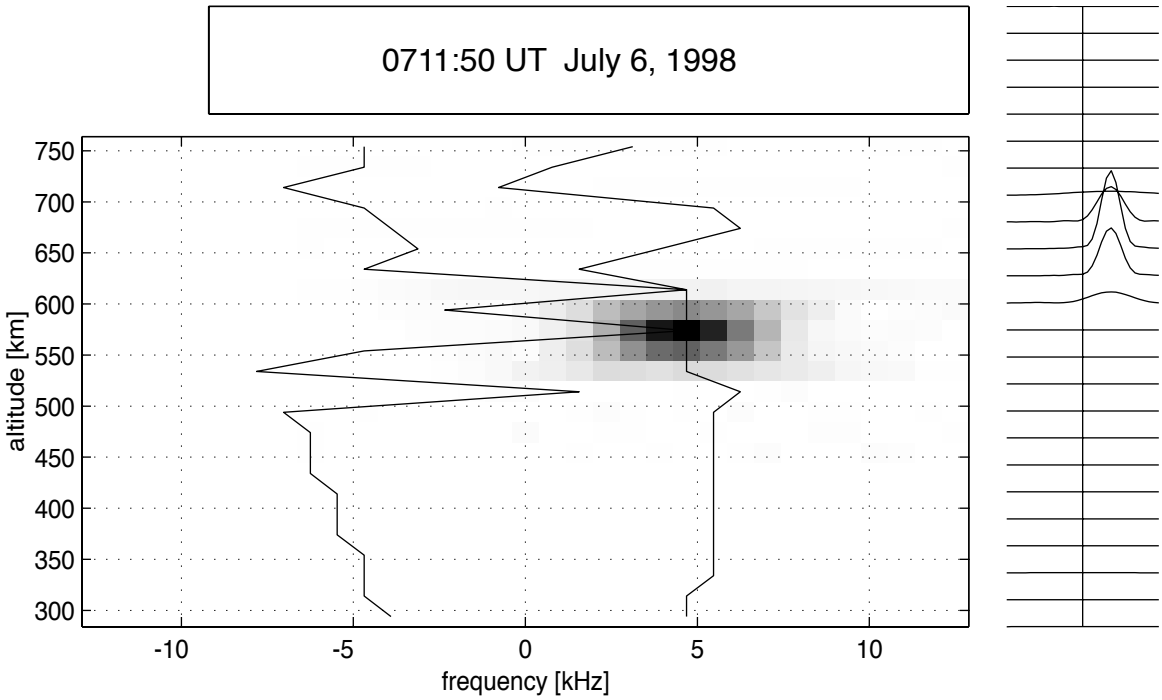

Figure 5.8: Same format as Figure 5.6, but for echoes from a real satellite.

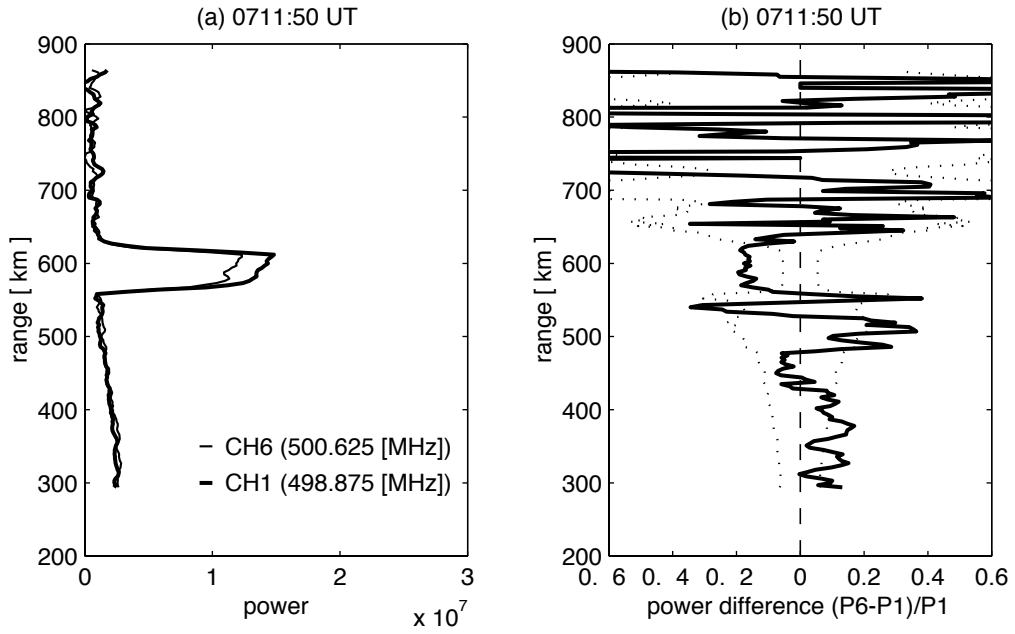

Figure 5.9: Same format as Figure 5.1, but for echoes from a real satellite.

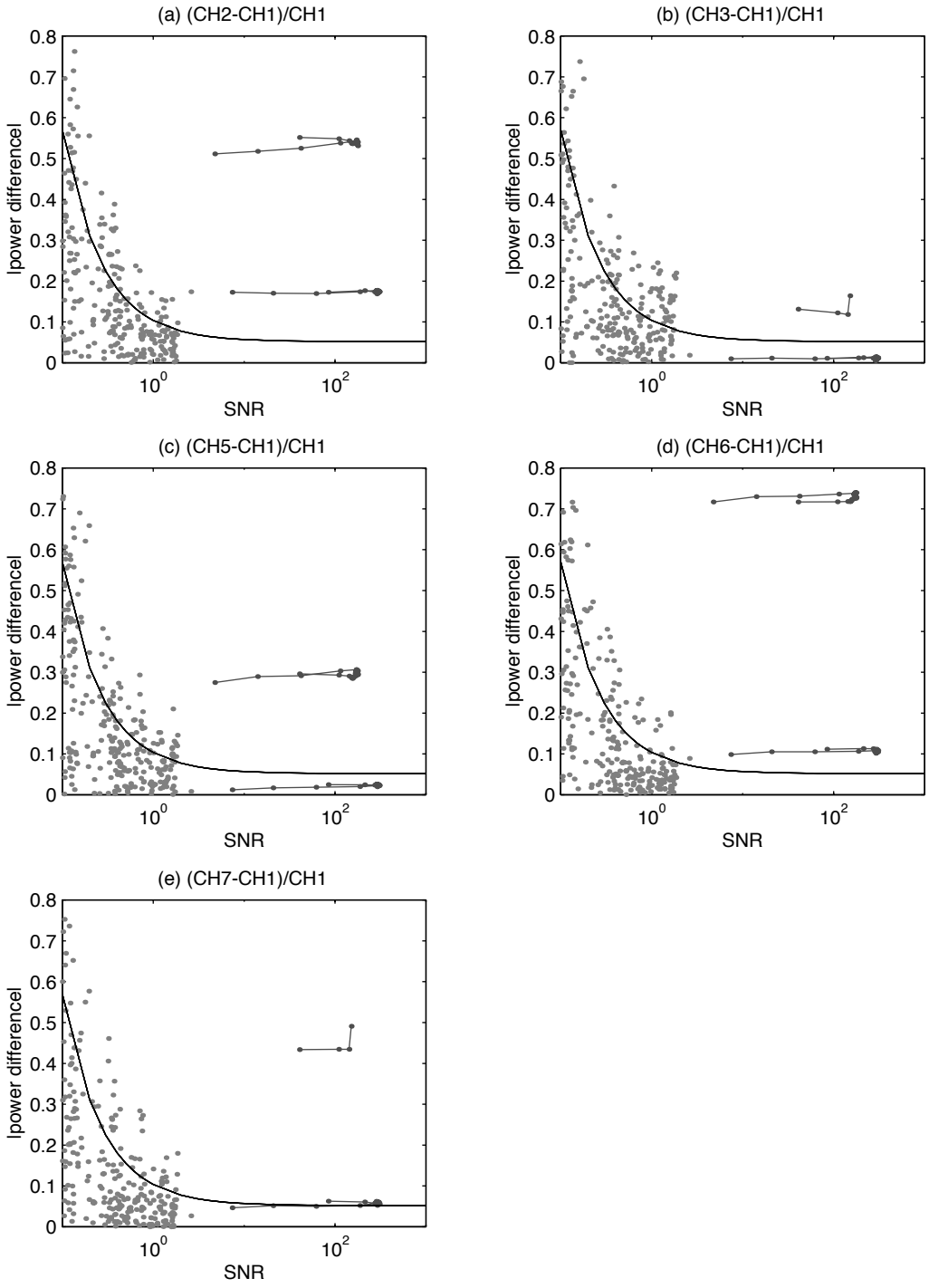

Figure 5.10: Relative power differences for real satellites in the same format as Figure 5.4. Black lines at the high SNR are from ranges with power enhancements from real satellites.

Chapter 6

Conclusions and Suggestions for Future Studies

Three investigations on the generation mechanisms of ion upflow in the ionosphere were carried out using data from the EISCAT Svalbard radar (ESR), the EISCAT VHF radar, and the DMSP satellites.

The simultaneous observations with the ESR and the DMSP satellites provide, for the first time, a systematic investigation on the occurrence regions of ion upflows in the dayside topside ionosphere. The distributions of field-aligned (FA) ion velocities in each of several magnetospheric regions suggest that ion upflows occur not only in the cusp and cleft (the low-altitude portion of the low-latitude boundary layer (LLBL)) which have been considered as ion upflow regions, but also in the topside ionosphere connected to the mantle region. The ion upflows seldom occur either in the Boundary Plasma Sheet (BPS) or in the Central Plasma Sheet (CPS) in the dayside high latitudes. Almost all the events where the average ion velocity is more than 100 m s^{-1} are associated with soft electron precipitation (differential energy flux of electrons at 100 eV > 10^7 eV cm^{-2} s^{-1} sr^{-1} eV^{-1}). Although soft electron precipitation also exists in the BPS, the associated ion velocities are mostly less than 100 m s^{-1}. The present results indicate that soft particle precipitation is the predominant source driving *F* region ion upflow, but it works on ion upflow effectively only in the higher latitude regions in the dayside and not in the BPS.

A case study using the ESR and the EISCAT VHF radar simultaneously has shown that FA ion upflows observed at an altitude of 665 km in the cusp are associated with significant anisotropy of ion temperature, isotropic increases of electron temperature and enhancements of electron density. There is no clear correspondence between the enhancements of the electric

field strength and the occurrence of the ion upflows. This suggests that the ion upflow is driven primarily by precipitation. The energy of soft particle precipitation is supplied to the ions in the *F* region/topside ionosphere via wave-particle interaction, such as wave-induced transverse ion heating, and an upward parallel electric field due to anomalous resistively produced by plasma turbulence. The data support that in addition to direct precipitation effects, namely enhanced ambipolar diffusion and heat flux, wave-particle interaction may play an important role in ion upflow in the *F* region/topside ionosphere. The difference of the occurrence frequency of ion upflow at each region may hence depend on the existence of the effect of the wave-particle interaction.

In order to understand the plasma waves related to the ion upflow, the *k*-dependence of the received power in high signal-to-noise ratio (SNR) conditions, occurring for naturally enhanced ion-acoustic lines (NEIALs) and for real satellites, is investigated by using data obtained from the ESR, where the data are recorded in 8 separate channels using different frequencies. We found that variations of the relative power between channels well above both the estimated and expected 1-sigma level occur over signal pre-integrated profiles. The most plausible explanation we can suggest is that the frequency/wave number (*k*) dependence of the power in NEIAL events has its origin in the scattering medium itself. The observational facts are at least modeled using the parametric decay of beam driven Langmuir waves in an inhomogeneous medium [*Forme et al.*, 2001].

The conclusions from these three investigations are that wave-particle interactions are significantly important for ion upflow in the polar topside ionosphere, as well as ion heating in the high-energy part seen in ion conics and TAIs in the bottomside magnetosphere. Although the energy of soft electron precipitation is considered as the main source of the ion upflow, this thesis shows that strong ion upflow ($\geq$ 100 m s^{-1}) is not directly driven by soft electron precipitation. Strong ion upflows during and after the NEIALs occur via interaction between ions and plasma waves induced by soft electron precipitation. From the result mentioned above, generation mechanisms of ion upflow must have transverse ion heating and upward acceleration by wave-particle interaction while the induced plasma waves decay. The interaction is considered to frequently occur in the vicinity of the cusp. Other approaches will certainly be needed to further understand the proposed mechanism. We propose here three experiments through which one can more extensively understand the relations between ion upflow and plasma instabilities.

1. Statistical studies of NEIALs observed with the ESR

NEIALs observed with the EISCAT UHF radar in Tromsø have been statistically investigated by *Rietveld et al*. [1996]. The distribution of the occurrence of NEIALs as a function of universal time (UT) shows a general period of maximum occurrence in the 12 to 24 UT (approximately 14 to 02 magnetic local time (MLT)). The distribution probably reflects the times when the auroral oval is above Tromsø which is most likely in the evening. On the contrary, NEIALs observed with the ESR are frequently received in the cusp around noon, due to its latitudinal location. Since plasma waves associated with ion heating are slightly different between the dayside and nightside polar regions [*André et al*., 1998], the characteristics of NEIALs observed with the ESR may be different from those obtained from the EISCAT UHF radar. It should be also noted that NEIALs are more frequently observed with the EISCAT VHF radar (224 MHz and $k_{\mathrm{VHF}} \approx 9.4$ m^{-1}) than with the EISCAT UHF radar (931 MHz and $k_{\mathrm{UHF}} \approx 39.1$ m^{-1}). The difference is probably due to the wave number dependence of the ion-acoustic waves. Statistical studies of the occurrence frequency of NEIALs with the ESR (500 MHz and $k_{\mathrm{ESR}} \approx 21$ m^{-1}), whose wave number dependence is probably approximately between the EISCAT UHF and VHF radars, will also help us to understand the physical mechanism responsible for NEIALs.

2. Simultaneous observations with the EISCAT radar system and in-situ measurements

The IS radars enable us to examine time and height distributions of several plasma parameters, but they are not capable of providing direct information on plasma waves associated with plasma instabilities. On the contrary, in-situ measurements such as satellites and sounding rockets carrying plasma wave instruments enable us to examine the characteristics of plasma instabilities associated with plasma waves, but they cannot provide time and height distributions of several plasma parameters. Hence simultaneous observations with the EISCAT radar system and in-situ measurements complement each weak point to aid in understanding these relations between ion upflow and plasma instabilities. *Yoshida et al*. [2000] have shown the relation between ELF waves, ion conics, and ion upflow around the nightside inverted-V region, by using simultaneous observations between the Akebono satellite and the EISCAT radars in Tromsø. Since EISCAT observations have been recently coordinated with Cluster II satellite observations, a relatively high number of simultaneous

events including ion upflow phenomena can be found in the dayside around the cusp. Cluster II is composed of 4 simultaneous satellite measurements hundreds to thousands of kilometers apart, and also the magnetic conjunction situation is different from that of most other satellites because of the polar orbits with an apogee of approximately 20 and a perigee of approximately 4 Earth's radii. Those simultaneous observations allow for the investigations of the influence of plasma waves to ions in both the ionosphere and the magnetosphere.

3. Comparison between the results of modeled and observed dynamic behavior of ion upflow

Statistical and simultaneous observations as described above can be used to estimate the physical mechanism of plasma instability associated with ion upflow. The relation of the plasma instability to ion acceleration will be examined from plasma parameters obtained from the ESR just before and after NEIALs. It is, however, difficult to estimate how plasma instability affects ion upflow from the observational data. Although previous models indicate that precipitation effects, particularly enhanced ambipolar diffusion, are sufficient to explain the results of ion upflow from the IS radar data [*Liu et al*., 1995; *Caton et al*., 1996; *Blelly et al*., 1996], additional physical processes are required to explain the observed ion upflow around NEIALs [e.g., *Wahlund et al*., 1992a]. Hence a model including microscopic processes such as wave-particle interactions is needed to explain such ion upflow phenomena. Using such a model, we will be able to understand interactions between plasma waves and ions around NEIALs, which should in turn be confirmed by observations.

Finally, the ion upflow and outflow phenomena that we focus on in this thesis are considered to occur not only on the Earth, but also on other planets such as Venus and Mars. These physical mechanisms obtained on the Earth will also help researchers understand the generation mechanisms of ion outflow occurring on other planets.

Appendix A

Ion Motions in the Polar Topside Ionosphere

In this appendix, we quantitatively examine the effect of ion accelerations due to the external field on the ion motions in the polar topside ionosphere, where local magnetic field lines are nearly vertical and ions start to flow up along the magnetic field line. At the beginning, we explain a general equation of momentum and investigate the relative importance of each term in the equation. If the momentum equation is correct, we can determine unknown parameters such as the ion-neutral collision frequency ν_{in} and neutral velocity V_n from observational results. However, it should be noted that the momentum equation cannot be applied to the ion upflow phenomena accompanied with the naturally enhanced ion lines (NEIALs), which we mainly treat in this thesis. In Section A.1, we estimate the contributions of each force in momentum equation of ions to ion motions in the topside ionosphere. In Section A.2, we compare the theoretical estimation described in Section A.1 with observational results using the EISCAT Svalbard radar (ESR).

A.1 Theoretical Formulation

The main ion and neutral species in the topside ionosphere, around an altitude between 400 km and 700 km, are the oxygen ion (O^+) and atomic oxygen (O), respectively. The number density of O is approximately 10^{12} - 10^{14} m^{-3} and a few 10 to a few 100 times larger than that of O^+ (see Figure 1.1). It means that the topside ionosphere is partially ionized plasma, as mentioned in Section 1.1.

The topside ionosphere includes the boundary between collision and diffusion dominant

regions. The mean free path of ions λ_i, which is related to the collision between O^+ and O, is written as

$$\lambda_i = \frac{1}{n_n \sigma_{in}} , \tag{A.1}$$

where n_n is number density of neutrals (O) and σ_{in} is the cross section between O^+ and O. Because the cross section σ_{in} is approximately $3\times10^2\times$ (Bohr radii)$^2 \approx 10^{-18}$ m^2 for both the resonance charge exchange and the momentum transfer [*Pesnell et al*., 1993], the mean free path of ions is approximately 10 km to 1000 km in the topside ionosphere. This indicates that the collisions between O^+ and O lessen with an increase in altitude. The scale height of ions H_i is related to the thermal diffusion, and is written as

$$H_i = \frac{k_B\left(T_i + T_e\right)}{m_i \left|\vec{g}\right|} . \tag{A.2}$$

In the case of the total temperature of ions and electrons being approximately 3000 K in the topside ionosphere, the scale height of the ions H_i is approximately 200 km, which is intermediate between the minimum and maximum length of the mean free path. This means that ions can freely move with the thermal velocity at the upper part of the topside ionosphere (called the exosphere), whereas collisions between O^+ and O still dominate ion motions at the lower part of the topside ionosphere (called the barosphere). For that reason we shall discuss both thermal and collision forces in the topside ionosphere in detail.

A general momentum equation for the topside ionospheric ions is written as

$$\begin{aligned} & n_i m_i \frac{\partial \vec{V_i}}{\partial t} + n_i m_i \left(\vec{V_i}\cdot\nabla\right)\vec{V_i} \\ & = -\nabla P_i + n_i k_B\left(T_{i//} - T_{i\perp}\right)\frac{1}{\left|\vec{B}\right|}\frac{\partial\left|\vec{B}\right|}{\partial s} + \nabla\cdot\vec{\tau_i} - n_i m_i \vec{g} + n_i e\left(\vec{E} + \vec{V_i}\times\vec{B}\right) \\ & \quad - m_i\left(Q_i - L_i\right)\left(\vec{V_i} - \vec{V_n}\right) - n_i m_i \nu_{in}\left(\vec{V_i} - \vec{V_n}\right) - n_i m_i \nu_{ie}\left(\vec{V_i} - \vec{V_e}\right) \\ & \quad + \frac{m_{in} z_{in} \nu_{in}}{k_B T_{in}}\left(\vec{q_i} - \frac{n_i m_i}{n_n m_n}\vec{q_n}\right) + \frac{3}{5}\frac{m_{ie}\nu_{ie}}{k_B T_{ie}}\left(\vec{q_i} - \frac{n_i m_i}{n_e m_e}\vec{q_e}\right) \end{aligned} , \tag{A.3}$$

where

$$m_{in} = \frac{m_i m_n}{m_i + m_n} \approx m_i$$
$$m_{ie} = \frac{m_i m_e}{m_i + m_e} \approx m_e \tag{A.4}$$

and

$$T_{in} = \frac{m_n T_i + m_i T_n}{m_i + m_n} \approx \frac{T_i + T_n}{2}$$
$$T_{ie} = \frac{m_e T_i + m_i T_e}{m_i + m_e} \approx T_e \quad , \tag{A.5}$$

Q and L are the production and loss ratios, $\vec{\tau}$ and $\vec{q}$ are the stress tensor and the heat flow vector. $\frac{\partial}{\partial s}$ indicates a differential toward parallel to the magnetic field lines. The subscripts *i*, *e*, and *n* are for ions (O^+), electrons, and neutral particles (O), respectively. When we consider ion motions only in the direction parallel to the magnetic field lines, the Lorentz force $n_i e \overrightarrow{V_i} \times \overrightarrow{B}$, related to a cyclotron gyration, disappears from equation (A.3). Hence the field-aligned (FA) momentum equation (A.3) can be written as

$$\begin{aligned}
&\frac{\partial \overrightarrow{V_{i//}}}{\partial t} + \left(\overrightarrow{V_{i//}} \cdot \frac{\partial}{\partial s}\right) \overrightarrow{V_{i//}} \\
&= -\frac{1}{n_i m_i} \frac{\partial P_{i//}}{\partial s} + \frac{k_B}{m_i}\left(T_{i//} - T_{i\perp}\right) \frac{1}{\left|\overrightarrow{B}\right|} \frac{\partial \left|\overrightarrow{B}\right|}{\partial s} + \frac{1}{n_i m_i} \frac{\partial \overrightarrow{\tau_{i//}}}{\partial s} - \overrightarrow{g_{//}} + \frac{e}{m_i} \overrightarrow{E_{//}} \\
&- \frac{\left(Q_i - L_i\right)}{n_i}\left(\overrightarrow{V_{i//}} - \overrightarrow{V_{n//}}\right) - \nu_{in}\left(\overrightarrow{V_{i//}} - \overrightarrow{V_{n//}}\right) - \nu_{ie}\left(\overrightarrow{V_{i//}} - \overrightarrow{V_{e//}}\right) \\
&+ \frac{z_{in}\nu_{in}}{n_i k_B T_{in//}}\left(\overrightarrow{q_{i//}} - \frac{n_i m_i}{n_n m_n} \overrightarrow{q_{n//}}\right) + \frac{3}{5} \frac{m_e \nu_{ie}}{n_i m_i k_B T_{ie//}}\left(\overrightarrow{q_{i//}} - \frac{n_i m_i}{n_e m_e} \overrightarrow{q_{e//}}\right)
\end{aligned} \quad . \tag{A.6}$$

In order to investigate ion acceleration per one particle, equation (A.3) is divided by $n_i m_i$. We describe, in sequence, the contributions of each term of equation (A.6) to the ion motions in the polar topside ionosphere.

The first term on the left hand side of equation (A.6) is the time differential of FA ion velocity. For the time scale of the IS radar observations (typically 1 min), this time differential term is sufficiently smaller than, for example, the gravity force. The second term on the left hand side of equation (A.6), called the advection term, is also negligibly small when FA ion velocity is subsonic. Hence ion motions are usually considered in the steady state condition, which means that the upward forces must balance the downward forces.

The first term on the right hand side of equation (A.6) is the ion pressure gradient force. Parallel ion pressure can be described, using the ion density and the parallel ion temperature, as

$$P_{i//} = n_i k_B T_{i//} . \tag{A.7}$$

Since electron density decreases with increasing altitude in the topside ionosphere, this pressure gradient force acts on ions as an upward force. This force is the same order as the gravity force. For example, when ion temperature increases through frictional heating, as given by [e.g., *Schunk et al*., 1975; *St-Maurice and Laneville*, 1998]

$$T_i = T_n + \frac{m_i}{3k_B}\left|\overrightarrow{V_i} - \overrightarrow{V_n}\right| , \tag{A.8}$$

the upward pressure force increases with the ion temperature enhancements. To be exact, this frictional heating is due to resonant charge exchange collisions between O^+ and O, and the contribution perpendicular to the magnetic field lines is larger than that parallel to the magnetic field lines [e.g., *Schunk and Nagy*, 1980]. However, the ion temperature anisotropy due to the frictional heating becomes weak with higher altitudes in the topside ionosphere, because the influence of Coulomb collisions, which cause isotropic heating, increases with increasing altitude [e.g., *McCrea et al*., 1993].

The second term on the right hand side of equation (A.6) is the magnetic mirror force due to the ion temperature anisotropy. The temperature anisotropy $T_{i\perp}/T_{i//} \approx 2$ was found in the topside ionosphere [*Ogawa et al*., 2000a]. In the case of $T_{i\perp}$ = 4000 K and $T_{i//}$ = 2000 K at

665 km altitude, for example, the magnetic mirror force is approximately 0.5 m s^{-2}, which is 1 order smaller than the gravity force. Hence this term can be usually neglected in the topside ionosphere.

The third term on the right hand side of equation (A.6) is the height differential of the stress tensor. A general expression for the parallel stress tensor is given by *Schunk* [1975] as

$$\tau_{i//} \approx \frac{1}{4} n_i m_i \left[\left(\overrightarrow{V_i} - \overrightarrow{V_n} \right)_{//}^2 - \frac{1}{3} \left(\overrightarrow{V_i} - \overrightarrow{V_n} \right)^2 \right] . \quad \text{(A.9)}$$

For the neutrals, the main flows are horizontal, at speeds from 100 - 800 m s^{-1}, while the velocity gradients are in the FA direction. These conditions yield a large viscous stress effect. The viscosity associated with FA ion velocity is small. Large horizontal ion flows can occur, with speeds up to several km s^{-1}, but they are $E \times B$ drifts, and they exhibit little variation with altitude. The lack of a velocity gradient implies that viscous stress is not important even for these large drifts. The height differential of the stress tensor term is important if there are large relative drifts in the horizontal direction.

The fourth term on the right hand side of equation (A.6) is the gravity force, which accelerates ions downward along the vertical direction. The gravity force is approximately 9 m s^{-2} around 600 km altitudes. The gravity force is the main downward force in the polar topside ionosphere. The dip angle of the magnetic field line at Longyearbyen is 81.5˚ (see Table 2.1 and Figure 4.1), so the gravity force toward the magnetic field lines is written as

$$\overrightarrow{g_{//}} = \overrightarrow{g}_{vertical} \, sin(I) \, . \quad \text{(A.10)}$$

The magnitude of the gravity force toward the magnetic field lines at Longyearbyen is nearly the same as that along the vertical direction.

The fifth term on the right hand side of equation (A.6) is an electric force by the electric field. Ions interact with electrons through the electric field as well as Coulomb collision and heat conductance. Here we also consider the electron momentum equation in order to evaluate the electric force working ions. The FA momentum equation of electrons is given as

$$
\begin{aligned}
& n_e m_e \frac{\partial \overrightarrow{V_{e//}}}{\partial t} + n_e m_e \left(\overrightarrow{V_{e//}} \cdot \frac{\partial}{\partial s} \right) \overrightarrow{V_{e//}} \\
& = -\frac{\partial P_{e//}}{\partial s} + n_e k_B \left(T_{e//} - T_{e\perp} \right) \frac{1}{\left| \overrightarrow{B} \right|} \frac{\partial \left| \overrightarrow{B} \right|}{\partial s} + \frac{\partial \overrightarrow{\tau_{e//}}}{\partial s} - n_e m_e \overrightarrow{g_{//}} - n_e e \overrightarrow{E_{//}} \\
& - m_e \left(Q_e - L_e \right) \left(\overrightarrow{V_{e//}} - \overrightarrow{V_{n//}} \right) - n_e m_e \nu_{en} \left(\overrightarrow{V_{e//}} - \overrightarrow{V_{n//}} \right) - n_e m_e \nu_{ei} \left(\overrightarrow{V_{e//}} - \overrightarrow{V_{i//}} \right) \\
& - \frac{1}{5} \frac{m_e \nu_{en}}{k_B T_{en//}} \left(\overrightarrow{q_{e//}} - \frac{n_e m_e}{n_n m_n} \overrightarrow{q_{n//}} \right) + \frac{3}{5} \frac{m_e \nu_{ei}}{k_B T_{ei//}} \left(\overrightarrow{q_{e//}} - \frac{n_e m_e}{n_i m_i} \overrightarrow{q_{i//}} \right)
\end{aligned}
\quad . \qquad \text{(A.11)}
$$

The magnetic mirror force on electrons can be neglected, based on the fact that there is no electron temperature anisotropy obtained from the IS radar observations described in Chapter 4. The force caused by the electron stress tensor is also small. The collision frequency between the electrons and neutrals (O) in the topside ionosphere is written as [*Schunk and Nagy*, 2000]

$$
\nu_{en} = 8.9 \times 10^{-17} n_n \sqrt{T_e} \left(1 + 5.7 \times 10^{-4} T_e \right) , \qquad \text{(A.12)}
$$

while the collision frequency between the electrons and ions (O^+) in the topside ionosphere is written as [*Schunk and Nagy*, 2000]

$$
\nu_{ei} = 54.5 \times 10^{-6} \frac{n_i}{T_{ei}^{3/2}} . \qquad \text{(A.13)}
$$

ν_{en} is at least one order smaller than ν_{ei}, whose value is a few 10 s^{-1} in the topside ionosphere. We can hence ignore the electron-neutral collision term and electron-neutral heat flux term in equation (A.11). Since the other terms multiplied by electron mass m_e can be ignored, except for the electron-ion collision and heat flux terms, the electric field derived from the FA electron momentum equation (A.11) is written as

$$\begin{aligned}\overrightarrow{E_{//}} &= -\frac{1}{n_e e}\frac{\partial P_{e//}}{\partial s} - \frac{m_e \nu_{ei}}{e}\left(\overrightarrow{V_{e//}} - \overrightarrow{V_{i//}}\right) + \frac{3}{5}\frac{m_e \nu_{ei}}{n_e e k_B T_{ei//}}\overrightarrow{q_{e//}} \\ &= -\frac{1}{n_e e}\frac{\partial P_{e//}}{\partial s} - \frac{m_i \nu_{ie}}{e}\left(\overrightarrow{V_{e//}} - \overrightarrow{V_{i//}}\right) + \frac{3}{5}\frac{m_i \nu_{ie}}{n_e e k_B T_{ei//}}\overrightarrow{q_{e//}}\end{aligned}, \qquad \text{(A.14)}$$

where $n_e m_e \nu_{ei} = n_i m_i \nu_{ie}$ and $n_e \approx n_i$. This electric field is called "the ambipolar electric field." The value is approximately $1\,\mu$V m^{-1} in the topside ionosphere. The fifth term on the right hand side of equation (A.6), for which is substituted this ambipolar electric field, is usually one of the main upward forces in the topside ionosphere.

The sixth term on the right hand side of equation (A.6) indicates a force due to chemical reactions. Regarding the production ratio Q_i, the ionization caused by particle precipitation is approximately 10^9 m^{-3} per second at maximum in the topside ionosphere even if the cusp-like (burst) soft electron precipitation occurs, which is smaller than the background electron density (approximately 10^{11} m^{-3}) in the topside ionosphere. On the other hand, the loss ratio L_i, can be derived from the following chemical reactions [e.g., *Schunk and Walker*, 1970; *Schunk and Nagy*, 2000]

$$\begin{aligned}L_i &= \left(\alpha_r\left[O^+\right] + \alpha_1\left[NO^+\right] + \alpha_2\left[O_2{}^+\right]\right) n_e \\ &\approx \left(\alpha_r n_e + k_1\left[N_2\right] + k_2\left[O_2\right]\right)\left[O^+\right] \\ &\approx \left(\alpha_r n_e + k_1\left[N_2\right] + k_2\left[O_2\right]\right) n_e\end{aligned}, \qquad \text{(A.15)}$$

where

$$\begin{aligned}
&O^+ + e^- \xrightarrow{\alpha_r} N + h\nu && \alpha_r = 3.7\times10^{-18}\left(250/T_e\right)^{0.7} && [m^3 s^{-1}] \\
&NO^+ + e^- \xrightarrow{\alpha_1} N + O && \alpha_1 = 4.0\times10^{-13}\left(300/T_e\right)^{0.5} && [m^3 s^{-1}] \\
&O_2{}^+ + e^- \xrightarrow{\alpha_2} O + O && \alpha_2 = 7.4\times10^{-14}\left(1200/T_e\right)^{0.56} && [m^3 s^{-1}] \\
&O^+ + N_2 \xrightarrow{k_1} NO^+ + N && k_1 = 1.2\times10^{-18}\left(300/T_i\right) && [m^3 s^{-1}] \\
&O^+ + O_2 \xrightarrow{k_2} O_2{}^+ + O && k_2 = 2.0\times10^{-17}\left(300/T_i\right)^{0.5} && [m^3 s^{-1}]
\end{aligned}. \qquad \text{(A.16)}$$

It should be noted that we assume equilibrium conditions for the nitrogen monoxide ion (NO^+) and molecular oxygen ion ($O_2{}^+$) when neglecting the production of NO^+ and $O_2{}^+$ due to

solar radiation in the topside ionosphere. Below approximately 600 km altitude, loss processes through the rearrangements of O^+ into NO^+ and O_2^+ are still dominate in equation (A.15), because the number density of nitrogen molecules (N_2) and oxygen molecules (O_2) are larger than electron density n_e below the altitude (see Figure 1.1) although each reaction rate given by α_r, k_1, and k_2 has almost the same order. At any altitude, however, this loss ratio is less than 10^{-4} n_e in the topside ionosphere. Hence the force regarding the chemical reactions can be neglected in the topside ionosphere.

The seventh term on the right hand side of equation (A.6) is the ion-neutral collision force. This force works on ions as the resistance due to the neutral motion. The ion-neutral collision frequency is written as [*Schunk and Nagy*, 2000]

$$\nu_{in} = 3.67\times10^{-17}\, n_n\sqrt{T_{in}}\left(1-0.064\log_{10}T_{in}\right)^2 , \qquad \text{(A.17)}$$

and the value is between 0.01 and 1 s^{-1} in the topside ionosphere. Because parallel ion velocity $V_{i//}$ can take a large value (more than 100 m s^{-1}) in the topside ionosphere, this force is one of the main forces in the topside ionosphere as well as in the *F* region ionosphere.

The eighth term on the right hand side of equation (A.6) is the ion-electron collision force. This collision is the Coulomb interaction between ions and electrons. The Coulomb collision frequency between O^+ and electron is written as

$$\nu_{ie} = 18.5\times10^{-10}\frac{n_i}{T_{ie}^{3/2}} , \qquad \text{(A.18)}$$

and this value is a few 10 times smaller than ν_{in} in the topside ionosphere. This Coulomb collision effect becomes important at a higher altitude. This term is eliminated through the ambipolar electric field described in equation (A.14), which is derived from electron momentum equation (A.11).

The ninth term on the right hand side of equation (A.6) is a force due to heat flux of ions and neutrals, which interact through the collision between them. Parameter z_{in}, for the resonant charge exchange collision is described in *Schunk* [1975] in detail. This force can be divided into two factors and written by using ion and neutral temperature gradients [*Conrad and Schunk*, 1979]. When the ion (neutral) temperature increases with increasing altitude, the term associated with the ion (neutral) temperature gradient works as an upward (downward)

force. Although the coefficient of the neutral temperature gradient term takes a large value for $T_n \approx T_i$, the neutral temperature gradient is generally small in the *F* region/topside ionosphere; therefore, the O^+ thermal diffusion associated with this factor is not likely to be significant under normal ionospheric conditions [*Conrad and Schunk*, 1979]. On the other hand, the O^+ temperature gradient can be large throughout the dayside *F* region/topside ionosphere; however, the coefficient of the ion temperature gradient is small [*Conrad and Schunk*, 1979]. Hence this force can be usually neglected in the topside ionosphere.

The last term on the right hand side of equation (A.6) is a force due to heat flux of electrons and ions, which interact through the collision between them. The first factor related to the ion heat flux $\overrightarrow{q_{i//}}$ can be negligible because the term is multiplied by m_e/m_i. When the velocity difference between ions, electrons and neutrals can be negligible, the electron heat flux is written as [*Conrad and Schunk*, 1979]

$$\overrightarrow{q_{e//}} = -\frac{25}{8}\left(\frac{k_B P_{e//}}{m_e\left(\nu_{ee}+\frac{13}{8}\nu_{ei}\right)}\right)\frac{\partial T_{e//}}{\partial s} = -\frac{25\sqrt{2}}{\left(8+13\sqrt{2}\right)}\frac{k_B P_{e//}}{m_e \nu_{ei}}\frac{\partial T_{e//}}{\partial s}\ , \tag{A.19}$$

where ν_{ei} is written in equation (A.13) and

$$\nu_{ee} = \frac{54.5}{\sqrt{2}}\times 10^{-6}\frac{n_i}{{T_{ei}}^{3/2}} \quad \left(=\frac{\nu_{ei}}{\sqrt{2}}\right). \tag{A.20}$$

The force associated with the electron heat flux is thus written as

$$-\frac{3}{5}\frac{\nu_{ie}}{n_i k_B T_{ie//}}\overrightarrow{q_{e//}} = \frac{15\sqrt{2}}{\left(8+13\sqrt{2}\right)}\frac{k_B \nu_{ie}}{m_e \nu_{ei}}\frac{T_{e//}}{T_{ie//}}\frac{\partial T_{e//}}{\partial s} \approx 0.8\frac{k_B}{m_i}\frac{\partial T_{e//}}{\partial s}\ . \tag{A.21}$$

When the electron temperature strongly increases with increasing altitude, for example, under conditions of particle precipitation, this force becomes as important as the ion pressure gradient force. Although this term, as well as the ion-electron collision term, is eliminated through the ambipolar electric field described in equation (A.14), it does not mean that the effect of the electron heat flux can be negligible, but it means that the effect of the ambipolar

electric field becomes small when the effect of the electron heat flux from the magnetosphere to the topside ionosphere becomes large.

Consequently ion and electron diffusion terms, due to those pressure gradient and gravity forces, and a collision term between ions and neutrals are considered to be the main forces in the polar topside ionosphere. Hence the FA ion momentum equation (A.6) is usually simplified as

$$\left(-\frac{1}{n_e m_i}\frac{d\left(n_e k_B T_{i//}\right)}{ds}-\frac{1}{n_e m_i}\frac{d\left(n_e k_B T_{e//}\right)}{ds}-\overrightarrow{g_{//}}\right)=\nu_{in}\left(\overrightarrow{V_{i//}}-\overrightarrow{V_{n//}}\right) \qquad \text{(A.22)}$$

in the polar ionosphere, using the ambipolar electric field derived from equation (A.12) and $n_i \approx n_e$. The effects of particle precipitation, electron heat flux and flectional heating are included on the left hand side of equation (A.22) as functions of the electron density n_e, the FA electron temperature $T_{e//}$, and the FA ion temperature $T_{i//}$.

A.2 Observational Results

Next we investigate the validity of equation (A.22), using observational results obtained from the ESR. Figure A.1 shows the diffusion term on the left hand side in equation (A.22) and the field-aligned (FA) ion velocity at an altitude of 452 km on December 8, 1999. It is clearly seen in Figure A.1 that the fluctuations of the diffusion term correlate with those of the ion velocity. When ion-neutral collision frequency ν_{in} and FA neutral velocity $V_{n//}$ are assumed constants, the relation between the diffusion term and the ion velocity is handled as a linear function according to equation (A.22). Conversely, if the relation between the diffusion term and the ion velocity, which are derived from observational data, can be expressed with a linear function, the inclination in the linear function should be interpreted as the ion-neutral collision frequency ν_{in}. Furthermore, the intercept of the axis of the ion velocity should be interpreted as the FA neutral velocity $V_{n//}$. In the following, the validity of equation (A.22) is discussed using the ion-neutral collision frequency ν_{in} derived from the inclination and modeled on equation (A.17).

Figure A.2 and Figure A.3 show the relation between the diffusion term and the FA ion velocity at four altitudes, 417, 452, 488, and 523 km, respectively. Every 2 min data for 2 hours are over-plotted in each panel. The ion velocity increases with the diffusion term at any

altitude. Line (A) indicates the results of a least square approximation from the x axis. Broken line (B) indicates the results of a least square approximation from the y axis. The difference between line (A) and line (B), associated with an ambiguity of the inclination, is small, and the larger inclination value is within 2 times that of the smaller one in many cases. This means that ν_{in} and $V_{n//}$, which are unknown quantities in equation (A.22), are almost constant for 2 hours. Therefore the inclination is regarded as the ion-neutral collision frequency ν_{in} at each altitude. Then, the intercept of the x axis is regarded as the FA neutral velocity $V_{n//}$.

Figure A.4 shows the results of the inclinations derived from the ESR data at different altitudes. An example of the top left panel in the Figure A.4 shows that reliable inclinations are obtained from observational data between 400 km and 550 km altitudes. This indicates that the ion velocities are well correlated with the diffusion terms for 2 hours. The larger inclination values at each altitude are within 3 times those of smaller ones. Below the altitudes of 400 km, only a few reliable inclinations are obtained. The black line indicates a height profile of the ion-neutral collision frequency ν_{in} obtained from the model described in equation (A.17). The neutral number density n_n and temperature T_n are derived from MSIS–E 90 [*Hedin*, 1991], and the ion temperature T_i is derived from the ESR data. Around 412 km and 452 km altitudes in the left upper panel in Figure A.4, the collision frequency derived from the observations corresponds to that obtained from equation (A.17). Above 488 km altitude, the collision frequency derived from the observations is approximately 2 times higher than that obtained from equation (A.17). The same features above 488 km are seen in other examples in Figure A.4. On the other hand, the collision frequency derived from the observations is lower than that from equation (A.17), when the inclinations are exactly decided below 400 km altitude in the lower left panel. Hence the derivation of ion-neutral collision frequency ν_{in} from the ESR data and equation (A.22) is possible only within altitude limits between approximately 400 and 600 km. However, this derivation from only observational data may also be helpful for constructing a realistic model, because theoretical ion-neutral (O^+ - O) collision frequency models remain a matter for debate [e.g., *Salah*, 1993].

The collision frequency obtained from equation (A.17) is in proportion to the neutral number density. The theoretical collision frequencies around 500 km altitude on November 26, 2000 (in the lower right panel of Figure A.4) are approximately 4 times larger than that on December 21, 1998 (in the upper right panel of Figure A.4). This is because the neutral density on November 26, 2000, near the solar maximum, is higher than those on December 21, 1998. The observational collision frequencies also show similar differences. The collision

frequencies at 488 km and 523 km on November 26, 2000 (also in the lower right panel of Figure A.4) are approximately 3 times higher than those on December 21, 1998 (also in the upper right panel of Figure A.4). It is likely that the collision frequencies obtained from the inclination also have a solar cycle dependence.

Figure A.5 shows an example of time variations of the collision frequency ν_{in} and the FA neutral velocity $V_{n//}$ at an altitude of 452 km, derived from the ESR data. Magnetic Local Time (MLT) ≈ UT + 3 hours ≈ Geographical Local Time (LT) + 2 hours. The upper panel in Figure A.5 shows the collision frequency derived from the observation at each 2 hours. The collision frequency at noon (around 11 UT) is higher than that at night (around 21 UT). When the diffusion term (in the middle panel of Figure A.5) and the ion velocity (in the lower panel of Figure A.5) have small fluctuations (e.g., those between 16 and 18 UT), the ambiguity of the collision frequency ν_{in} becomes relatively large. The collision frequency derived from equation (A.17), plotted as a solid line in the same upper panel, also has a similar change as that derived from the ESR data. It is mainly due to the variation of the neutral number density; the maximum is around noon and the minimum is around night.

The red line in the lower panel of Figure A.5 shows the FA neutral velocity $V_{n//}$ derived from the ESR data. The velocity changes from downward around noon to strongly upward around night. When we regard the FA neutral velocities at every 2 hours as offsets of the FA ion velocities, the change of direction of the relative velocities in the lower panel coincides with that of the diffusion term in the middle panel.

The neutral velocity $V_{n//}$ should generally be reflected by the meridional neutral wind described as

$$\overrightarrow{V_{n//}} = \overrightarrow{V_{n(South-North)}} \cos(I) , \qquad \text{(A.23)}$$

where I is the dip angle of the magnetic field line at Longyearbyen (see Figure 4.1). The ordinate in the right hand of the lower panel in Figure A.5 indicates the meridional neutral wind velocity. The positive (negative) velocities indicate motion to the southward (northward). According to equation (A.23), the FA neutral velocities observed on December 7, 1999 are interpreted as neutrals moving poleward with the velocity of 100 m s^{-1} around daytime and equatorward with the velocity of 700 m s^{-1} around nighttime. These trends agree with the directions and amplitudes of the average meridional neutral wind in the polar *F* region/topside

ionosphere [*Thayer et al.*, 1987]. The neutral velocities derived from observations at different altitudes between 400 km and 600 km also have the same trends, although they are not shown.

These observational results lead to the conclusion that the approximation of the FA ion momentum equation (A.22) is greatly useful in understanding ion motions in the polar topside ionosphere. Ion upward flows are often explained by thermal diffusion using equation (A.22).

As an exception, when the flectional heating is considerably strong or naturally enhanced ion lines are often seen, observational results rarely satisfy equation (A.22). In the former case, we must consider transportation of ions and electrons to the perpendicular direction as well as to the parallel direction. In the latter case, additional effects such as “anomalous” resistively produced by plasma turbulence [e.g., *Papadopolous*, 1977]

$$\overrightarrow{E_{//}} = \eta^{*}_{//} \overrightarrow{j_{//}} \ , \qquad \text{(A.24)}$$

may be needed to explain the observational results, because the left hand side in equation (A.22) becomes clearly smaller than the right hand side in equation (A.22) [*Wahlund et al.*, 1992a].

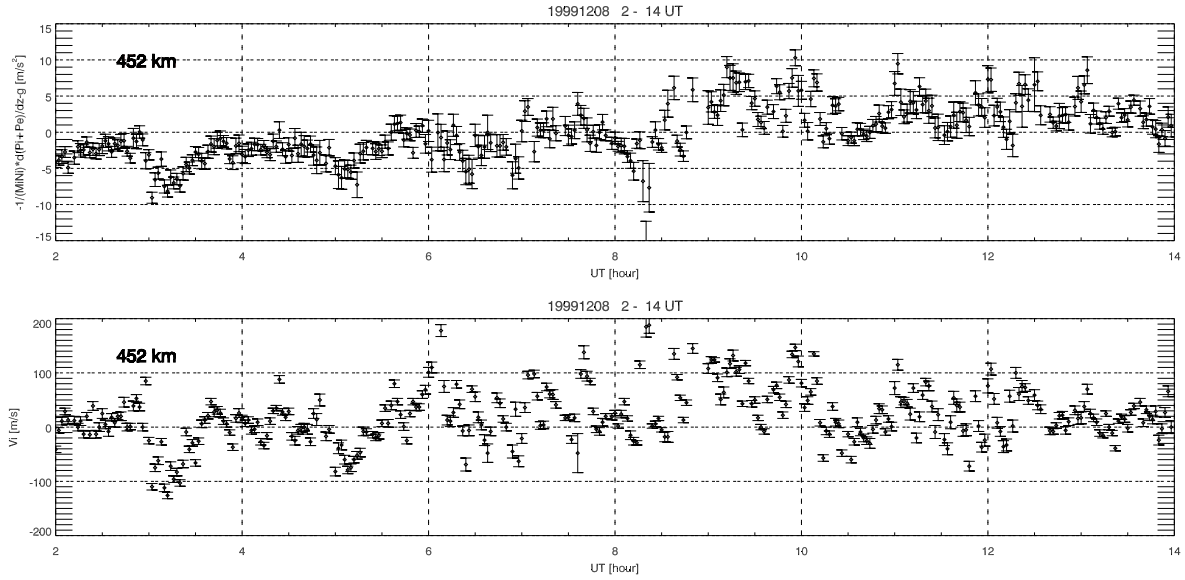

Figure A.1: Time variations of diffusion term (upper panel) and field-aligned (FA) ion velocity (lower panel) at an altitude of 452 km obtained from the ESR between 02 and 14 UT on December 8, 1999. Positive diffusion term and FA ion velocity are in an upward direction.

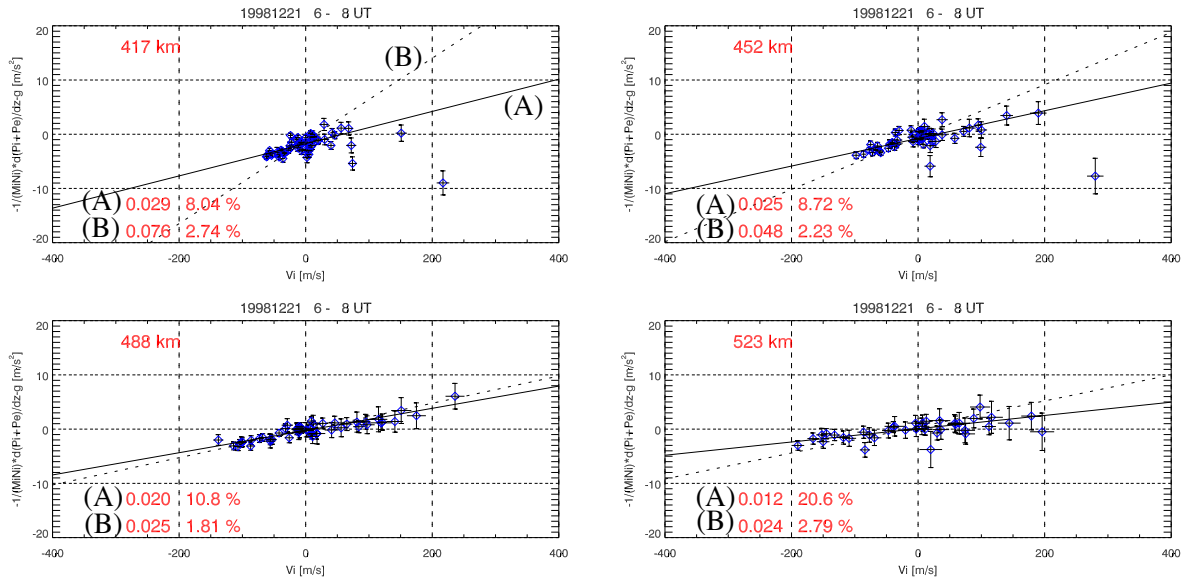

Figure A.2: Relation between diffusion term and field-aligned ion velocity obtained from the ESR between 06 and 08 UT on December 21, 1998. Numbers at lower left of each panel indicate inclinations of line (A) and (B).

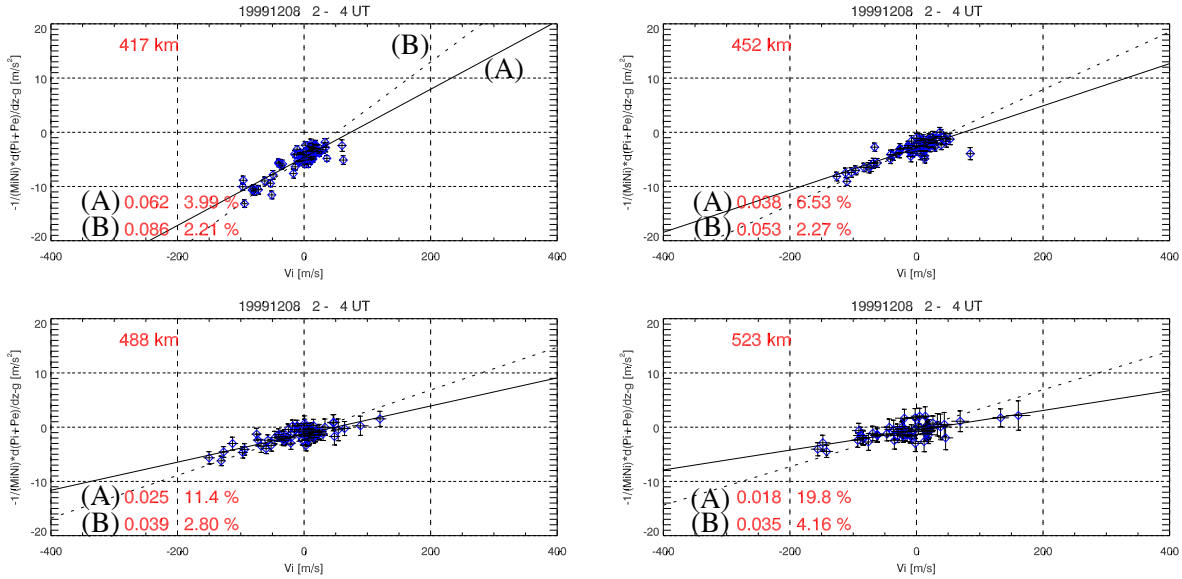

Figure A.3: Same format as Figure A.2, but between 02 and 04 UT on December 8, 1999.

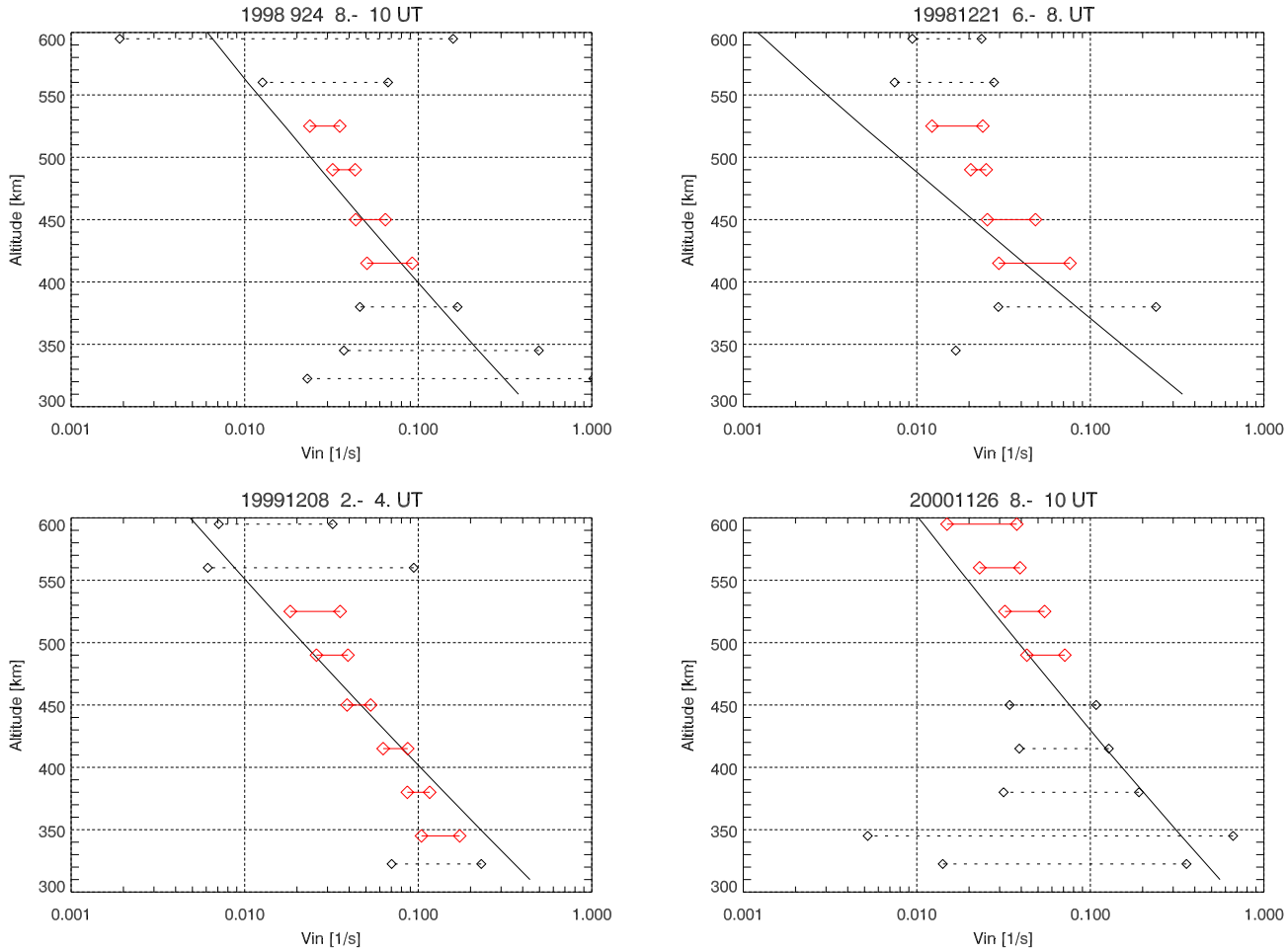

Figure A.4: Height variations of ion-neutral collision frequencies derived from observations and models. Red lines indicate that larger inclination value is within 3 times that of the smaller one. Black line indicates a collision frequency obtained from model described in equation (A.17).

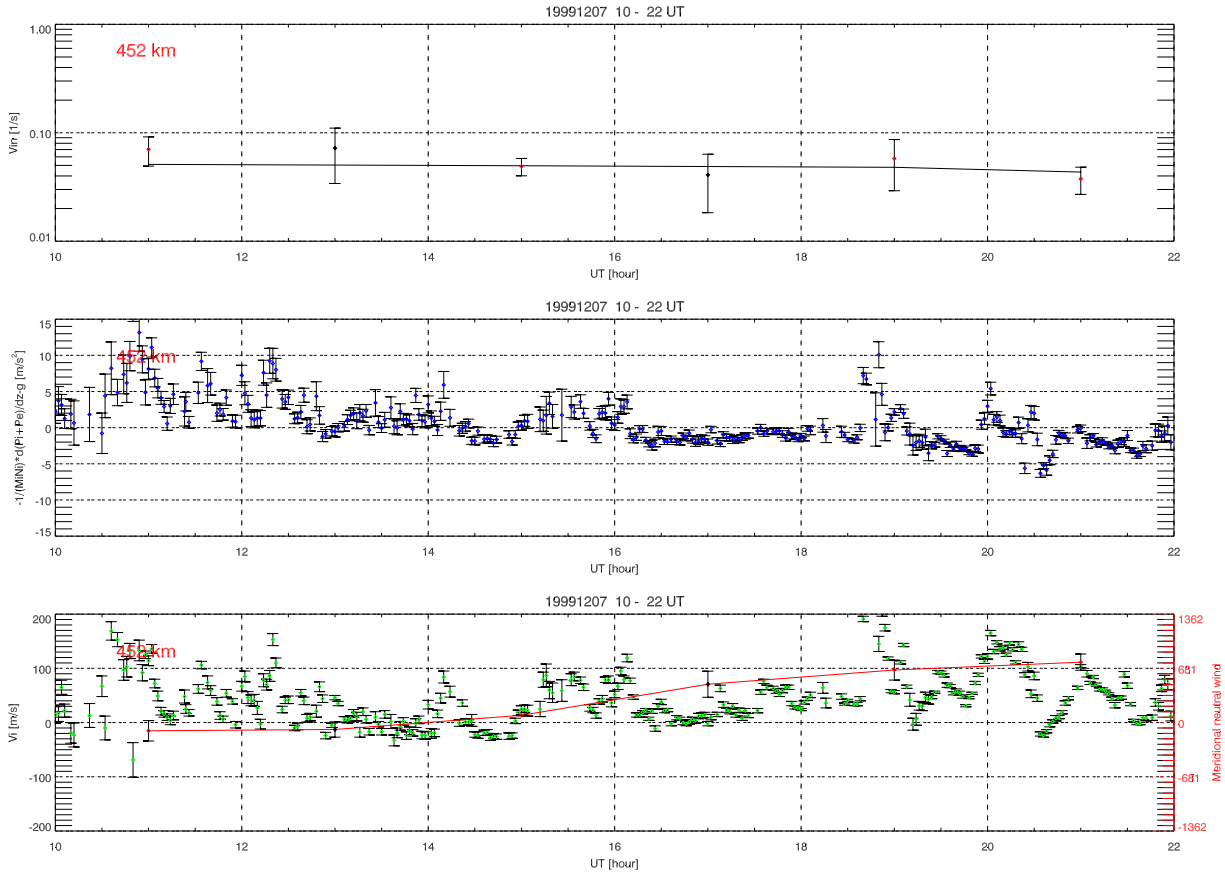

Figure A.5: Time variations of the collision frequency (upper panel), diffusion term (middle panel), and field-aligned (FA) ion and neutral velocities (lower panel) at an altitude of 452 km obtained from the ESR between 10 and 22 UT on December 7, 1999. Horizontal line and each vertical line in the upper panel indicate collision frequencies obtained from model described in equation (A.17) and from ESR observations, respectively. The red line and each green point in the lower panel indicate FA neutral velocity derived from observations and FA ion velocity from observations. The ordinate on the right hand side of the lower panel indicates the reflected meridional neutral velocity. The positive (negative) velocities indicate motion to the southward (northward).

Bibliography

Abe, T., B. A. Whalen, A. W. Yau, R. E. Horita, S. Watanabe, and E. Sagawa, EXOS D (Akebono) suprathermal mass spectrometer observations of the polar wind, *J. Geophys. Res., 98*, 11,191, 1993.

André, M., P. Norqvist, A. Vaivads, L. Eliasson, O. Norberg, A. I. Eriksson, and B. Holback, Transverse ion energization and wave emissions observed by the Freja satellite, *Geophys. Res. Lett., 21*, 1915, 1994.

André, M., Waves and wave-particle interactions in the auroral region, *J. Atmos. Terr. Phys., 59*, 1687, 1997.

André, M., P. Norqvist, L. Andersson, L. Eliasson, A. I. Eriksson, L. Blomberg, R. E. Erlandson, and J. Waldemark, Ion energization mechanisms at 1700 km in the auroral region, *J. Geophys. Res., 103*, 4199, 1998.

Arnoldy, R. L., K. Lynch, P. M. Kintner, J. Bonnell, T. E. Moore, and C. J. Pollock, SCIFER-structure of the cleft ion fountain at 1400 km altitude, *Geophys. Res. Lett., 23*, 1869, 1992.

Baumjohann, W., G. Paschmann, and C. A. Cattell, Average plasma properties in the central plasma sheet, *J. Geophys. Res., 94*, 6597, 1989.

Bilitza, D., International reference ionosphere-status 1995/96, *Adv. Space Res., 20*, 1751, 1997.

Blelly, P. L., A. Robineau, and D. Alcayde, Numerical modeling of intermittent ion outflow events above EISCAT, *J. Atmos. Terr. Phys.*, *58*, 273, 1996.

Buchert, S. C., A. P. van Eyken, T. Ogawa, and S. Watanabe, Naturally enhanced ion-acoustic lines seen with the EISCAT Svalbard Radar, *Adv. Space Res.*, *23*, 1699, 1999.

Cabrit, B., H. Opgenoorth, and W. Kofman, Comparison between EISCAT UHF and VHF backscattering cross section, *J. Geophys. Res.*, *101*, 2369, 1996.

Caton, R., J. L. Horwitz, P. G. Richards, and C Liu, Modeling of *F*-region ionosphere upflows observed by EISCAT, *Geophys. Res. Lett.*, *23*, 1537, 1996.

Chang, T., Lower-Hybrid collapse, caviton turbulence, and charged particle energization in the topside Auroral Ionosphere and magnetosphere, *Phys. Fluids*, *B5*, 2646, 1993.

Chappell, C. R., The terrestrial plasma source: A new perspective in solar-terrestrial process from Dynamic Explorer, *Rev. Geophys.*, *26*, 229, 1988.

Collis, P. N., I. Hüggström, K. Kaila, and M. T. Rietveld, EISCAT radar observations of enhanced incoherent scatter spectra: Their relation to red aurora and field-aligned currents, *Geophys. Res. Lett.*, *18*, 1031, 1991.

Conrad, J. R., and R. W. Schunk, Diffusion and heat flow equations with allowance for large temperature differences between interacting species, *J. Geophys. Res.*, *84*, 811, 1979.

Eastman, T. E., E. W. Hones, S. J. Bame, and J. R. Asbridge, The magnetospheric boundary layer - Site of plasma, momentum and energy transfer from the magnetosheath into the magnetosphere, *Geophys. Res. Lett.*, *3*, 685, 1976.

Endo, M., R. Fujii, Y. Ogawa, S. C. Buchert, S. Nozawa, S. Watanabe, and N. Yoshida, Ion upflow and downflow at the topside ionosphere observed by the EISCAT VHF radar, *Ann. Geophys.*, *18*, 170, 2000.

Feldshtein, Ya. I., and Yu. I. Galperin, The auroral luminosity structure in the high-latitude upper atmosphere - Its dynamics and relationship to the large-scale structure of the earth's magnetosphere, *Rev. Geophys., 23*, 217, 1985.

Forme, F. R. E., A new interpretation on the origin of enhanced ion-acoustic fluctuations in the upper ionosphere, *Geophys. Res. Lett., 20*, 2347, 1993.

Forme, F. R. E., and D. Fontaine, Enhanced ion-acoustic fluctuations and ion outflow, *Ann. Geophys., 17*, 190, 1999.

Forme, F., Y. Ogawa, and S. C. Buchert, Naturally enhanced ion-acoustic fluctuations seen at different wavelengths, *J. Geophys. Res., 106*, 21,503, 2001.

Foster, J. C., C. Del Pozo, K. Groves, and J. P. St-Maurice, Radar observations of the onset of current driven instabilities in the topside ionosphere, *Geophys. Res. Lett., 15*, 160, 1988.

Foster, C., M. Lester, and J. A. Davies, A statistical study of diurnal, seasonal and solar cycle variations of F-region and topside auroral upflows observed by EISCAT between 1984 and 1996, *Ann. Geophys., 16*, 1144, 1998.

Fu, S. Y., Q.-G. Zong, B. Wilken, and Z. Y. Pu, Temporal and Spatial Variation of the Ion Composition in the Ring Current, *Space Sci. Rev., 95*, 539, 2001.

Fukunishi, H., Y. Takahashi, T. Nagatsuma, T. Mukai, and S. Machida, Latitudinal structures of nightside field-aligned currents and their relationships to the plasma sheet regions, *J. Geophys. Res., 98*, 11,,235, 1993.

Garbe, G. P., R. L. Arnoldy, T. E. Moore, P. M. Kintner, and J. L. Vago, Observations of transverse ion acceleration in the topside auroral ionosphere, *J. Geophys. Res., 97*, 1257, 1992.

Hedin, A. E., Extension of the MSIS thermosphere model into the middle and lower atmosphere, *J. Geophys. Res., 96*, 1159, 1991.

Hirahara, M., T. Mukai, T. Terasawa, S. Machida, Y. Saito, T Yamamoto, and S. Kokubun, Cold dense ion flows with multiple components observed in the distant tail lobe by Geotail, *J. Geophys. Res., 101*, 7769, 1996.

Horwitz, J. L., and T. E. Moore, Four contemporary issues concerning ionospheric plasma flow to the magnetosphere, *Space Sci. Rev., 80*, 49, 1997.

Hultqvist, B., On the origin of the hot ions in the disturbed dayside magnetosphere, *Planet. and Space Sci., 31*, 173, 1983.

Hultqvist, B., On the acceleration of positive ions by high-latitude, large-amplitude electric field fluctuations, *J. Geophys. Res., 101*, 27,111, 1996.

Keating, J. G., F. J. Mulligan, D. B. Doyle, K. J. Winser, and M. Lockwood, A statistical study of large field-aligned flows of thermal ions at high-latitudes, *Planet. and Space Sci., 38*, 1187, 1990.

Kintner, P. M., J. Vago, S. Chesney, R. L. Arnoldy, K. A. Lynch, C. J. Pollock, and T. E. Moore, Localized lower hybrid acceleration of ionospheric plasma, *Phys. Rev. Lett., 68*, 2448, 1992.

Klumpar, D. M., Transversely accelerated ions: An ionospheric source of hot magnetospheric ions, *J. Geophys. Res., 84*, 4229, 1979.

Kozlovsky, A., and J. Kangas, Characteristics of the postnoon auroras inferred from EISCAT radar measurements, *J. Geophys. Res., 106*, 1817, 2001.

Köeröesmezey, Á., C. E. Rasmussen, T. I. Gombosi, and G. V. Khazanov, Anisotropic ion heating and parallel O^+, *Geophys. Res. Lett., 103*, 4171, 1998.

Knudsen, D. J., J. H. Clemmons, and J.-E. Wahlund, Correlation between core ion energization, suprathermal electron bursts, and broadband ELF plasma waves, *J. Geophys. Res.*, *103*, 4171, 1998.

Lee, M. C., R. J. Riddolls, W. J. Burke, M. P. Sulzer, E. M. C. Klien, M. J. Rowlands, and S. P. Kuo, Ionospheric plasma bubble generated by Arecibo heater, *Geophys. Res. Lett.*, *25*, 579, 1998.

Lehtinen, M. S., and A. Huuskonen, General incoherent scatter analysis and GUISDAP, *J. Atmos. Terr. Phys.*, *58*, 435, 1996.

Liu, C., J. L. Horwitz, and P. G. Richards, Effects of frictional heating and soft-electron precipitation on high-latitude *F*-region upflows, *Geophys. Res. Lett.*, *22*, 2713, 1995.

Lockwood, M., K. Suvanto, K. J. Winser, S.W.H. Cowley, and D.M. Willis, Incoherent scatter radar observations of non-Maxwellian ion velocity distributions in the auroral *F*-region, *Adv. Space Res.*, *9*, 113, 1989.

Lockwood, M., Relationship of dayside auroral precipitations to the open-closed separatrix and the pattern of convective flow, *J. Geophys. Res.*, *102*, 17475, 1997.

Lundin R., and B. Hultqvist, Ionospheric plasma escape by high-altitude electric fields - Magnetic moment 'pumping', *J. Geophys. Res.*, *94*, 6665, 1989.

Lynch, K. A., R. L. Arnoldy, P. M. Kintner, and J. L. Vago, Electron distribution function behavior during localized transverse ion acceleration events in the topside auroral zone, *J. Geophys. Res.*, *99*, 2227, 1994.

Lynch, K. A., R. L. Arnoldy, P. M. Kintner, and J. Bonnell, The AMICIST auroral sounding rocket: A comparison of transverse ion acceleration mechanisms, *Geophys. Res. Lett.*, *23*, 3293, 1996.

Maynard, N. C., E. J. Weber, D. R. Weimer, J. Moen, T. Onsager, R. A. Heelis, and A. Egeland, How wide in magnetic local time is the cusp? An event study, *J. Geophys. Res., 102*, 4765, 1997.

McCrea, I. W., M. Lester, T. R. Robinson, J.-P. St.-Maurice, N. M. Wade, and T. B. Jones, Derivation of the ion temperature partition coefficient beta-parallel from the study of ion frictional heating events, *J. Geophys. Res., 98*, 15,701, 1993.

Millward, G. H., R. J. Moffett, H. F. Balmforth, and A. S. Rodger, Modeling the ionospheric effects of ion and electron precipitation in the cusp, *J. Geophys. Res., 104*, 24,603, 1999.

Moore, T. E., C. J. Pollock, M. L. Adrian, P. M. Kintner, R. L. Arnoldy, K. A. Lynch, and J. A. Holtet, The cleft ion plasma environment at low solar activity, *Geophys. Res. Lett., 23*, 1877, 1996.

Mukai, T., M. Hirahara, S. Machida, Y. Saito, T. Terasawa, and A. Nishida, Geotail observations of cold ion streams in the medium distance magnetotail lobe in the course of a substorm, *Geophys. Res. Lett., 21*, 1023, 1994.

Newell, P. T., and C.-I. Meng, The Cusp and Cleft/boundary layer: Low-altitude identification and statistical local time variation, *J. Geophys. Res., 93*, 14,549, 1988.

Newell, P. T., C.-I. Meng, D. G. Sibeck, and R. Lepping, Some low-altitude cusp dependences on the interplanetary magnetic field, *J. Geophys. Res., 94*, 8921, 1989.

Newell, P. T., W. J. Burke, C.-I. Meng, E. R. Sanchez, and M. E. Greenspan, Identification and observations of the plasma mantle at low altitude, *J. Geophys. Res., 96*, 35, 1991a.

Newell, P. T., W. J. Burke, E. R. Sanchez, C.-I. Meng, M. E. Greenspan, and C. R. Clauer, The low-latitude boundary layer and boundary plasma sheet at low altitude: Postnoon precipitation regions and convection reversal boundaries, *J. Geophys. Res., 96*, 21,013, 1991b.

Newell, P. T., and C.-I. Meng, Mapping the dayside ionosphere to the magnetosphere according to particle precipitation characteristics, *Geophys. Res. Lett., 19*, 609, 1992.

Nilsson, H., S. Kirkwood, L. Eliasson, O. Norberg, J. Clemmons, and M. Boehm, Ionospheric signature of the cusp: A case study using Freja and the Søndrestrøm radar, *Geophys. Res. Lett., 21*, 1923, 1994.

Nilsson, H., M. Yamauchi, L. Eliasson, O. Norberg, and J. Clemmons, Ionospheric signature of the cusp as seen by incoherent scatter radar, *J. Geophys. Res., 101*, 10,947, 1996.

Norqvist, P., T. Oscarsson, M. André, and L. Blomberg, Isotropic and perpendicular energization of oxygen ions at energies below 1 eV, *J. Geophys. Res., 103*, 4223, 1998.

Ogawa, T., S. C. Buchert, N. Nishitani, N. Sato, and M. Lester, Plasma density suppression process around the cusp revealed by simultaneous CUTLASS and EISCAT Svalbard radar observations, *J. Geophys. Res., 106*, 5551, 2001.

Ogawa, Y., R. Fujii, S. C. Buchert, S. Nozawa, S. Watanabe, and A. P. van Eyken, Simultaneous EISCAT Svalbard and VHF radar observations of ion upflows at different aspect angles, *Geophys. Res. Lett., 27*, 81, 2000a.

Ogawa, Y., F. Forme, and S C. Buchert, Frequency dependent power fluctuations: a feature of the ESR system or physical?, *Ann. Geophys., 18*, 1224, 2000b.

Papadopoulos, K., A review of anomalous resistivity for the ionosphere, *Rev. Geophys. Space phys., 15*, 113, 1977.

Pesnell, W. D., K. Omidvar, and W. R. Hoegy, The momentum transfer collision frequency of O^+ - O, *Geophys. Res. Lett., 20*, 1343, 1993.

Press, W. H., S. A. Teukolsky, W. T. Vetterling, and B. P. Flannery, NUMERICAL RECIPES in C, second edition, *Cambridge university press*, 1992.

Reiff, P. H., J. L. Burch, and T. W. Hill, Solar wind plasma injection at the dayside magnetospheric cusp, *J. Geophys. Res., 82*, 479, 1977.

Rietveld, M. T., P. N. Collis, and J.-P. St.-Maurice, Naturally enhanced ion-acoustic waves in the auroral ionosphere observed with the EISCAT 933 MHz radar, *J. Geophys. Res., 96*, 19,291, 1991.

Rietveld, M. T., P. N. Collis, A. P. van Eyken, and U. P. Løvhaug, Coherent echoes during EISCAT UHF Common Programmes, *J. Atmos. Terr. Phys., 58*, 161, 1996.

Roble, R. G., and B. A. Emergy, On the global mean temperature of the thermosphere, *Planet. and Space Sci., 31*, 597, 1983.

Roederer, J. R., *Solar-Terrestrial Research for 1980s*, National Research Council, *National Academy Press*, Washington, D.C., 1981.

Rosenbauer, H., H. Grünwaldt, M. D. Montgomery, G. Paschmann, and N. Sckopke, HOES/2 plasma observations in the distant polar magnetosphere: The plasma mantle, *J. Geophys. Res., 80*, 2723, 1975.

Salah, J. E., Interim standard for the ion-neutral atomic oxygen collision frequency, *Geophys. Res. Lett., 20*, 1543, 1993.

Sandahl, I., and P.-A. Lindqvist, Electron populations above the nightside auroral oval during magnetic quiet times, *Planet. and Space Sci., 38*, 1031, 1990.

Schunk, R. W., and J. C. G. Walker, Thermal diffusion in the *F2*-region of the ionosphere *Planet. Space Sci., 18*, 535, 1970.

Schunk, R. W., Transport equation for aeronomy, *Planet. Space Sci., 23*, 437, 1975.

Schunk, R. W., P. M. Banks, and W. J. Raitt, Effect of electric fields on the daytime high-latitude *E* and *F* regions, *J. Geophys. Res., 80*, 3121, 1975.

Schunk, R. W., and A. F. Nagy, Ionospheres of the terrestrial planets, *Rev. Geophys. Space phys., 18*, 813, 1980.

Schunk, R. W., and A. F. Nagy, Ionospheres: Physics, Plasma Physics, and Chemistry, *Cambridge university press*, 2000.

Seki, K., M. Hirahara, T. Terasawa, T. Mukai, Y. Saito, S. Machida, T. Yamamoto, and S. Kokubun, Statistical properties and possible supply mechanisms of tailward cold O^+ beams in the lobe/mantle region, *J. Geophys. Res., 103*, 4477, 1998.

Sedgemore-Schulthess, K. J. F., M. Lockwood, T. S. Trondsen, B. S. Lanchester, M. H. Rees, D. A. Lorentzen, and J. Moen, Coherent EISCAT Svalbard Radar spectra from the dayside cusp/cleft and their implications for transient field-aligned currents, *J. Geophys. Res., 104*, 24,613, 1999.

Seo, Y., J. L. Horwitz, and R. Caton, Statistical relationship between high-latitude ionospheric *F* region/topside upflow and their drivers: DE 2 observations, *J. Geophys. Res., 102*, 7493, 1997.

Sharp, R. D., R. G. Johnson, and E. G. Shelly, Observations of an ionospheric acceleration mechanism producing energetic (keV) ions primarily normal to the geomagnetic field direction *J. Geophys. Res., 82*, 3324,1997.

Shelley, E. G., R. D. Sharp, and R. G. Johnson, He^{2+} and H^+ flux measurements in the day side cusp - Estimates of convection electric field, *J. Geophys. Res., 81*, 2363, 1976.

Singh, N, Pondermotive versus mirror force in creation of the filamentary cavities in auroral plasma, *Geophys. Res. Lett., 21*, 257, 1994.

St.-Maurice J.-P., W. Kofman, and D James, In situ generation of intense parallel electric field in the lower ionosphere, *J. Geophys. Res., 101*, 335,1996.

St-Maurice, J.-P., and P. J. Laneville, Reaction rate of O^+ with O_2, N_2, and NO under highly disturbed auroral conditions, *J. Geophys. Res.*, *103*, 17,519, 1998.

Stasiewicz, K., B. Holback, V. Krasnoselskikh, M. Boehm, M. R. Boström, and P. M. Kintner, Parametric instabilities of Langmuir waves observed by Freja, *J. Geophys. Res.*, *101*, 21,515, 1996.

Su, Y.-J., R. G. Caton, J. L. Horwitz, and P. G. Richards, Systematic modeling of soft-electron precipitation effect on high-latitude *F* region and topside ionospheric upflows, *J. Geophys. Res.*, *104*, 153, 1999.

Suvanto, K., M. Lockwood, and T. J. Fuller-Rowell, The influence of anisotropic *F* region ion velocity distributions on ionospheric ion outflows into the magnetosphere, *J. Geophys. Res.*, *94*, 1347, 1989.

Thayer, J. P., T. L. Killeen, F. G. McCormac, C. R. Tschan, J.-J. Ponthieu, and N. W. Spencer, Thermospheric neutral wind signatures dependent on the east-west component of the interplanetary magnetic field for Northern and Southern Hemispheres as measured from Dynamics Explorer-2, *Ann. Geophys.*, *5*, 363, 1987.

Veselovsky, I. S., P. T. Newell, and T. Y. Lui, Pervasive small-scale enhancements in mantle and polar rain precipitation, *Geophys. Res. Lett.*, *22*, 3263, 1995.

Wahlund, J.-E., H. J. Opgenoorth, I. Häggström, K. J. Winser, and G. O. L Jones, EISCAT observations of topside ionospheric ion outflows during auroral activity: Revisited, *J. Geophys. Res.*, *97*, 3019, 1992a.

Wahlund, J.-E., F. R. E. Forme, H. J. Opgenoorth, M. A. L. Persson, E. V. Mishin, and A. S. Volokitin, Scattering of electromagnetic waves from a plasma: Enhanced ion-acoustic frustrations due to ion-ion two-stream instabilities, *Geophys. Res. Lett.*, *19*, 1919, 1992b.

Wannberg, G., I. Wolf, L.-G. Vanhainen, K. koskenniemi, J. Rottger, M. Postila, J. Markkanen, R. Jacobsen, A. Stenberg, R. Larsen, S. Eliassen, S. Heck, and A. Huuskonen, The EISCAT Svalbard radar: A case study in modern incoherent scatter radar system design, *Radio Sci.*, *32*, 2283, 1997.

Whalen, B. A., S. Watanabe, and A. W. Yau, Observations in the transverse ion energization region, *Geophys. Res. Lett.*, *18*, 725, 1991.

Winglee, R. M, Multifluid simulations of the magnetosphere: The identification of the geopause and its variation with IMF, *Geophys. Res. Lett.*, *25*, 4441, 1998.

Winningham, J. D., W. J. Heikkila, F. Yasuhara, and S.-I. Akasofu, The latitudinal morphology of 10-eV to 10-keV electron fluxes during magnetically quiet and disturbed times in the 2100-0300 MLT sector, *J. Geophys. Res.*, *80*, 3148, 1975.

Winser, K. J., M. Lockwood, G. O. L. Jones, and K. Suvanto, Observation of nonthermal plasmas at different aspect angles, *J. Geophys. Res.*, *94*, 1439, 1989.

Yau, A. W., B. A. Whalen, A. G. McNamara, P. J. Kellogg, and P. J. W. Bernstein, Particle and wave observations of low-altitude ionospheric ion acceleration events, *J. Geophys. Res.*, *88*, 341, 1983.

Yau, A. W., and M. André, Sources of ion outflow in the high latitude ionosphere, *Space Sci. Rev.*, *80*, 1,1997.

Yoshida, N., S. Watanabe, H. Fukunishi, T. Sakanoi, T. Abe, T. Mukai, H. Hayakawa, A. Matsuoka, Y. Kasahara, R. Fujii, S. Nozawa, and Y. Ogawa, Coordinated Akebono and EISCAT Observations of Suprathermal Ion Outflows in the Nightside Inverted-V Region, *J. Atmos. Sol.-Terr. Phys.*, *62*, 449, 2000.

Zhou, X. W., C. T. Russell, G. Le, S. A. Fuselier, and J. D. Scudder, Solar wind control of the polar cusp at high altitude, *J. Geophys. Res.*, *105*, 245, 2000.